FABRICATION AND CHARACTERIZATION OF INSULATING-FILM/PHOSPHOR-FILM/INSULATING-FILM HETEROSTRUCTURES

SUBMITTED BY

YEUNG KAI MING

FOR THE DEGREE OF

MASTER OF PHILOSOPHY IN PHYSICS

AT

THE HONG KONG POLYTECHNIC UNIVERSITY

2002

ABSTRACT

Insulating-film/phosphor-film/insulating-film heterostructures are currently being investigated as potential structures for future ac thin film electroluminescent device (TFELD) applications. The insulating layer and the phosphor layer are of different kinds of materials possessing very different structural, electrical and optical properties. To optimize the performance of these heterostructures, a good understanding of the optical and electrical properties of each individual layer, namely, the insulating layer and the phosphor layer, is of paramount importance. The main objective of our study is to identify the important processing parameters in the fabrication of each individual layer used in these heterostructures. The effects of these processing parameters on the structural, electrical and optical properties of the individual layers were investigated. The correlation between the structural, optical and electrical properties was investigated.

In this study, ZnS:Mn was used as the phosphor layer while for the insulating materials, two types of ceramic materials, $BaTiO_3$ and $PbZr_xTi_{1-x}O_3$ (PZT) were employed. Optimized processing parameters for growing these films by pulsed laser deposition (PLD) have been revealed. The crystallographic structures and impurities of the prepared films were studied by X-ray diffractometry (XRD) and Raman spectroscopy. The surface morphology, surface roughness, grain size and porosity were examined by scanning electron microscopy (SEM) and atomic force microscopy (AFM). From the growth of $BaTiO_3$ films on $LaAlO_3$ (LAO) substrates by PLD, structural characteristics were found to depend on film thickness. In general, (100)-oriented $BaTiO_3$ films with different thickness were epitaxially grown on LAO substrates. All the films fabricated were smooth and crack free. The texture of the films as examined by XRD rocking curve varies with film thickness. The grain size and surface roughness were found to increase with thickness of the films. Raman

scattering confirmed that these films possess tetragonal phase with good stoichiometry and free of impurities. For those $BaTiO_3$ and PZT films grown on epitaxial LNSMO buffered LAO, they were epitaxially grown with (100) orientation. On the other hand, ZnS:Mn films grown on either Si or ITO coated glass substrate were polycrystalline in structure. These films were found to have different combinations of phase when fabricated by PLD under different deposition temperatures. Zinc blende structure dominated when fabricated under lower deposition temperatures of around 150°C, and with higher deposition temperatures of around 450°C a higher wurtzite phase ratio was obtained.

For electrical properties, the dielectric constant and P-E loop characteristics of the $BaTiO_3$ and PZT films, deposited on the LNSMO electrode buffered LAO, were measured. Only weak ferroelectric behaviour for $BaTiO_3$ films as observed and the dielectric constant at 1 kHz was around 1200. PZT films were confirmed to have ferroelectricity as shown in P-E measurements and the dielectric constant at 1 kHz was around 680.

For optical properties, the optical constants of the ZnS:Mn layers were measured by spectroscopic ellipsometry (SE). Variations in the band gap energy of ZnS and the $^4T_1(G) - {}^6A_1(S)$ transition energy of the doped Mn^{2+} ions were investigated by optical transmittance and photoluminescence (PL) measurements, respectively. The changes in the optical properties of the ZnS:Mn layer with different processing parameters were correlated to its structural characteristics.

Lastly, heterostructures of phosphor layer and insulating layers were fabricated. Their performance in relation to different insulating materials was characterized by measuring their electroluminesent properties. However, this study indicated that the use of $BaTiO_3$ and PZT insulating materials has no significant influence on the electroluminescence behaviour of the ZnS:Mn layer.

ACKNOWLEGEMENTS

I would like to acknowledge my chief supervisor, Dr. C.L. Mak, for his valuable advice and discussion throughout these two years. Special thanks would also be given to my co-supervisors Dr. K.H. Wong and Dr. W.L. Tsui for always giving enlightening suggestions and discussions in many different aspects. I would also extend my special thanks toward Dr. K.H. Pang for the discussions especially on structural characterization by X-ray diffraction, AFM and SEM. Thanks would also go to Mr. M.N. Yeung for his assistance in SEM operation.

I would also like to thank my research companions, Mr. K.S. So, Miss H.Y. Cheung, Miss F.F. Hau and Mr. W.S. Tsang, for their useful suggestions.

Finally, I would like to thank all members of my family for their encouragement and support throughout the research period.

This project is supported by a Research Grant of The Hong Kong Polytechnic University under Code No. G-V859. I am grateful for the award of a research studentship by the university.

TABLE OF CONTENTS

PAGE

CHAPTER 1

INTRODUCTION

Display technology is being steadily driven towards light-weight, high-quality, high-resolution displays to replace the current cathode ray tube (CRT) display. Among the display driving forces are the advancements in portable computers, high-definition television (HDTV), and head-mounted displays. Flat panel display (FPD) technology is the CRT replacement technology of choice. [Rack et al., 1998]

Representatives of current FPD technologies are plasma, liquid crystal (LCD), field emission (FED), and electroluminescent (EL) displays. Each of these display types has unique advantages and disadvantages for particular markets. Among different FPD, thin-film electroluminescent devices (TFELDs) have many promising characteristics. TFELDs are all-solid, emissive display devices with the following superior characteristics: fast response (several microseconds), wide viewing angles (> 160°), high resolution, wide operation temperature range (-20°C – 85°C), light weight and good display quality. Hence TFELDs for use in flat-panel display applications has become an important area for physicists and engineers. Despite the phosphor technology required for a full-color display application of the TFELDs, the insulating layer materials are very important for the device operations. For acceptable performance of TFELDs, high quality insulating films with high breakdown voltages, high dielectric constants, and excellent interfacial stability are required. [Krasnov, 1999]

A number of dielectric materials have been adapted into the TFELDs. These dielectric materials are generally required to provide current confinement, charge storage and barrier protection. Further, there are requirements on the insulator-semiconductor interface (ISI), thermal expansion matching, the amount of charge stored at the interfaces, good brightness characteristics, and low leakage of the bound charge under low applied voltages [Krasnov, 1999]. Different dielectric materials

have been investigated for the device fabrication, these include Al_2O_3 [Theis, 1984], Ta_2O_5, SiON [Tiku et al., 1989], Y_2O_3 [Nakanishi et al., 1996] and $BaTiO_3$ [Lee et al., 2001]. Among these dielectric materials, $BaTiO_3$ has earned much attention.

In ACTFEL device operation, this insulating layer acts as the current limiting layer to protect the phosphor layer against catastrophic damage caused by unlimited current. On the other hand, it also provides sufficient charging and discharging displacement current for efficient EL operation, which would depend on the dielectric permittivity of the material and the efficiency of charge injected into the phosphor layer. For efficient ACTFEL device, despite of the phosphor layer, a suitable choice of the insulating layer is the second most important issue. In general, insulating layers with high dielectric permittivity, high breakdown field and small loss tangent are essential for improving the EL efficiency. However, the subsequent increasing of RC time when charging and discharging this high-permittivity EL layers will reduce the refresh rate of the ACTFEL display. And that will inhibit the ACTFEL device developed into a large, high-resolution flat-panel display.

With its special polarization-voltage loop and well-known high dielectric permittivity, ferroelectric materials should have remarkable difference compared to the dielectric materials and probably solve the RC time problem while maintain the advantage of high dielectric permittivity. The P-E loop of the ferroelectric material suggests that with a suitable voltage driver, one can control a single pixel to undergo EL process for an ACTFEL display. This can be illustrated by first keeping a row of pixels slightly below the coercive field without charging process. By applying a reversed field at the corresponding column to exceed the coercive field, only a single pixel of that row involves in the charge transferring EL process. This result will be equivalent to only charge up a single pixel and thus will reduce the RC product of that row. Hence, an improved EL brightness and a shorter switching time would be expected when ferroelectric materials are incorporated into the EL device structure. In this study, the interest is to investigate the difference in using dielectric and ferroelectric materials as the insulating layers for the EL devices. In order to

investigate the effect of different types of insulating material on EL device, $BaTiO_3$ as the dielectric material and $Pb(Zr_{0.52}Ti_{0.48})O_3$ (PZT) as the ferroelectric material were used throughout the project.

Pulsed laser deposition (PLD) was used throughout in our experiments to fabricate the device. It is well known for its flexibility in thin film fabrication. PLD has proved to be a very successful technique for high quality thin oxide films fabrication in our previous investigations, including LSMO [Wu et al., 2001] and PZT [Wu et al., 2000]. However phosphor material like ZnS:Mn has not been fabricated by PLD in our group before, and hence fabrication techniques for phosphor films have also been studied.

This thesis focuses on the fabrication and characterization of the insulating-film/phosphor-film/insulating-film tri-layer heterostructure. Therefore, studies on the fabrication and characterization of individual layers using PLD are necessary. For the insulating layers, both the structural and dielectric properties of the films are important in device operation. For example, films with suitable lattice orientation can enhance their dielectric permittivity, while a smooth film surface is desired for reliable device application. Furthermore, ferroelectric layer with a good *P-E* hysteresis loop is useful in obtaining a better device operation. For the phosphor layer, besides its structural properties, its optical properties are also important. In our studies, structural properties were characterized by XRD, SEM and AFM. Impedance analyzer and *P-E* characteristics were employed to characterize the dielectric properties of the insulating layer. For measuring the optical properties of the phosphor layer, transmittance measurement and photoluminescent emission were used. Based on these results, we can optimize the parameters in our PLD process to obtain the desired film properties. Finally, insulating layer and phosphor layer were incorporated together to form a heterostructure and were characterized by its EL emission.

In chapter 2, a brief introduction of electroluminescent device covering its structure, operation, materials requirement and drive method is presented. Chapter 3 is a brief history and the principle of PLD, and also the advantages and disadvantages of

the PLD technique for film preparation. Chapter 4 presents the experimental setup and measurement. Chapter 5 covers the fabrication and characterization of the individual layers including the insulating layer and phosphor layer. The last chapter is to conclude the present work and to make suggestions for future investigation and development.

CHAPTER 2

ELECTROLUMINESCENT DEVICE

Electroluminescence (EL) is a non-thermal generation of light resulting from the application of an electric field to a substrate. There are two classes of EL devices. One is the light-emitting diode (LED) device, in which light is generated by electron-hole pair recombination near a p-n junction. The other one is often called high-field electroluminescence in which light is generated by impact excitation of a light-emitting center, called an activator or a luminescent center, by high-energy electrons. The electrons gain their high energy from a high electric field on the order of 10^8 V/m. In this study, we are interested in the latter type.

The phenomenon of high-field electroluminescence was discovered by Destriau in 1936 [Destriau, 1936]. He observed light emission from a ZnS phosphor powder dispersed in an insulator sandwiched between two electrodes when a high AC voltage was applied. However, the effort on the development of AC powder EL devices was not begun until the transparent electrically conductive films made of SnO_2 were developed around 1950 which trigger research and development of EL around the world. During the period from 1950's to early 1960's, basic studies were focused on the AC powder EL. However, the AC powder EL devices were found to have limitations such as multiplexing problem, low luminance, high operating voltage, poor contrast and significant luminance degradation over fairly short time (~500 hours). These properties obstruct the development of this device into display applications. The breakthrough began from the development of thin-film EL structures in late 1950's. Afterwards, the introduction of double-insulating-layer type AC thin-film EL structure by Russ and Kennedy in 1967 [Russ et al., 1967] and the announcement of bright (~3400cd/m^2) and long lifetime (>10000 hours) double-insulating-layer AC thin-film EL developed by Inoguchi et al [Inoguchi et al., 1974] stimulated a lot of studies in electroluminescence device. Based on this structure, different

investigations on the choice of dielectric materials for insulating layers and optimization of deposition processes as well as new deposition methods were performed to put this device to use in display technology.

In this chapter, the general descriptions of EL devices will be covered. The structures of the typical EL devices will be first presented. Then, some operation theories of EL devices are described. Following is the consideration on the materials including phosphor and the insulating materials. Finally, a brief introduction on the drive method will be described.

2.1 Device structure

2.1.1 AC thin film EL (ACTFEL) device

An ACTFEL device consists of several constituent thin-film layers that are all important in terms of device operation. This kind of device consists of a phosphor layer, at least one insulating layer, an opaque conductor, a transparent conductor and a substrate. Fig. 2.1(a) shows the basic 'standard' structure of an ACTFEL device. The central layer is the thin-film phosphor that emits light when a large enough electric field is applied across it. Since the applied field is so high (~10^8 V/m) that any imperfection in the thin film stack that produces a short circuit would cause a destructive amount of energy to be dissipated if the phosphor were connected to the electrodes directly. In order to protect this phosphor layer against the high electric field, the insulating layers on both side of the phosphor layer would act as the current limiting layers to limit the maximum current within the capacitive charging and discharging displacement current level. Finally, electrodes on top and bottom of the device with either side is transparent in the visible spectra complete a basic capacitive structure. The standard ACTFEL device structure is deposited onto a transparent substrate and light reaches the viewer through the substrate. The other is so called "inverted' ACTFEL device structure, as shown in Fig. 2.1(b). The difference is the

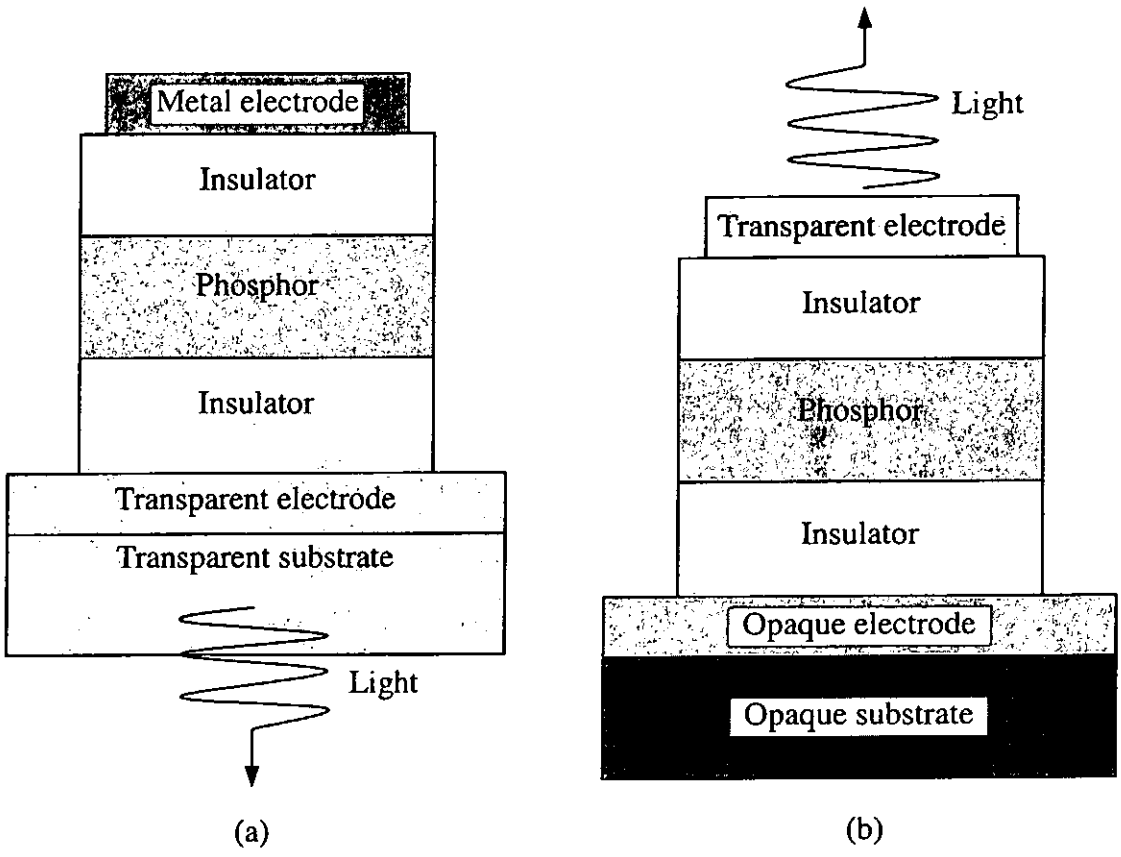

Figure 2.1: (a) The standard ACTFEL device structure. (b) The inverted ACTFEL device structure.

fabrication of the device onto an opaque substrate and the light reaches the viewer through the transparent top electrode.

The standard and inverted ACTFEL devices are both used in commercial processes, and the choice of the structure is often determined by process requirements, process limitation or the ultimate device applications. Both structures have its advantages and disadvantages. The standard structure is preferred for test and monochrome passive-matrix displays because the active device layers are shielded from the viewer by a glass substrate that provides inherent durability. However when high temperature process procedures are involved, the standard structure becomes undesirable because its glass substrate-based structure begins melting around 600°C. On the other hand, for the inverted structure, option of depositing on opaque substrate allows the use of high-temperature tolerant ceramic or silicon substrates.

2.1.2 AC powder EL device

The AC powder EL device was first developed by Sylvania in the first era of EL devices [Ono, 1995]. The structure and fabrication for this type of EL is relatively simple. A typical AC powder EL device structure is shown in Fig. 2.2. The phosphor layer (50-100 μm) consists of a suitably doped ZnS powder (with grain size of 5 – 20 μm) suspended in a dielectric, which also acts as a binder. The phosphor layer is sandwiched between two electrodes, one of which is transparent and supported by a substrate such as glass. The dielectric for holding the phosphor powder may be an organic material, such as cyanoethylcellulose and PVC. Extra protection against catastrophic breakdown can be done by adding an insulating layer between the phosphor layer and the electrodes.

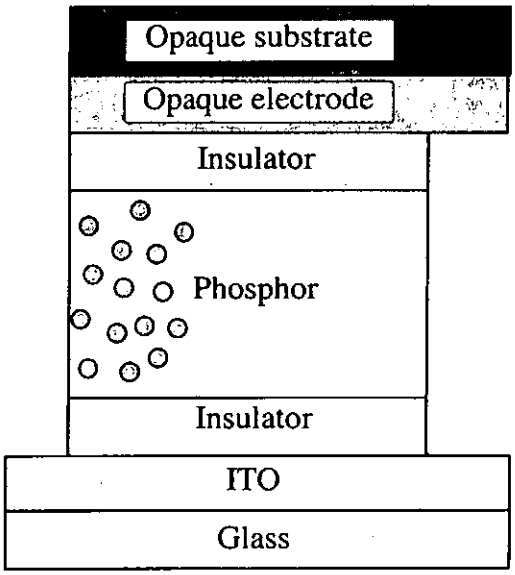

Fig. 2.2 AC powder EL device structure

2.2 Device operation

Since Inoguchi et al [Inoguchi et al., 1974] reported on high-luminance and long-lifetime EL devices, ACTFEL with a double-insulating layer structure has been the

center of research and development. Much of the efforts have been placed on the studies of this type of EL device and this makes ACTFEL become the best-understood EL device on operation mechanism. Hence the description of the operation in this section will be concentrated on ACTFEL devices.

The light emission of an electroluminescent device is originated from transferring energy from charge carriers to luminescent centers in the phosphor. This requires the presence of charge carriers in the phosphor layer with sufficient energy to excite the luminescent centers to an excited state. For ACTFEL device, the light generation is not induced by a direct current flow through the phosphor layer because it is in series with the insulator. Instead, light emission is produced by applying an AC voltage to the device. The conduction of charge carriers in the phosphor layer of an ACTFEL device is usually assumed to originate from tunneling of electrons from the insulator-phosphor interface states. The energy depth of the states required the presence of a high electric field at the phosphor-insulating interface for injection to occur. And this field also serves to accelerate the carriers to gain sufficient energy to excite the luminescent centers in the phosphor.

When an ACTFEL device is driven by an AC voltage with amplitude below the threshold voltage of the device, the electrical characteristics are similar to a simple capacitor. The capacitance of an insulating layer or the phosphor layer can be obtained from the formula below:

$$C_{layer} = \frac{\varepsilon_r \varepsilon_o}{d_{layer}} \tag{2.1}$$

where C_{layer} is the equivalent capacitance of the layer and d_{layer} is the thickness. ε_o and ε_r is the permittivity of vacuum and relative dielectric constant of the layer respectively. Since an ACTFEL device consists of several layers, the device can be considered as a capacitor with the capacitance equal to the capacitances of the individual insulator and

phosphor layers in series, i.e.

$$C_i = \frac{C_{ph} C_{i,top} C_{i,bottom}}{C_{ph} C_{i,top} + C_{ph} C_{i,bottom} + C_{i,top} C_{i,bottom}} \tag{2.2}$$

And the insulating layers can be treated as a single capacitance,

$$C_i = \frac{C_{i,top} C_{i,bottom}}{C_{i,top} + C_{i,bottom}} \tag{2.3}$$

When a device is driven under the threshold voltage, the field in the phosphor layer is then given by

$$E_{ph} = \frac{C_i}{C_i + C_{ph}} \frac{V_{applied}}{d_{ph}} \tag{2.4}$$

where $V_{applied}$ is the voltage applied to the device, C_i is the capacitance of the insulating layer, C_{ph} is the capacitance of the phosphor layer and d_{ph} is it thickness. When the applied AC voltage reaches the threshold value, V_{th}, of the ACTFEL device, at which the injection of charge occurs, the purely capacitive behaviour of the phosphor layer is no longer present. When the voltage applied across the device has a magnitude greater than V_{th}, charge is transferred across the phosphor layer and light emission is observed. In this regime, the operation of an ideal ACTFEL device can be classified into two behaviors and proceeds as follow.

When the applied voltage is below the turn-on voltage, the device behaves as a capacitor as described above. Then, when the applied voltage reaches the turn-on voltage of the ACTFEL device, the phosphor field at the phosphor/insulator interface on the cathodic side of the device is high enough that electrons trapped in interface states or bulk traps are tunnel emitted into the phosphor conduction band. The

schematic diagram is shown in process 1 of the energy-band diagram in Fig. 2.3. The injected electrons are accelerated and gain kinetic energy from the electric field and drift across the phosphor layer (process 2 of Fig. 2.3). When the electrons transmit across the phosphor layer, they may collide with luminescent impurities that absorb some of the energy and are subsequently promoted to an excited state (process 3 of Fig. 2.3). When the luminescent centers relax back to their ground states, they may release the energy either through the emission of a photon with energy equal to the energy level difference (process 4 of Fig. 2.3), or non-radiatively through phonon emission. The efficiency of the electroluminsecent properties is certainly maximized when all the excited impurities relax radiatively. After collision, the electrons continue to travel across the phosphor layer, and gain energy and possibly undergo more collisions until reaching the anodic phosphor/insulator interface, where they are trapped by the phosphor/insulator interface state caused by the disorder at the heterojunction (process 5 of Fig. 2.3). Finally, some of the photons released by the luminescent impurities pass through the device and are observed.

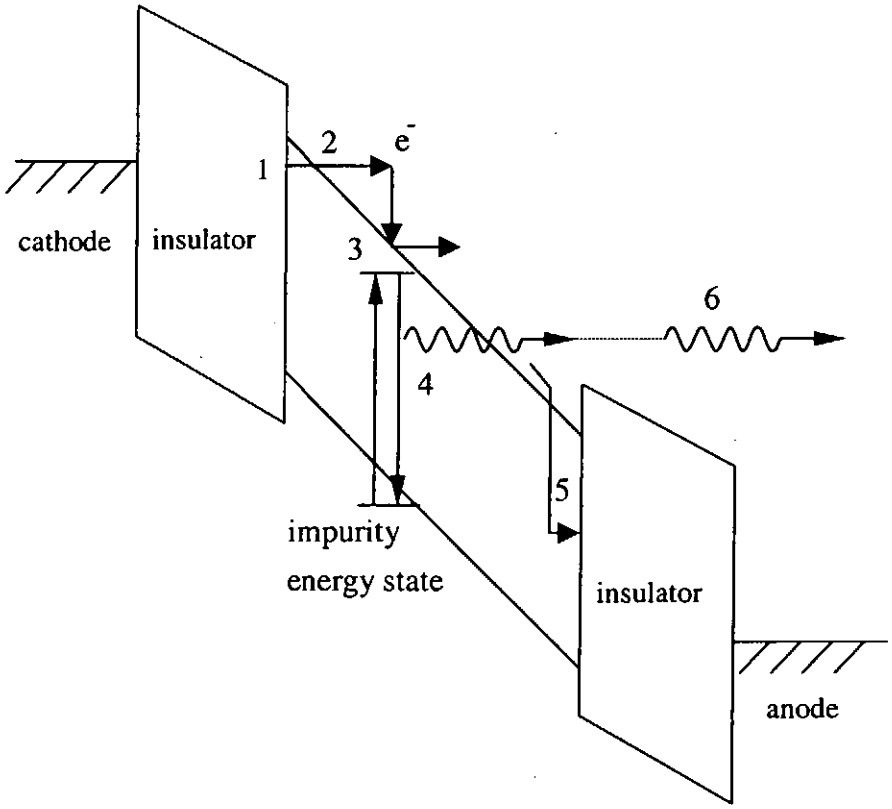

Figure. 2.3 Energy-band diagram of an ideal ACTFEL device under applied voltage; numbers refer to the corresponding features described in the text.

Next, the device will undergo a similar process driven by the opposite voltage polarity. Between AC voltage pulses, there is an interval of zero applied voltage. However, the internal field of the phosphor is non-zero due to the presence of trapped charges at the interface setup by previous external bias. This non-zero field, known as the internal polarization field, usually is strong enough to cause emission of some of the electrons at one interface and leaks across the phosphor to the opposite interface. Even though there is leakage of interface charges, much of them still accumulates at the phosphor/insulator interface and assists the reverse applied voltage process. Since these trapped electrons at the interface create an internal field in the phosphor, the biasing electric field is enhanced by the combination of the internal field and the external applied voltage. The effect of this combination lowers the voltage required for injection and hence modifies the turn-on voltage of the device.

The mechanism of ACTFEL device operation described is a simple and ideal

model, the operation mechanism however can be much more complicated for a real device. Several considerations including the presence of space charge in the phosphor layer [Shih et al., 1995], dependence of the emission rate of electrons into the phosphor on the density of interface states [Bhaskaran et al., 1995], role of holes in the operation [Corlatan et al., 1997] are suggested to have effect on the device performance. The presence of space charge in the phosphor is particularly the one being extensively studied. In the ideal model, space charge in the phosphor is not considered, so the slope of the bands and the electric field in the phosphor layer is constant as shown in Fig. 2.3. However, if space charge exists in the phosphor, the bands of the phosphor will be bent due to a non-uniform electric field profile set up by the space charge, as shown in Fig. 2.4. When a bias voltage is applied to the device, the presence of space charge causes the band to be bent so that the field is enhanced near the cathodic side of the device while the field is reduced at the anodic side. The enhancement of the cathodic field facilitates tunneling injection of electrons from the interface states and results in a lower voltage for the tunneling injection. On the other hand, the reduced field at the anodic side allows the electron distribution to cool down before hitting the interface which has the effect of decreasing insulator degradation due to hot electron bombardment at the anode.

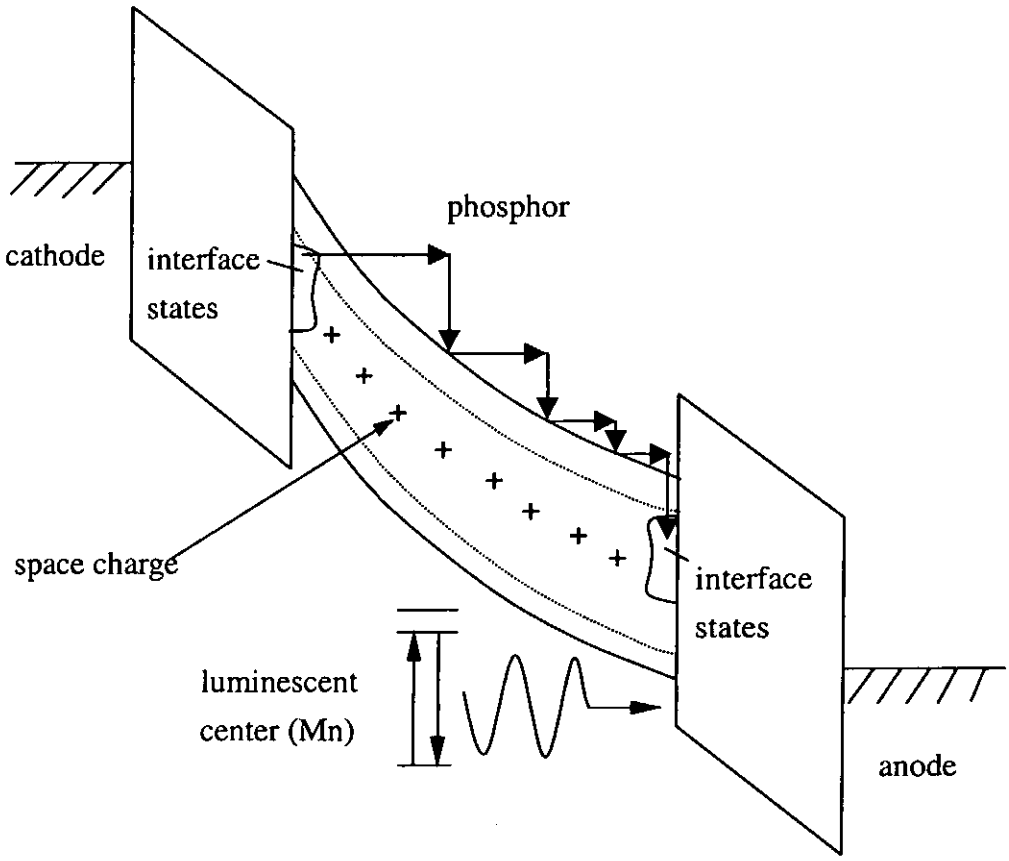

Fig. 2.4 Energy-band diagram of the double-insulating-layer-type AC thin-film device containing space charge in the phosphor layer under applied voltage.

2.3 Materials requirements

The operation of EL device depends on the performance of the constituent layers. The phosphor layer and the insulating layer are especially important to the whole device in terms of electrical properties, optical properties and the electroluminescent efficiency, especially in ACTFEL devices. This section describes the material requirements for the phosphor layer and insulating layer in order to fabricate EL device.

2.3.1 The phosphor layer

There are many materials available for use as phosphors; however, only certain phosphors would satisfy the requirements for use as the EL device phosphor,

especially for ACTFEL device. It is because the phosphor in use must be capable to withstand in high field operation up to 10^8 V/m, which is necessary for EL emission [Ono, 1995], and provide a medium for the efficient transport of high energy (> 2 eV) electrons. Many phosphor materials hence become not suitable for EL device due to these two major requirements.

Usually the phosphor consists of a host material with luminescent centers. The host material and the luminescent centers have to satisfy some requirements as described in the following sections.

2.3.1.1 Phosphor host materials

For a suitable phosphor host materials used in EL devices, the first requirement is that the bandgap must be large enough so that the emitted visible light from the luminescent centers will not be re-absorbed by the host material. However the bandgap should not be too large either because the relatively deep interface states for large bandgap host materials do not emit a sufficient number of electrons at the fields reached with reasonable applied voltages (< 300 V). As a result, the suitable phosphor host materials are limited to ones with the range of bandgap between ~3 to ~4.5 eV [Ono, 1995]. In addition, the transition-type bandgap, whether it is direct or indirect, would have strong effect on interface carrier injection. An example for a suitable host material is ZnS. ZnS possesses a bandgap of 3.6 eV with a direct-transition type band structure which is wide enough to transmit the visible spectrum of light, but not so wide as to inhibit the avalanche multiplication process of electrons for providing enough carriers to impact excitation of the luminescent centers.

The second requirement is that the host material should have a high degree of crystallinity and large grain size, which have been shown to be an essential condition for the best ACTFEL device [Ono, 1995]. Since the emission of light is originated from the impact excitation of luminescent centers by hot electrons, the best possible crystalline order of host materials is required to allow electron acceleration to a kinetic

energy sufficient for impact excitation to occur. Electrons transport in amorphous or poorly crystallized semiconducting material is often through hopping conduction between dense but localized states within the band gap. When compare this to the crytalline semiconductor, in which the electrons transport through the delocalized extended state in the conduction band; hopping conduction is a much less efficient means of electron transport than delocalized extended band state conduction. Delocalized carrier transport through the phosphor have been shown to increase dramatically with higher crystallinity [Kina et al., 1997; Tong et al., 1999], so enhancement of transport of electrons at high field is expected in a phosphor of higher crystallinity. Hence the hot electrons in the phosphor will more efficiently excite the luminescent centers which result in a brighter and more efficient EL device.

It is also desirable that the dielectric properties of the host material be such that an electric field large enough for electron injection can be achieved and the injected electrons are efficiently transported in the phosphor layer. Since the applied voltage is dropped across the insulating layers and the phosphor layer, it is realized that the larger phosphor field will be favourable. The condition required would come to equation 2.4 which reveals that $C_{ph} << C_i$ is preferred. Therefore, the dielectric constant of the phosphor should be as small as possible relative to the insulator, so that most of the applied voltage drops across the phosphor layer rather than across the insulator.

2.3.1.2 Luminescent centers

Luminescent centers (dopants in the phosphor) determine the colour of emitted light. They ordinarily occupy the cations of the host material and presented in a small fraction on the order of one percent in concentration. However this level of dopants is several orders of magnitude larger than that found in semiconductor devices and it is considered already high enough to affect the crystallinity of the phosphor and introduces defects into the phosphor. It is known that the transition from excited state

back to the ground state in a luminescent center can undergo a radiative band-to-band process and a competitive non-radiative process through excited vibration (phonon) of the host lattice. As the excited center will prefer to lose its energy non-radiatively to a nearby lattice defect, the luminescent centers are more favourable if they satisfy the following requirements.

In order to reduce the undesired defects and optimizes the emission efficiency of the luminescent centers, obtaining a good crystalline phosphor is necessary. Hence, the luminescent centers should be incorporated into a substitutional lattice site. On the other hand, the luminescent centers have a relatively high dopant level which tends to deteriorate the crystallinity. To avoid this, luminescent centers with both the geometric size and the valence that closely match with the host cations are more desirable. If there is a geometric mismatch, the dopant atoms will have to fit into a less efficient interstitial site, and if there is a valence mismatch, this will have to be compensated by an additional co-activator ion.

Besides, since the phosphor has to be subjected to a high applied voltage, stability of the luminescent centers under a high electric field of the order of 10^8V/m is required. A well-known example is the poor thin film EL performance of the donor-acceptor center associated with the copper doped ZnS; the same center is the activator in the efficient green CRT phosphor. This undesired phenomenon may be attributed to the unstable shallow donor and acceptor levels in high electric fields because electrons can tunnel out of these levels. And so suitable luminescent centers are those with deep energy levels, i.e. isolated luminescent centers. Typical luminescent centers found to be suitable are transition-metal ions, such as Mn (yellow), and rare-earth ions, for example, Tb (green), Sm (red), Eu (red), Ce (blue-green) and Pr (white).

2.3.2 The insulating layer

For ACTFEL devices, the insulating layers sandwiching the phosphor layer are quite important for proper device operation. The most important role of the

insulating layers is to protect the phosphor layer from large currents that flow when the phosphor is driven to electrical breakdown. The importance for the insulating layers can be realized as follows.

The electroluminescence of the phosphor layer is always associated with the dielectric breakdown of the phosphor. At low fields, the phosphor layer has high resistivity and is essentially an insulator. However, at critical electric field, the current increases very rapidly with voltage and simultaneously electroluminescence is observed. If such a breakdown exhibits a negative resistance characteristic or if any non-uniformity forms in the thin phosphor layer, a region with slightly lower threshold field that prevails for the major portion of the film could draw vastly more current and lead to the formation of a permanent short circuit. The purpose of the insulating layers and the applied field in AC operation is to let the device swept through the threshold field periodically, then only a limited amount of charge per unit area can pass through the active phosphor layer. In this way the dissipation or heating is limited to an acceptable level throughout the films and catastrophic failure is essentially avoided.

In addition, the insulating material being used must satisfy critical mechanical requirements in term of adhesion and stress over process temperatures that range up to 550°C. Furthermore, they must prevent ionic diffusion of foreign species into the phosphor layer. Also the materials should provide interface states at the boundary of the phosphor layer and the insulating layer, so that sufficient electrons are injected from these interface states into the conduction band of the phosphor layer through tunneling when the applied field is larger than the threshold electric field. The generally accepted requirements of insulators for ACTFEL applications are as follows: [Ono, 1995]

1. high dielectric constant, $\varepsilon_o\varepsilon_r$
2. high dielectric breakdown electric field, E_{BD}
3. small number of pinholes and defects
4. good adhesion to the electrodes and phosphor layer
5. small loss tangent, tan δ

With the same argument made in equation 2.4, the ratio of C_i and C_{ph} is very important in determining the efficiency of the voltage drop across the phosphor layer. The equation suggests that $C_i >> C_{ph}$ is preferred, since the capacitance of the insulating layers depends on the relative dielectric constant, ε_r, which implies that the relative dielectric constant of the insulating layer should be as large as possible, while the thickness should be as small as possible. However, compromises have to be made because there are practical limits to both the size of insulator dielectric constant and the insulator thickness. Charge leakage for insulators thinner than about 500 Å has been reported which degrades the device performance. [Keir et al., 1996] Also, when the device is turned on, the phosphor layer becomes virtually short circuited. Consequently the additional voltage applied above the turn-on voltage is suddenly dropped across the insulating layers, so that the thinner insulators will be subjected to higher electric fields than the thicker insulators. Therefore, the insulating layers must possess significant breakdown fields if they are to be useful for ACTFEL application. However, the high-dielectric constant materials generally have fairly low breakdown fields and vice-versa. A value of figure of merit is introduced to characterize the dielectric materials for insulating layers [Howard, 1977]. This figure of merit is the product of dielectric constant and breakdown electric field, $\varepsilon_o\varepsilon_r E_{BD}$. This figure of merit is equal to the maximum trapped charge density Q_{max} at the phosphor layer/insulating layer interface.

In addition, it has been found that thin-film EL insulating layers exhibit two distinctly different film breakdown patterns. One pattern is a propagating arc that destructively grows in size until significant microscopic damage is done to the films (so called "propagating breakdown") which usually occurs in those insulators with relative dielectric constants above 40. The other pattern is the so called "self-healing" localized discharge that clears the film defect by causing a microscopic open circuit to occur around the breakdown site, and hence, do not grow in size. Because all thin film devices have some microscopic defects, it is desired that the insulating materials have self-healing breakdown characteristic.

Pinholes and defects in an insulator should be as few as possible because the display panel is large in size, and pinholes and defects will certainly degrade the quality of the display. Problems are more serious for propagating breakdown mode insulators for which the pinholes and defects can lead to catastrophic failure of the display. Also good insulator adhesion is certainly necessary for prolonging the lifetime of ACTFEL display.

The insulators in an ACTFEL device should have a small loss tangent, tan δ. The loss tangent is a measure of the dissipative characteristics. The larger the loss tangent, more charges will be leaked through the insulators. This reduces device efficiency by consuming more power.

2.4 Drive methods

The light emitting mechanism of thin-film EL displays with the double-insulating-layer structure requires alternating polarity of the driving electric field for efficient light generation. This display has to be driven with an AC drive method. A typical thin-film EL is an XY-matrix display with M vertical columns and N horizontal rows, as shown schematically in figure 2.3.1. The cross sections of the X and Y electrodes form the picture pixels of the thin-film EL devices. X electrodes correspond to column electrodes or data lines, and Y electrodes to row electrodes or scan lines.

Table 2.3.1 describes the selection states of the pixels and the voltage across them when a single pixel P(i,j) in the XY-matrix electrode system is addressed. The electrodes not being addressed are in a floating state and M, N >> 1. For the M=N case, a voltage of the half-selected pixels becomes $V_a/2$. With the sharp non-linear luminance vs. voltage (L-V) characteristics, $V_a/2$ can be taken much smaller than the threshold voltage V_{th}, so that no EL emission occurs at the half-selected and non-selected pixels. Drawbacks are the rather high drive voltage ranging from 180 to 240 V in commerical displays, and the substantial capacitance of the thin-film EL structure,

which implies significant displacement currents.

There are two refresh-type drive methods for XY-matrix EL displays:

1. Multiplex drive method where each scan line is addressed during the dwell time t_s defined by $t_s = 1 / Nf$ (line-at-a-time drive scheme), where N is the number of scan lines and f is the drive frequency or drive frame rate.
2. Active matrix method using an active device such as a thin-film transistor (TFT) attached to each pixel.

In the line-at-a-time type driving method, image is formed by scanning of X-Y matrix. A write voltage V_w just below or equal to the device threshold voltage is applied to the selected row (scan line) and at the same time the data information is applied to all columns (data lines), as modulation voltage V_M. When a pixel receives both the write and full modulation voltages (V_w+V_M), the pixel is fully turned on. Scanning of the whole display is performed at least 60 times a second, giving a frame rate of 60 Hz. For example, a 400-scan lines driven at 60 Hz, the dwell time for each scan line t_s requires 40 μs. For a large scan lines, this drive method suffers from a low duty-ratio driving, resulting in low luminance and occurrence of flickers.

In the active matrix method, memory effect is installed to drive circuits for each pixel, so that the number of scan-lines is not a problem even in the refresh type EL displays. However, since an EL display is a capacitive display driven at high voltage, it is necessary to fabricate high-voltage, large-current active drivers in a small area inside each pixel. Advanced IC technology on the active driver capable to operate at high voltage with good reliability is necessary for EL displays and it is expected to be costly.

The information on one data line (column electrode) is determined by the data input to column drivers. The column voltage at the intersection with row electrode is indeed affected by the resistivity of column electrode and the capacitance of thin-film EL structure because pixels along the column form a RC network. One of the suggestions requires the resistivity of column electrodes must be as low as possible.

The purpose is to reduce the RC product to be much shorter than the dwell time per scan line [Mellor et al., 1984]. On the other hand, the whole line of a row electrode has to be written "at a time" which determine the conductivity of row electrodes. That means the row drivers must be able to charge the capacitor formed by the pixels along the scan line within a few microseconds, and therefore row electrodes must be made of good conductor.

Since the RC product determines the refresh rate of the whole EL device, reducing the resistivity of the column and row electrodes is one of the methods. The other consideration would be reducing the capacitance of the insulating component. However, in ACTFEL devices, insulating layers with higher dielectric constant are preferred for more efficient and brighter electroluminescence, and this contradicts with the idea of reducing capacitance. Ferroelectric materials, on the other hand, possess a polarization-electric field (PE) hystersis loop, i.e. the occurrence of dynamic change of dielectric permittivity with the applied AC voltage. This implies a larger permittivity during steep switching of polarization at the coercive field while smaller permittivity at other time. By selecting an appropriate driving voltage in the following XY-matrix (Fig. 2.3.1), we might gain a faster refresh rate for EL devices. For example, we set the applied voltage along the ith column V_i to be slightly larger than half of the coercive voltage. At the same time, a negative $-V_i$ is applied along the jth row while remain rows have zero potential. Along the ith column, the capacitance of the P(i, k) ($k \neq j$) displays are small due to a field smaller than coercive field. However, the P(i, j) display has a large capacitance due to a larger field ($\equiv$ coercive field). Hence the total capacitance along ith column mainly arises from one display unit. This is different from using dielectric material as insulating layer where the capacitance of the ith column is the sum of all the display units along ith column. This approach may be a potential to relieve the problem due to the intrinsic RC network in the XY-matrix design, and that is the motivation led us conducting the research to explore the possibility of this concept.

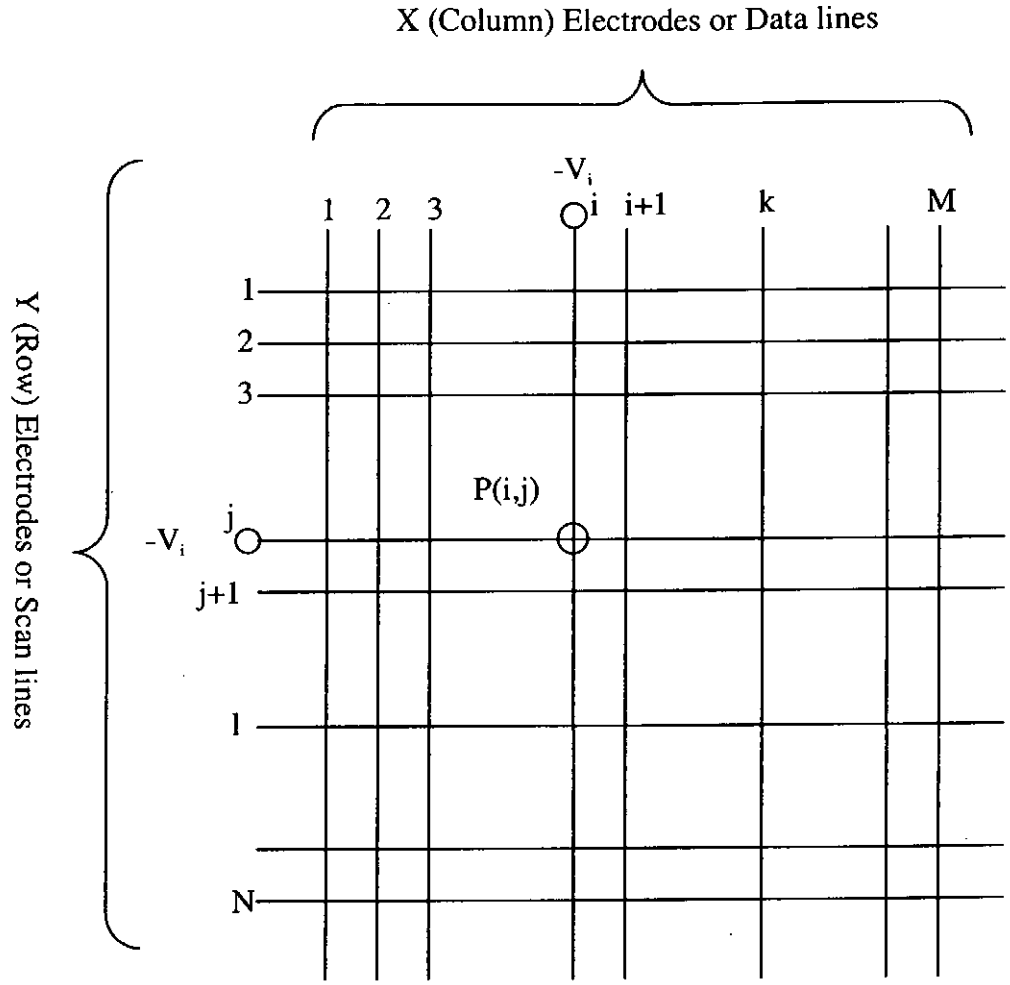

Figure 2.3.1 XY-matrix electrode system of a typical thin-film EL display

Pixel	State of selection	Pixel voltage
P(i, j)	Selected	$V_S = V_a$
P(i, l≠j)	Half selected (Data (X) line)	$V_{HX}=V_a \times M/(M+N)$
P(k≠i, j)	Half selected (Scan (Y) line)	$V_{HY}=V_a \times N/(M+N)$
P(k≠i, l≠j)	Non selected	$V_N=0$

Table 2.3.1 Selection states and pixel voltages of matrix display panels

CHAPTER 3

PULSED LASER DEPOSITION (PLD)

The need of various optic and electronics devices, including electro-optic, spatial light modulators and many others has greatly stimulated the investigation on the fabrication of thin films. The development of deposition techniques for the preparation of thin films with controlled, reproducible, and well-defined properties plays an increasingly important role in technological applications. General speaking, deposition techniques can be broadly classified as physical and chemical methods. Chemical depositions involve chemical reactions and/or exchanges during film formation; metal-organic chemical vapour deposition and sol-gel fabrication are examples of this technique. On the other hand, physical vapour deposition (PVD) only involve physical transfer of material from a target to the surface of a substrate; typical examples of PVD include sputterings, molecular beam epitaxy (MBE), and pulsed laser deposition (PLD).

Growing various thin films, in particular, oxide films, using PLD technique has been well studied in our group. [Wu et al., 2000] Hence, in the present studies, PLD is utilized for fabrication of several layers of thin films. In this chapter, we will first describe the historical development of PLD, and its advantages and disadvantages. Finally, a brief description of basic mechanism of PLD will be presented.

3.1 Historical development of pulsed laser deposition

Since the first ruby laser constructed in 1960 by T. H. Maiman at Hughes Research Laboratories, interests on experimental investigation of laser-material interaction was initiated. The earliest experimental study using laser to ablate material can track back to 1962 [Chrisey et al., 1994]. In that study, Brech and Cross used ruby-laser to ablate metal and studied the emitted light. Since then, vast studies on the interactions of intense laser beams with solid surfaces [Ready, 1963], liquids [Askar'yan et al., 1963] and

gaseous materials [Meyerand et al., 1963] were performed. Their results suggested that intense laser radiation could vaporize materials so that film deposited by pulsed laser was possible. This idea for deposit thin films was finally demonstrated by Smith and Turner in 1965 [Smith et al., 1965].

In 1970's, the invention of electronic Q-switch and the development of high efficiency second harmonic generator brought PLD to a new era. The former one can deliver short pulses with very high peak power density exceeding 10^8 W/cm^2 while the latter one makes laser able to deliver shorter wavelength radiation. These two developments make laser ablation to be suitable for high quality film growth. Furthermore, Gaponov deposited oxide films in an oxidizing ambient in late 1970's [Gaponov et al., 1979]. This so called reactive deposition technique is regarded as the foundation for the in-situ growth of high T_c superconductor and ferroelectric films using PLD.

The second breakthrough of PLD in late 1980's was triggered by the successful growth of high T_c superconducting films. The pioneering work was done by Venkatesan of Bellcore [Dijkkamp et al., 1987]. The experiment had proved that PLD method is an affordable technique to explore new frontiers in material science. Since then, interest has been sustained and broadened by the concurrent development of high-power pulsed ultraviolet (UV) excimer lasers that are reliable and convenient to use.

3.2 Advantages and disadvantages of pulsed laser deposition

PLD possesses two main advantages over other techniques. Firstly, from the setup point of view, one of its uniqueness is the application of laser as the source for material evaporation. Lasers are clean and introduce minimal contamination from the heat source. So, film contamination from the support material is reduced because of the surface evaporation characteristics of the beam. Simultaneous or sequential multi-source evaporation can be done easily by directing the laser beam with external mirrors or by proper arrangement of the deposition chamber, and so in situ growth of multi-layer films

is possible. Furthermore, the setup is relatively simple. The laser source is kept outside the vacuum system and this reduces the sophisticated mounting and arrangement in the vacuum system. Unlike thermal and electron beam evaporation, PLD system is absence of electron beams or hot filaments in the vacuum system. So PLD has an enormously valuable natural capability for reactive deposition in ambient gases.

Secondly, from the consideration of ablation mechanism and film formation, PLD has the potential to growth quality film of any material. The reasons are as following:

1. With the high power densities obtained by focusing the laser beams, high melting point materials can be vaporized. Also an extremely high heating rate of the target (10^8 K/s) leading to congruent evaporation at high deposition rates, which is an essential parameter for the synthesis of polycomponent thin-film materials.
2. The laser ablation at high laser fluence generates a high energy of plasma particles (10-1000 eV) [Saenger, 1993] (in form of ground- and excited state atoms and ions, together with electrons). This high-energy plume can increase the adhesion abilities and adatom surface mobilities, and enhance film nucleation via energy-enhanced chemical reactions. Consequently, epitaxial growth of thin film is possible at reduced substrate temperature.
3. Extremely high pulsed deposition rates (>10^5 nm/s) which result in a specific growth mechanism and a high packing density of the deposited films.
4. The allowance of relatively high ambient gas pressure can modulate the ablation beam's kinetic energy through the collisions between the ablated species and the ambient gas molecules. This is useful to avoid defects induced by too high energy species' bombardment to the deposited films. Also by filling different gas and pressure, optimized films quality can be obtained or even been used to manipulate different properties of the films. [Chrisey et al., 1994]

However, there are still some disadvantages impeded the PLD for the thin film technology. First of all, since the plasma plume generated from the pulsed laser ablation of solid targets always has a 'forward peaking' performance, the angular distribution

profiles of the deposited materials are narrow. This limits the uniformity of the deposited films on the substrate. The problem of scaling up the PLD process to coat large substrates compatible with industrial applications is still remained to tackle with. Another drawback of PLD is the generation of particulates on the substrates. The nature of these particulates, including the generation rate, the energy or velocity, the size, the chemistry and microstructure, depends upon the process conditions as well as the target material. The presence of particulates of micro size has the adverse effect especially on the nano-scale thin films.

3.3 Mechanisms of pulsed laser deposition

In contrast to the simplicity of the hardware, the working principle of PLD is a very complex physical phenomenon. The mechanisms involve multidiscipline of knowledge including laser characteristics, target materials properties (such as optical, topological, and thermodynamical properties), the laser-material interaction, the evaporated plume dynamic in vacuum and gas environment, film growth mode on the substrate, properties of substrate and target materials such as lattice parameters, thermal expansion parameters, chemistry, and much more. But in general, the thin film formation process in PLD can be divided into four stages:

1. Laser radiation interaction with the target,
2. Dynamics of the ablation induced plume (plasma),
3. Interaction of the ablation induced plume with the substrate, and
4. Nucleation and growth of a thin film on the substrate surface.

Each stage will make different contributions to the film formation. The first and the third stages are particular important for the synthesis of polycomponent materials; while, the second and the fourth stages will influence the characteristics and properties of the deposited films. The contribution of each stage is described briefly as follow.

3.3.1 Laser radiation interaction with the target

Laser radiation interaction with the target is particularly concerned with the ablation of target material under high laser fluence. The mechanism of laser ablation is very complex and typically falls on a continuum between the limits of 'thermal' and 'non-thermal'. In this stage, the laser is focused onto the surface of target material. The irradiant on the opaque target is partially reflected and partially absorbed by the surface layer. The ratio depends on the wavelength of laser and the optical properties of the target material. Absorption of this intense light energy leads to local heating and evaporation of target material. At sufficiently high flux densities and short pulse duration, all elements in the target are rapidly heated up to their evaporation temperature. Materials are dissociated from the target surface and ablated out with stoichiometry as in the target. The ablation mechanisms involve many complex physical phenomena such as collisional-, thermal-, and electronic-excitation, exfoliation and hydrodynamics.

3.3.2 Dynamics of the ablation induced plume (plasma)

The emitted materials tend to move towards the substrate according to the laws of gas-dynamic and show the forward peaking phenomenon [Namiki et al., 1986]. Singh et al reported that the spatial thickness varied as a function of $cos\theta$. [Singh et al., 1990] The spot size of the laser as well as the plasma temperature has significant effects on the deposited film uniformity. The target-to-substrate distance also governs the angular spread of the ablated materials. The spread of the plume would ultimately affect the profile and homogeneous of the film.

3.3.3 Interaction of the ablation induced plume with the substrate

Both the quality and the stoichiometry of thin films primarily depend on this interaction. The mechanism of this interaction is illustrated in figure 3.1. The

energetic species sputter some of the surface atoms forming a collision region between the incident flow and the sputtered atoms. After the formation of this thermalized region that serves as a source for condensation of particles, film starts to grow. When the condensation rate is higher than the sputtering rate, thermal equilibrium condition can be reached quickly and film grows on the substrate surface at the expenses of the direct flow of the ablation particles.

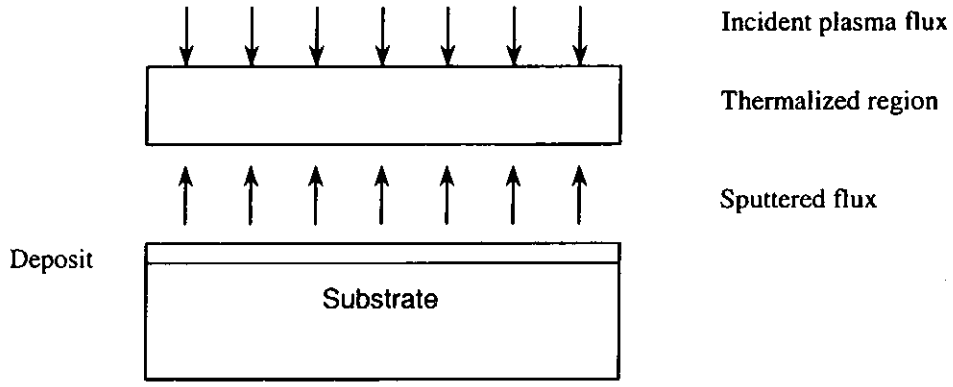

Figure 3.1 Schematic diagram of plasma-substrate interaction

3.3.4 Nucleation and growth of a thin film on the substrate surface

Nucleation and growth of crystalline films depends on many factors such as density, energy, ionization degree, types of condensing material, temperature and substrates' physico-chemical properties. The two main thermodynamic parameters for the growth mechanism are substrate temperature T and supersaturation Δm. They can be related by the following equation

$$\Delta m = kT \ln(R/R_e)$$

where k is the Boltzmann constant, R is the actual deposition rate, and R_e is the equilibrium value at the temperature T.

The nucleation process depends on the interfacial energies between the three phases present – substrate, condensing material and vapour. The minimum-energy shape of a nucleus looks like a cap, and the critical size of the nucleus depends on deposition rate and substrate temperature. For large nuclei, a characteristic of small

supersaturation, the nucleation process creates isolated patches (islands) on substrates. These patches subsequently grow and coalesce together. As the supersaturation increases, the critical nucleus shrinks until its height reaches atomic diameter such that its shape is two-dimensional. For very large supersaturation, the layer-by-layer nucleation will happen for incompletely wetted foreign substrates.

The crystalline film growth depends on the surface mobility of adatom (vapour atoms). Normally, the adatom will diffuse through several atomic distances before sticking to a stable position within the newly formed film. The surface temperature of the substrate determines the adatom's surface diffusion ability. High temperature favors rapid and defect-free crystal growth, whereas low temperature or large supersaturation crystal growth may be overwhelmed by energetic particle impingement, resulting in disordered or even amorphous structures.

Metev and Veiko [Metev et al., 1989] suggested that the N_{99}, the mean thickness at which the growing, thin and discontinuous film reaches continuity is given by the formula

$$N_{99} = A(1/R)^{1/3} \exp(-1/T)$$

where R is the deposition rate (supersaturation related) and T is the temperature of the substrate and A is a constant related to the materials.

In general, different materials in thin film form can be fabricated and studied by PLD. This makes PLD to be a powerful deposition technique in thin film research. The successful in the fabrication of superconducting thin films (YBCO) and ferroelectrics thin film are the most enlightenment to indicate the ability of PLD.

CHAPTER 4

EXPERIMENTAL SETUP AND MEASUREMENT

4.1 Pulsed laser deposition

4.1.1 The experimental setup of PLD

A typical PLD system is illustrated in figure 4.1.1. Krypton Fluoride (KrF) and Argon Fluoride (ArF) excimer laser with wavelength of 248 and 193 nm respectively (Lambda Physik COMPex 205) were used for thin film fabrication. The laser beam was directed and focused into the deposition chamber via an UV-grade mirror and a plano-convex lens. The mirror is a dielectric multi-layer coated laser grade optical glass that is high reflectivity of excimer laser line at 45° incident angle. The incoming beam was focused onto a rotating target inside the chamber at an angle of 45°. The windows of the chamber are made of UV-grade fused silica which allow up to 90% transmittance of the excimer laser.

For film deposition, the chamber can be evacuated down to ~10 mTorr using a mechanical rotary pump (ULVAC D-330K) and to a higher vacuum of $5x10^{-7}$ Torr via a cryro-pump (CTI-CRYOGENICS CRYO-TORR 8). In addition, by using a diffusion pump (ULVAC F250) together with a mechanical pump, the chamber can also be evacuated to around $2x10^{-5}$ Torr. The pressure of the chamber was monitored by a manometer (MKS Baratron Type 122A) in the range from 10 to 0.001 Torr, while for pressure lower than 0.001 Torr, an ionization gauge (ULVAC type WIT) was employed.

The targets being ablated were mounted about 3.5 to 5 cm in front of the substrate holder. Depending on the chamber setup, targets were usually fixed with a rotating shaft through the center, so that the laser beam would ablate the circular surface of the targets. In situ multi-layers fabrication could be achieved by slide in and out the shaft

for target selection. Other variance was to mount the target on a holder with the plane surface facing the substrate and was ablated by the laser beam. (Figure 4.1.1b) The laser induced plasma plume from the target was aligned normally towards the substrate.

The substrate holder was equipped with a heating filament that can heat up to 750°C. A K-type (Nickel-Chromium, Nickel-Aluminium) stainless steel shielded thermocouple was employed for monitoring the temperature. The heating filament being used was Kanthal wire (25% chromium, 5% aluminium, 3% cobalt and 67% iron) of 0.559 mm in diameter and the resistance per unit length is 5.1 Ωm^{-1}. Total resistance of the Kanthal wire was 15 Ω. The heating process was controlled by a PID controller (Shimaden SR-19) and a power regulator (PAC25-0321). The substrates were secured on the holder by silver paint in order to ensure a good thermal contact between the substrate and the holder. However, surface temperature different from the read value would be expected due to heat loss and temperature gradient. Flowing gas of O_2 or Ar could be filled into the chamber during the deposition processing.

4.1.2 Procedure of fabricating thin films by PLD

In our studies, both the insulating films ($BaTiO_3$ and PZT films) and the conducting films (LNSMO films) was fabricated by the KrF excimer laser, while ArF excimer laser was used for the ablation of the phosphor films i.e. ZnS:Mn films. In addition, different substrates including Si (001) wafer, $LaAlO_3$ (LAO) (001) substrate and ITO-coated glass had been used for the fabrication of these films, therefore, the fabrication processing parameters were various from one particular film to the others. Hence the description below would be applied to the fabrication of $BaTiO_3$ films on LAO substrates, and the others will leave to more detail discussions in corresponding chapters.

To fabricate $BaTiO_3$ films, $BaTiO_3$ target was first mounted into the chamber. The laser fluence being used was about 6 J/cm^2 with the spot size around 5 mm^2. The LAO(001) substrate was ultrasonic cleaned in an acetone bath and then secured onto the holder face plate by silver paint. The holder was then mounted inside the chamber and placed in front of the target 4.5 cm away. The chamber was roughly evacuated by a mechanical rotary pump and ultimately reached a background pressure of 10^{-5} Torr using a cryo-pump. The substrate was then heat up to 700°C and slowly filled with O_2 gas to 200 mTorr for deposition procedure. KrF excimer laser operating at a repetition rate of 10 Hz was used. The thickness of the deposited films was estimated by the deposition time. The final thickness of the deposited films was measured by a surface profiler. In our experiments, thickness of the films was found to be around 200 nm for 3 minutes deposition. After deposition, the film was undergoing in-situ annealing for 2 hours under 200 mTorr O_2 and then cooled down to room temperature under the same ambient O_2 condition.

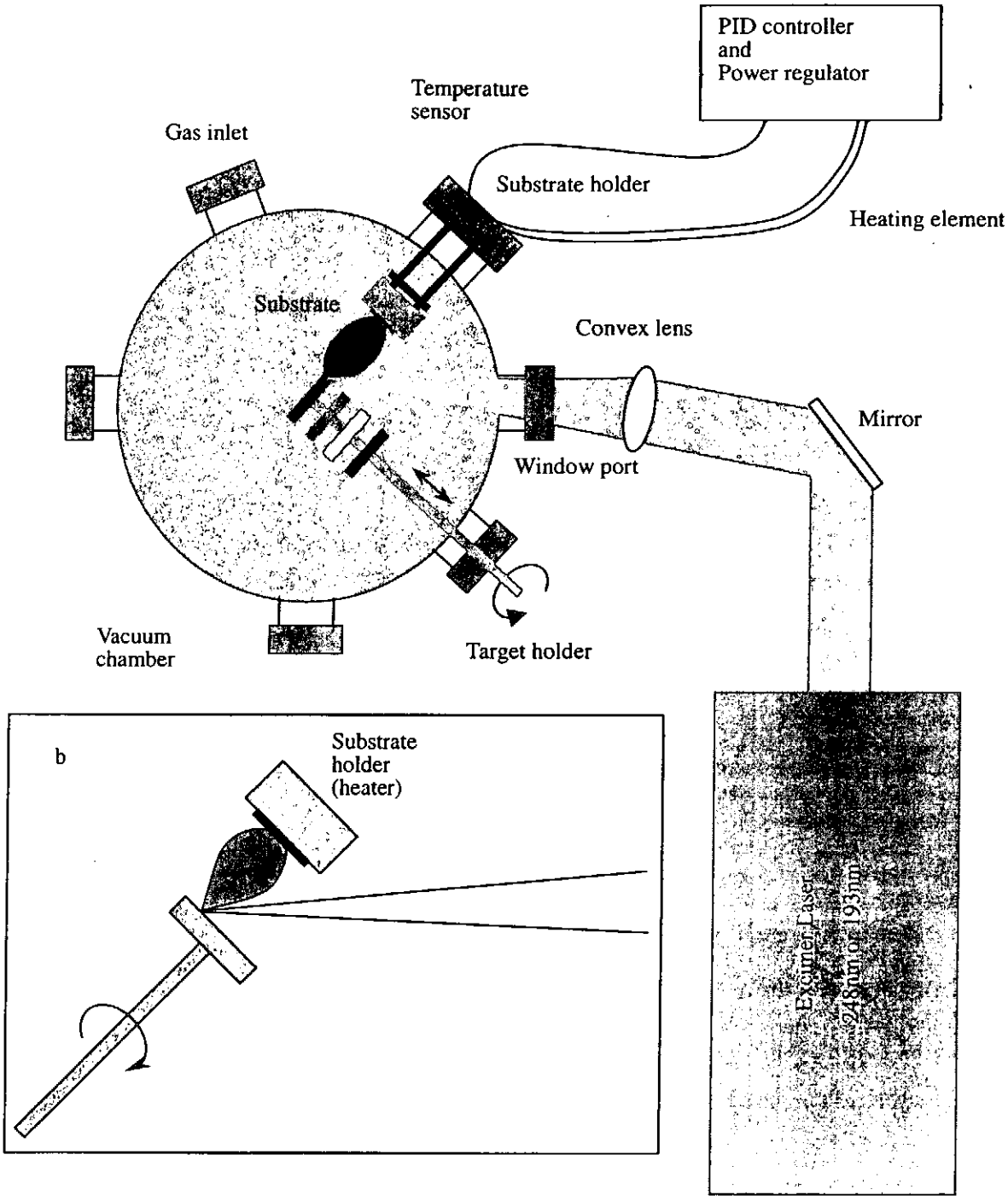

Figure 4.1.1. Schematic layout of the PLD set-up. The geometry in the box showed the other variance of the setup.

4.2 Sample characterization and measurements

4.2.1 Structural characterization

4.2.1.1 X-ray diffractometry (XRD)

X-ray diffractometry (XRD) is a common and non-destructive method for characterization of crystal structure and determination of atom location of various materials in bulk solids, powders, or thin films form. It has been extensively used to investigate the qualities of PLD films. The XRD system used in this study was a Philip X'pert system using Cu K_α radiation (λ = 1.54Å) operating both in four-circle and Bragg-Brentano (θ–2θ) geometries. The radiation from Cu K_β was filtered by a Ni filter.

The X-ray radiation from the X-ray source interacts with the atoms and makes the atoms polarized as an atom's negatively charged electrons and positively charged nucleus experience forces in opposite directions. Hence the charge distribution equivalent to the electronic dipoles and its polarization oscillates with the alternating electric field of the exerting electromagnetic (em) wave with the same frequency ν. The oscillating dipoles in turn radiate em waves of frequency ν, and the waves propagate in all direction. And in wave terminology, the X-ray scattered in all directions after interaction. The radiation scattered from one atom interacts destructively with radiation from other atoms except in certain directions like figure 4.2.1. In these directions, the scattered radiation is reinforced rather than destroyed. From the diagram, a constructive interference happens when

$$AB + BC = n\lambda\,,\ n = 1,2,3,\ldots$$

and because $AB = BC = d\sin\theta$, it follows Bragg's Law

$$2d\sin\theta = n\lambda\,,\ n = 1,2,3,\ldots$$

where n is the order of the intensity maximum, λ is the X-ray wavelength, d is the interplanar spacing, and θ is the angle of incident of X-ray beam.

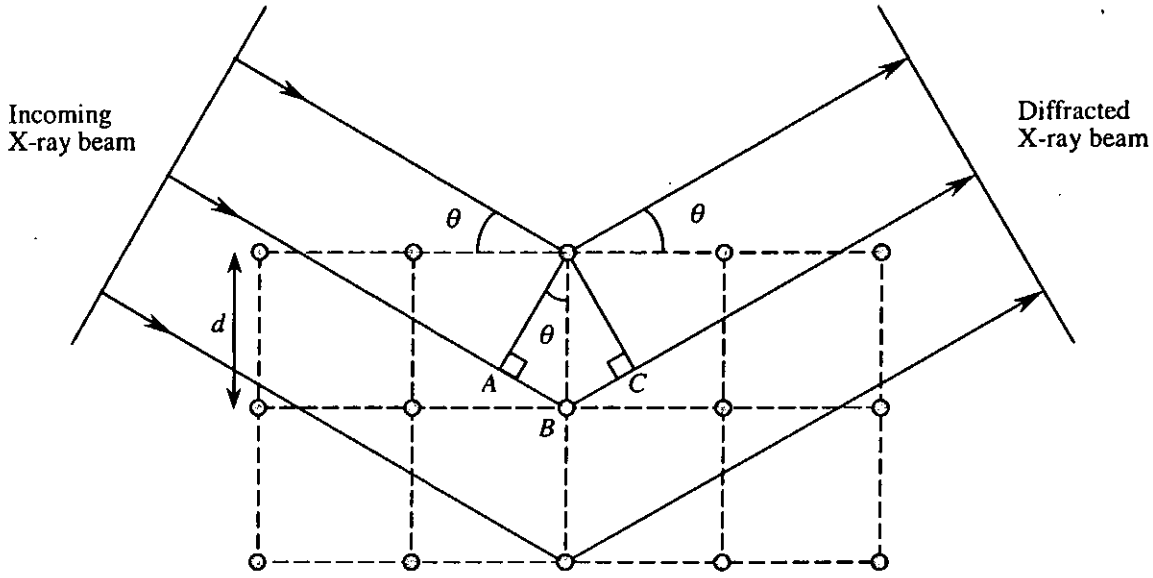

Figure 4.2.1 Bragg diffraction of X-rays from successive planes of atoms. Constructive interference occurs for ABC equal to an integral number of wavelengths.

The interplanar spacing for a simple cubic structure can be determined by the following equation

$$d = \frac{a}{\sqrt{h^2 + k^2 + l^2}}$$

where a is the lattice constant of the crystal structure and h, k and l are the reciprocal lattice indices for a, b, c axis respectively.

The experimental geometry of X-ray diffractometer (XRD) is illustrated in figure 4.2.2. It shows the X-ray source, different kinds of slits, monochromator and detector. Also, there are four rotating axes of θ (ω), 2θ, χ and ϕ for different scan modes. All different scan modes, θ–2θ, ω and ϕ scans, were utilized to investigate the crystal structure of the films in this project.

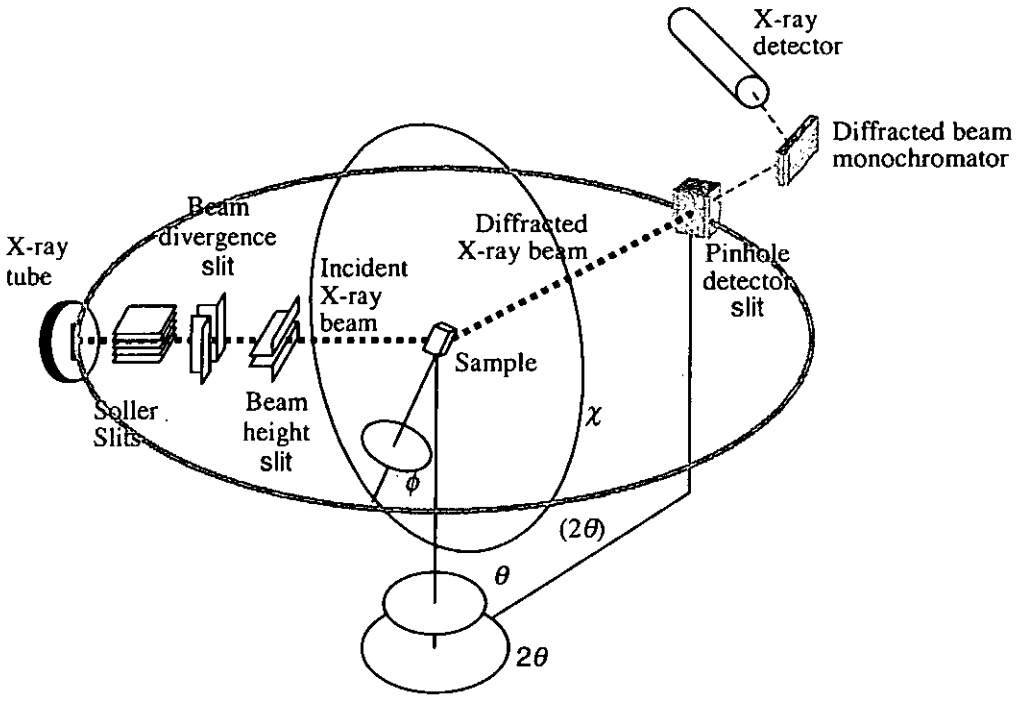

Figure 4.2.2 Experimental geometry, showing four primary axes of goniometer, X-ray tube, detector and slits

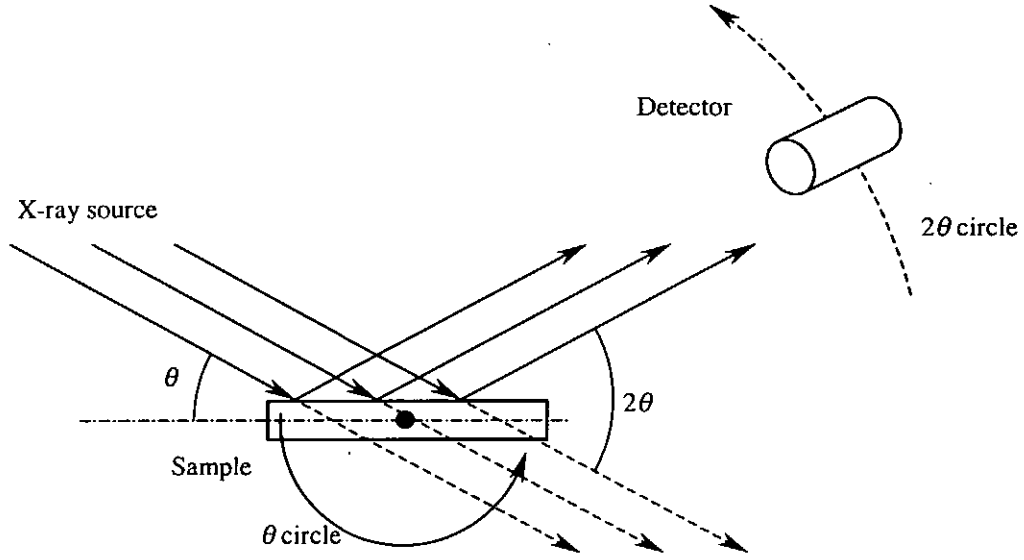

Figure 4.2.3 The schematic diagram of θ–2θ scan, the moving angle of the detector is twice of that of the sample

In the θ–2θ scan, the X-ray source is fixed at a position. While the sample rotates a certain angle with respect to the X-ray beam axis, the detector rotates twice of that angle as shown in figure 4.2.3. It allows the detector to follow the reflected ray and to receive the strongest signals from the zeroth order diffraction. The

constructive diffraction lines reflect the crystal structure of the materials under investigation. With appropriate calculation, information like crystalline phases and orientations can be determined.

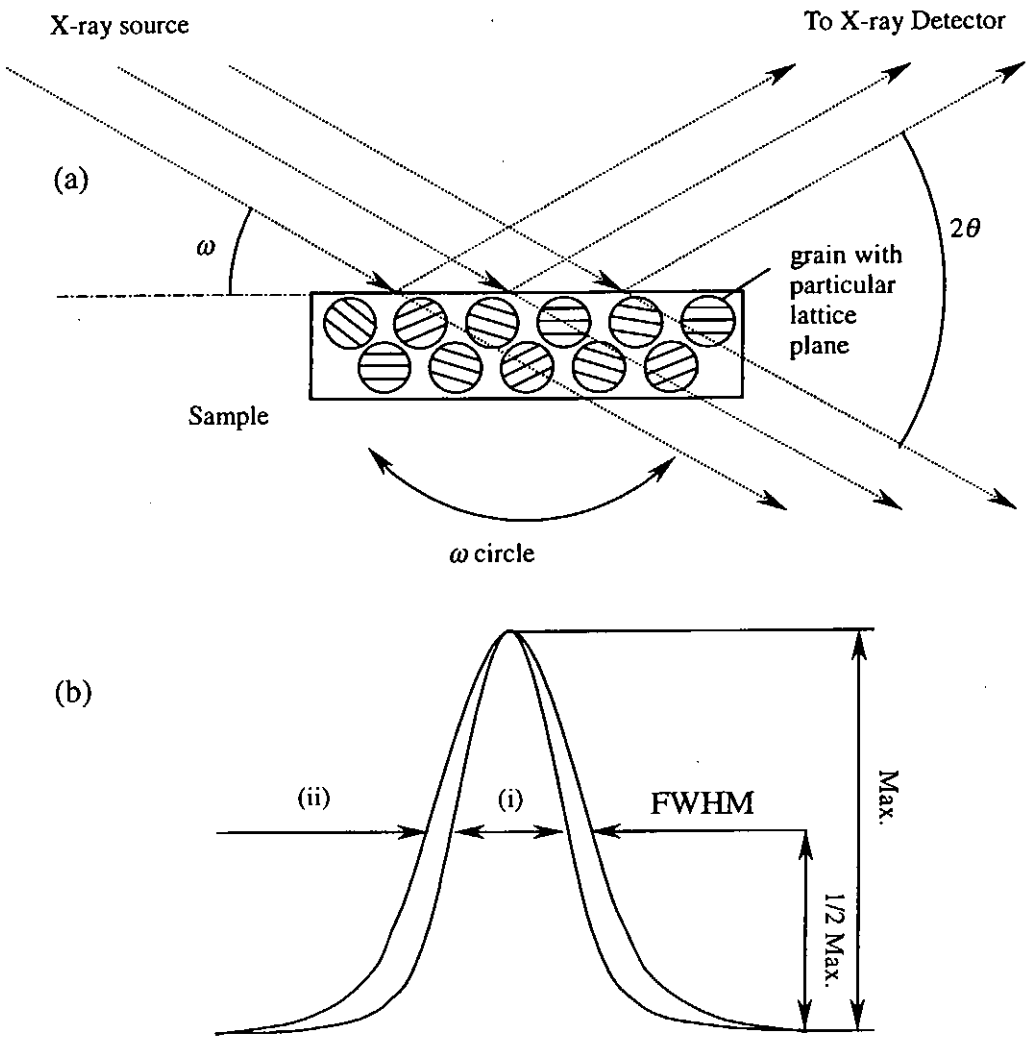

Figure 4.2.4 (a) The FWHM of ω scan reflects the alignment of different polycrystalline at a particular orientation. (b) FWHM of narrow and board rocking curve.

The θ–2θ scan, however, only gives information on the out-of-plane crystalline orientations of the film but cannot give quantitative measurements of orientations i.e. the degree of random orientation of the crystal grains with each other in the films. ω scan, on the other hand, could help to retrieve this information. Grains with different orientations in a thin film examined by ω scan mode are shown in figure 4.2.4 (a). The X-ray source and detector are fixed at certain θ angle for a particular orientation of the crystal plane reflection, the sample is then rocked along the ω axis. The strong

diffraction occurs only when a particular plane of the grain is aligned at the angle matched the Bragg's Law. Therefore, a broader profile will be obtained for worse-aligned grains in the same direction than a better-aligned one. Often the ω scan profile is referred as the rocking curve. In general, the full width at half maximum (FWHM) of the rocking curve is used as a parameter to determine the quality of film orientation, which is shown in figure 4.2.4 (b). The narrow profile (i) with smaller FWHM means a better film quality in orientation. On the other hand, the broad profile (ii) suggests a bad film quality. Usually, if FWHM of the rocking curve is less than or around 1°, the film can be considered as highly oriented. For comparison, the FWHM of ω scan of single crystal like LAO or silicon is about 0.2° in our XRD characterization system.

For powder, polycrystalline bulk materials and polycrystalline thin films with random crystal-plane orientation, θ–2θ and ω scan could provide adequate information for the structure properties. However, for single crystal substrate and high quality thin films especially for epitaxial films, the above two methods can only provide limited information of crystal planes paralleled to the surface and out-of-plane lattice spacing characteristics. For high quality thin films with single-phase orientation observed in θ–2θ profiles, in-plane crystallinity feature would be critical to determine whether the films are epitaxially growth on top of the single crystal substrate or its just randomly oriented along the plane. To retrieve this information, ϕ scan certainly would suit this purpose. Figure 4.2.5 shows the schematic diagram of the principle of ϕ scan. For a film with simple cubic structure and only peaks of (001) families observed in θ–2θ profiles, the families of (101) planes would be the signals being looking for. The specimen is first tilted 45° along the χ axis relative to the normal plane, θ and 2θ angles are set to the particular angles for specific planes. Then a 360° ϕ scan is performed to investigate the peaks appeared and identifies its four-fold symmetric feature i.e. peaks with 90° apart. By comparing the (101) planes of the (001) cut substrate, cube-on-cube epitaxial film can be justified if both peaks from the film and substrate aligned at same angles. Other structures like tetragonal, it could

also show four-fold symmetry with different tilting angle of χ axis, depended on the ratio of the c/a ratio (longer lattice constant against the shorter ones) as well as the growth direction.

In our studies, all the above three scanning modes were used whenever suitable to characterize the films prepared including $BaTiO_3$ films on LAO substrate, $BaTiO_3$/LNSMO/LAO, PZT/LNSMO/LAO and ZnS:Mn films.

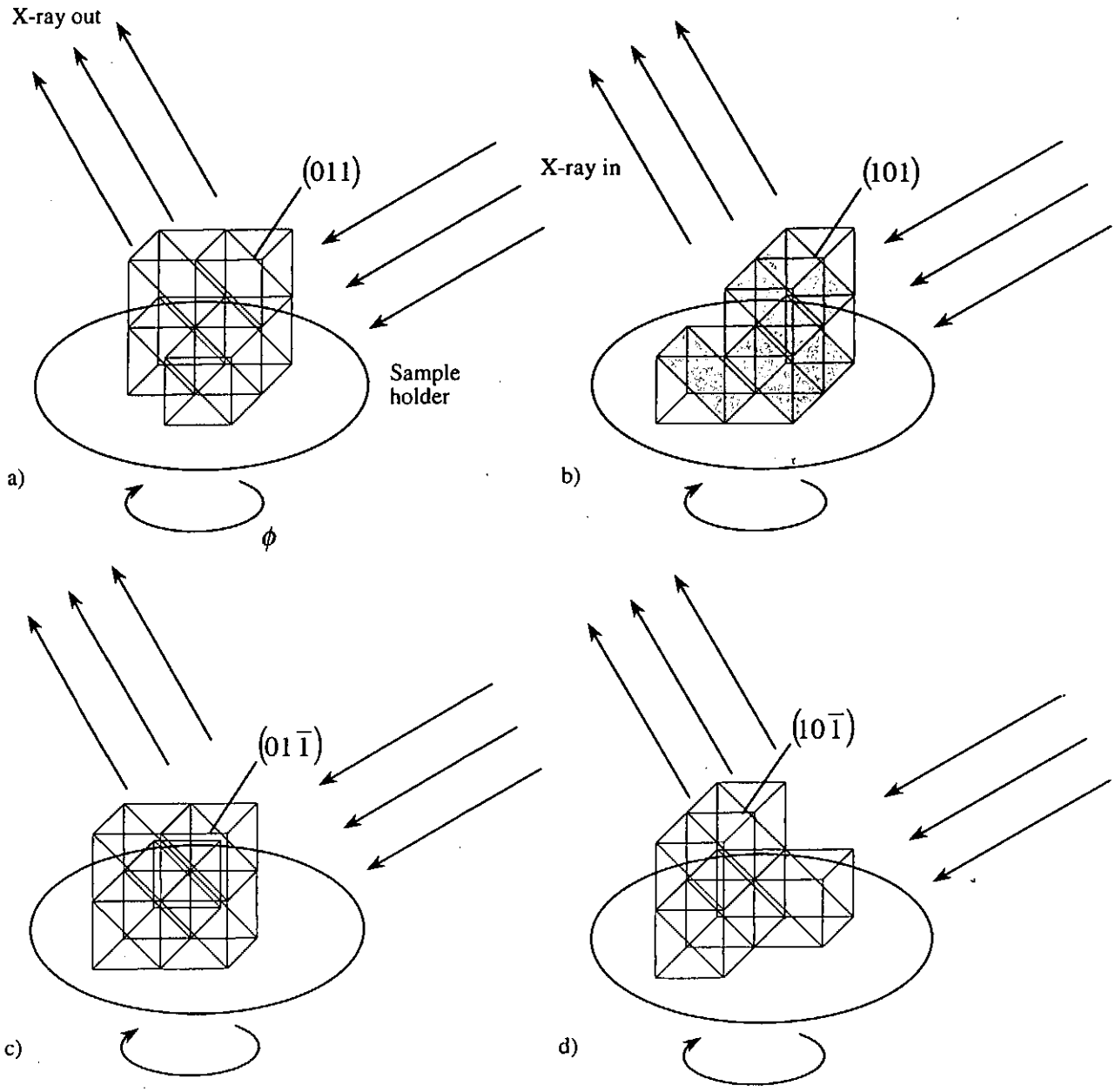

Figure 4.2.5 The illustrations of ϕ scan for the ϕ angles of 0°, 90°, 180° and 270° show the planes of (011), (101), $(01\bar{1})$ and $(10\bar{1})$ (not showing the tilting angle χ).

4.2.1.2 Scanning electron microscopy (SEM)

Beside structural characterization using X-ray differentometry, the surface morphology of our films was investigated by scanning electron microscopy (SEM, Leica stereoscan 440). Its principle maximum amplification is 300,000 so that grains size ~ 20-30 nm can be just resolved under this amplification.

The idea of electron microscopy is that in using energetic electron beam which have a shorter wavelength λ (about 0.1 nm) compared to light photons ($\lambda \approx$ 400-700 nm) used in optical microscope, a better resolution image could be obtained. In SEM, the detector collects electrons that are knocked out of the specimen atoms by the electron beam. The signal from detector is then amplified by circuitry and synchronized with the scan generator to produce an image. The schematic diagram of SEM is shown in figure 4.2.6. Electrons are generated from the cathode which is a heated sharp rod made of lanthanum hexaboride. After leaving the cathode and shield, the electrons are accelerated towards the anode. If the stabilization of the high voltage is adequate, electrons pass through the central aperture at a constant energy. The intensity and angular aperture of the beam are controlled by a condenser lens system between the gun and specimen. The beam after being minimized is deflected and scanned over the region that to be investigated in a raster pattern of lines by a magnetic field generated by a scanning deflection coil. The deflected beam is finally focused on the specimen by an objective lens through the correction elements of astigmatism, stigmator.

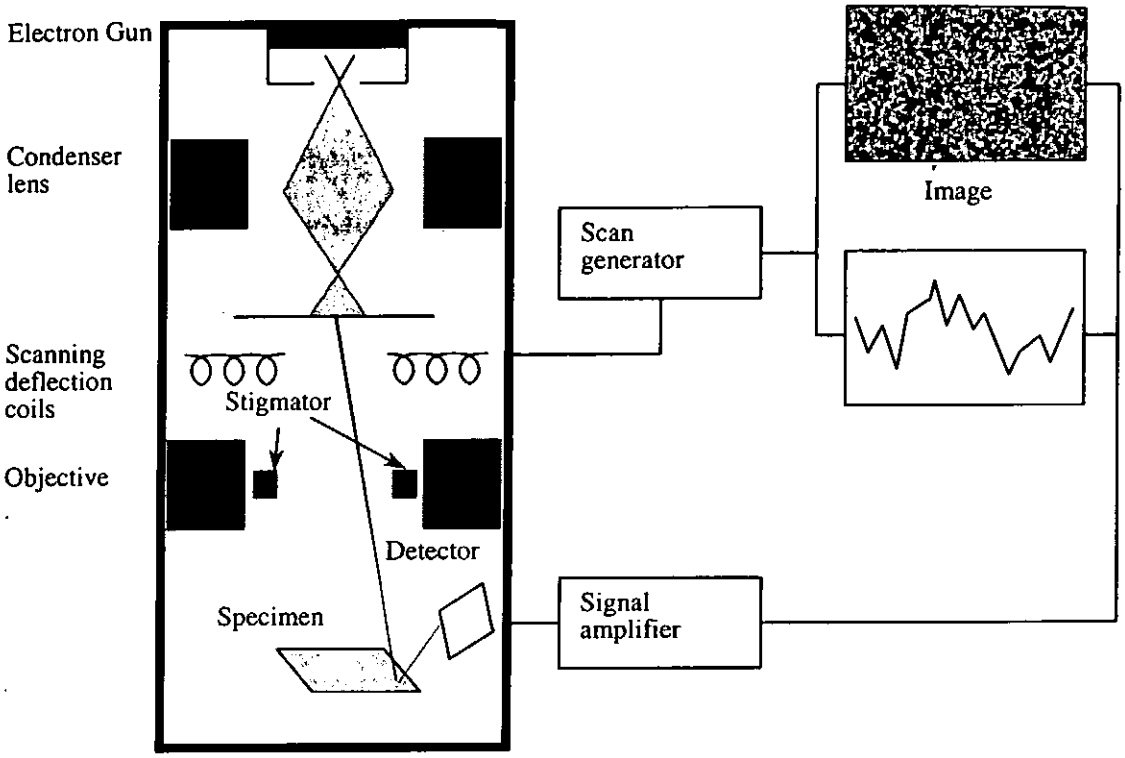

Figure 4.2.6 The simplified schematic diagram of scanning electron microscope.

The electrons that escape from the specimen basically are divided into backscattered electrons and secondary electrons. They are classified according to their energy. The energy for backscattered electrons is more than 50 eV while for secondary electrons is less than 50 eV. The backscattered electrons are generated by the elastic collision of the incident electron beam and the nucleus of the specimen. In the collision the direction of the beam electron is changed but the energy exchange is very small and usually less than 1 eV. On the contrary, the secondary electrons come from the inelastic collision of electron. The interaction in this inelastic collision results in the transfer of a few electron volts of energy to the conduction band electrons. Because of a large difference between escape depth of them, for backscattered electron the escape depth is sub-micron while for secondary electron it is at the order of 10 nanometres. They are collected and reconstructed as image with high topographic contrast. For smooth specimen surfaces shown in figure 4.2.7, they have the escape zones for both electrons uniformly deep in the specimen, resulting in minimal escape of electrons from the specimen per unit area. Rough surfaces have escape zone of

both electrons thrown off the horizontal, producing more volume of escape zone per unit area and resulting in the escape of more electrons during bombardment by the electron beam. Besides, the number of backscattered electrons is strongly depended on atomic number. The higher the atomic number the more emitted backscattered electron would be increased. It is so-called atomic number contrast of scanning electron microscope. Also the quality of reconstructed image can be improved by the noise reduction process, in which the scanning rate is slow and the number of raster line is increased. For non-conducting specimen, sharper image can be obtained by coating a thin gold layer around 10 nm, which can increase the emission of secondary and backscattered electron, reduction of thermal damages as well as the elimination of specimen charging. So, better details of surface morphology of the deposited thin films can be obtained by investigating the high resolution and high contrast SEM images.

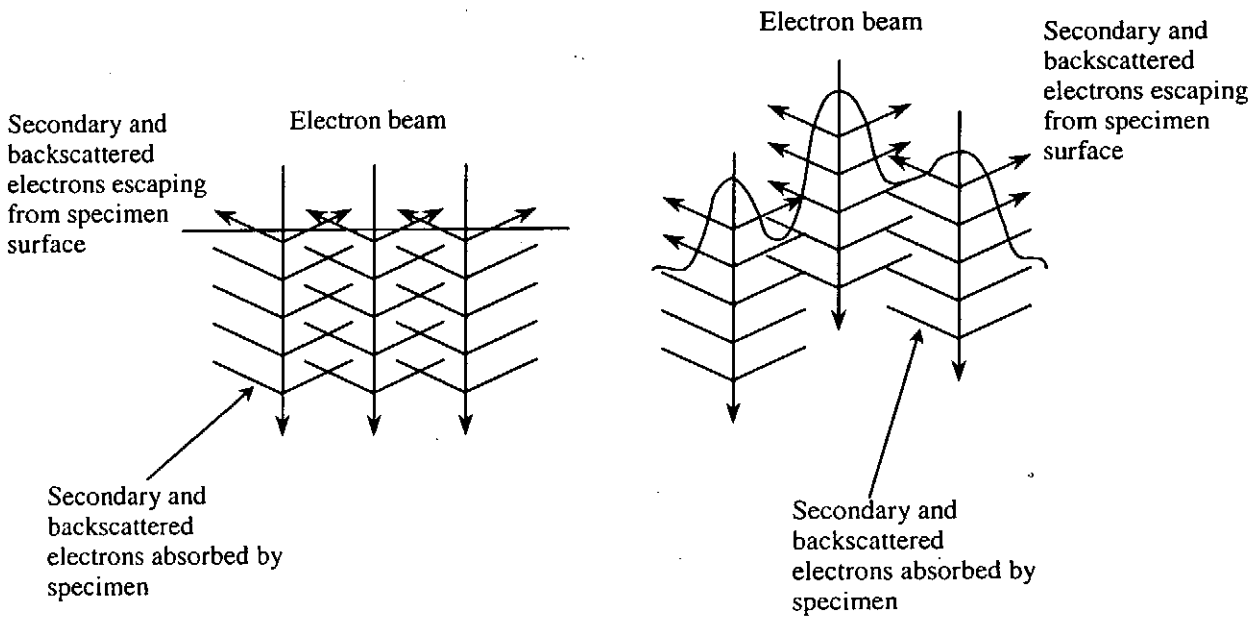

Figure 4.2.7 Topographic contrast. More backscattered and secondary electrons escape from a rough surface than from a smooth.

4.2.1.3 Atomic force microscopy (AFM)

AFM produces images that are much closer to simple topology and can image nonconducting surfaces [Binnig et al., 1983, 1986 and 1987; Martin et al., 1987]. It records interatomic forces between the apex of a tip and atoms in a sample as the tip is scanned over the surface of the sample. When the AFM is operated in a mode that senses the repulsive forces between tip and sample, the tip actually touches the sample. In the AFM machine, however, the probe tip is so sharp and the tracking force is so small that the tip can trace over individual atoms without damaging the surface of the sample. The AFM can also be operated in other mode that senses the attractive force between the tip and the sample. The feedback system then prevents the tip from touching and damaging the sample. But in this mode of operation, it generally results in decreasing lateral resolution. So far, most images obtained in this way are of micrometer-scale objects.

The probe tip can be made of a small fractured diamond fragment attached to a spring in the form of a cantilever. The small repulsive tracking force between the tip and the sample, usually in the range of 10^{-6} to 10^{-9} N, is recorded by measuring minute deflections of the cantilever. The typical spring constant for a cantilever would be about 1 N/m. If the microcantilever is made of silicon oxide with silicon etching technology [Albrecht et al., 1988] it can be even lighter and has a higher resonant frequency, less sensitivity to vibrations and more stable for atomic force microscope. Thus, a cantilever with a vibration frequency of 10 kHz would have a vibration amplitude less than 0.01 nm and would be suitable for atomic resolution imaging with minimal vibration isolation.

The essential parts of an AFM are shown in Figure 4.2.8. All AFMs use the principle of negative feedback to control the tip-sample separation. The atomic force between sample and tip is measured using a laser and detector through monitoring the cantilever motion. The measured force is compared to a user selectable reference

force to determine the error. The negative feedback loop moves the sample as needed to eliminate the measured error and maintain the desired interaction force. The sample is moved vertically (Z direction) using a piezoelectric (PZT) scanning tube position actuator. The PZT scanning tube also moves the sample in the X and Y direction for the raster scan. The sample is raster scanned under the tip while the feedback adjusts the sample position for a constant force. The sample's position in the Z-axis direction, commanded by the feedback, corresponds to the topography of the surface. To construct a 3 dimensional image of the surface, the computer records these Z-axis movements as a function of the sample's X and Y directions.

In our studies, AFM (Burleigh, Metris-2000) was used to characterize the surface morphology of the deposited films especially in the determination of lateral grain size and the surface roughness of the films.

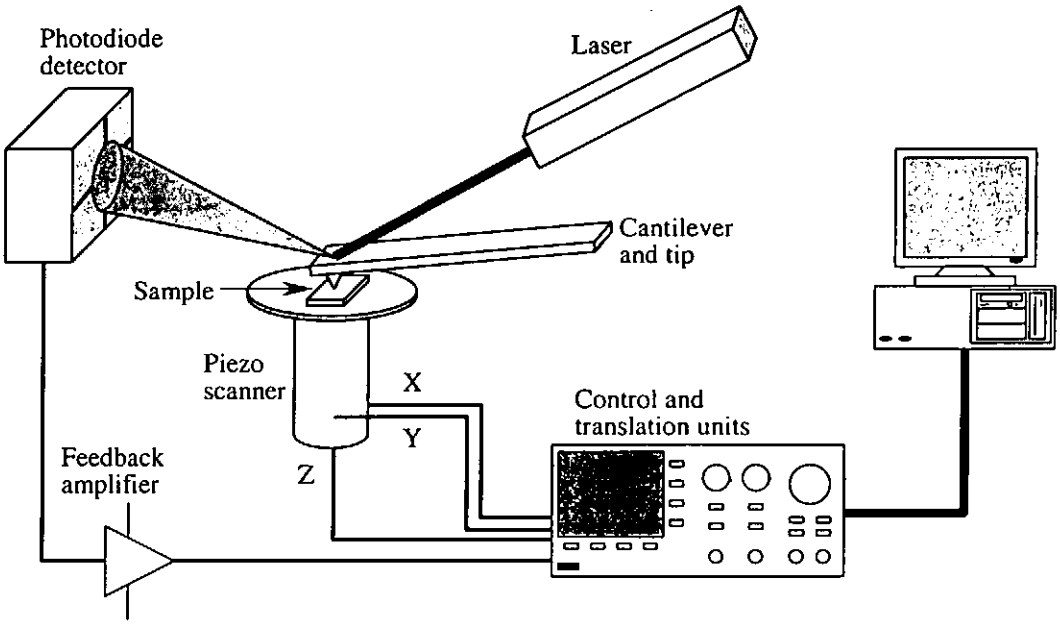

Figure 4.2.8 Schematic diagram of a typical atomic force microscopy control system.

4.2.1.4 Raman spectroscopy

Raman spectroscopy is a characterization method that measures the frequencies of the long-wavelength lattice vibrations (phonons). Unlike the x-ray diffraction, Raman spectroscopy does not provide a direct determination of the crystal structure. However, Raman spectroscopy has several advantages over diffraction methods. It can detect low-concentration impurity phases that can be missed by the XRD, and it is generally more sensitive than diffraction to noncrystalline phases. In addition, structural changes that alter the crystal symmetry often have a large effect on the Raman spectrum. So that Raman spectroscopy can distinguish more readily between crystalline phases possessing different symmetries but similar lattice parameters. In our case, the materials under test would be the $BaTiO_3$ films. It is known that the bulk $BaTiO_3$ ceramic has a very small lattice different in c/a ratio at the tetragonal phase (lattice constant a = 3.99Å, c = 4.03Å). Also the c/a ratio would be varied in thin film structure, since it would under stress due to the influence of the lattice mismatch with the LAO substrate. The variation would also effected from the different in their thermal expansion and contraction caused by the thermal history in the fabrication process. These effects would make XRD in difficulty to determine the $BaTiO_3$ films' structure. Raman spectroscopy is considered the solution in this problem.

In our measurement, a conventional Raman setup and a micro-Raman setup have been used to characterize films. For the conventional Raman setup, an argon ion CW laser (Coherent Innova 70) using 488 nm laser line was used. The output power was kept at 100 mW and focused to a spot size in the order of mm diameter. The scattered light were collected in the small-angle backward scattering geometry by a camera lens (Canon FD 85mm 1:18), and the collected scattering light was analyzed by a double grating monochromator (Spex 1403) equipped with a cooled photomultiplier tube (Hamamatsu R928).

For micro-Raman setup, the studies were performed in Materials Characterisation and Preparation Facility of The Hong Kong University of Science and Technology. The equipment used was micro-Raman spectrometer (Renishaw Ramascope 3000) equipped with a He-Ne laser ($\lambda = 632.8$ nm). The laser power of 10 mW was focused to a size of ~2 μm at the sample surface by a microscope. The room temperature room spectra were then recorded by a charge coupled device detector.

4.2.1.5 Surface profiling

The thickness of the thin films can be determined by examining the SEM image of cross-section of the film. Alternatively, film thickness measurement can be obtained more conveniently by using Alpha-step profiler (Tencor Instrument, model P-10). A sharp step on the film is needed to carry out this measurement. For this reason, a mask should be placed to produce an sharp step on the film during deposition. The idea of Alpha-step is to move a very fine needle across the step, detecting the thickness profile of the film like the following figure. The highest resolution of this instrument is less than 1 nm.

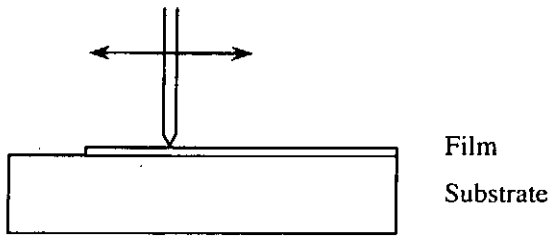

Figure 4.2.9 Film thickness measurement by Alpha-step surface profiler.

4.2.2 Optical characterization

4.2.2.1 Photoluminescence

Photoluminescence (PL) observed in II-IV compounds is a very useful tool in examining excitation transport in molecular solids, regular crystals or even disorder system. PL spectroscopy is a sensitive, non-destructive technique that can provide valuable information on the type and distribution of defects and impurities in a sample to examine its crystal quality.

In our PL measurement, ZnS:Mn films were excited by a 488 nm laser line from an argon ion gas laser (Coherent Innova 70) with power of 100 mW. PL spectra were collected by a camera lens (Canon FD 85mm 1:18) and dispersed by a double grating monochromator (Spex 1403). The dispersed signal was recorded by a photomultiplier tube (Hamamatsu R928).

4.2.3 Electrical properties measurement

4.2.3.1 Polarization-voltage measurement

Polarization-voltage (P-V) or polarization-electric field (P-E) loop measurement is a mean to determine the electrical properties of ferroelectrics. In this measurement, a Radiant Technologies RT66A standardized ferroelectric test system under virtual ground mode is used to carry out the P-V or P-E measurement. The drive and return terminals are connected to the top and bottom electrodes, respectively. While the kit drives the ferroelectric material with a triangular voltage profile, it measures the polarization of the ferroelectric material simultaneously. After one cycle of the driving voltage, a hysteresis loop of P-V or P-E is shown, from which the saturation and remnant polarizations for both positive and negative poling as well as the coercive

voltage or electric field can be determined.

4.2.3.2 *Dielectric measurement*

The degree of polarizability or charge storage capability of a material is identified by the term relative dielectric constant (ε_r). This is also referred to as relative permittivity. When an electric field is applied to two flat plates of a metal such that one plate becomes positive and the other negative, this applied electric field will cause polarization in the material between the conductive plates. The relative dielectric constant compares the polarizability or charge storage capability of the material with that of a vacuum between the plates:

$$\varepsilon_r = \frac{\varepsilon_{material}}{\varepsilon_{vacuum}} = \frac{\varepsilon^*}{\varepsilon_0}$$

Obviously, for vacuum, ε_r equals to 1. For most of the materials, ε_r will be larger than 1. The dielectric constant is affected by temperature, and the frequency of the applied field and the frequency of other electromagnetic fields impinging on the materials.

To measure the relative permittivity of our samples, we have to measure the capacitance first. The capacitance depends on the relative dielectric constant ε_r and the geometry of the capacitor. For a parallel-plate capacitor, the capacitance is expressed as:

$$C = \frac{\varepsilon_0 \varepsilon_r A}{t}$$

where A is the total area of the electrodes, t is the thickness of the dielectric. Thus the capacitance increases with the area and relative dielectric constant while it decreases when the thickness of the dielectric increases. Thin layers of Au or Pt, acted as the top electrodes of the capacitor, were coated on top of our films. The capacitance was measured by an impedance gain-phase analyzer (Hewlett Packard 4194A). Capacitance and dielectric loss at different frequency were measured.

CHAPTER 5

FABRICATION AND CHARACTERIZATION OF FILM LAYERS

In this project, heterostructures of insulating/phosphor/insulating tri-layer, which is basically the structure of electroluminescent device, was fabricated. Indeed, this study emphasizes on the use of two different insulating layers, namely, $BaTiO_3$ and $Pb(Zr_{0.52}Ti_{0.48})O_3$ (PZT), and their performance was compared. Since pulsed laser deposition (PLD) is a well-known technique to grow good quality thin films, PLD was used to fabricate the insulating layers. On the other hand, ZnS:Mn has the highest luminous efficiency which is ideal material for the phosphor layer. In our studies, the phosphor layer was also growth by PLD. To successfully fabricate the insulating/phosphor/insulating tri-layer structure, the correlation between the structural properties and processing parameters for individual layer must be first understood i.e. the technique for fabricating individual layer was investigated first. Accordingly, the fabrication and characterization of individual layers are discussed in this chapter.

5.1 Insulating layer

5.1.1 $BaTiO_3$ on $LaAlO_3$ (LAO) substrate

Either polycrystalline or amorphous $BaTiO_3$ have been used as the insulating layers for ACTFEL devices in many studies [Song et al., 1998]. The characteristics of these $BaTiO_3$ layer have been compared with other dielectric materials [Krasnov, 1999]. Promising dielectric properties with moderate dielectric constant at submicron thickness and excellent interface with ZnS:Mn made $BaTiO_3$ a excellent candidate for incorporation into ACTFEL devices. Since our goal is to compare the performance of the dielectric material with that of ferroelectric material such as PZT, good crystallinity $BaTiO_3$ films with comparable dielectric constant with PZT is fabricated

intentionally. In this part of the studies, high quality $BaTiO_3$ was fabricated on single crystal $LaAlO_3$ (LAO) substrates. The crystallinity, growth orientation, surface roughness and purity of the $BaTiO_3$ phase were investigated as a function of film thickness.

5.1.1.1 Fabrication

As it has been showed in Figure 4.1.1, the $BaTiO_3$ target was ablated by the KrF pulsed excimer laser with a repetition rate of 10 Hz. The laser beam was focused onto the surface of the target with the fluence of 6 J/cm^2. During deposition, the substrate was kept at 700 °C and under 200 mTorr ambient oxygen. The films were then post-deposition annealed at the same condition for 2 hours. The thickness of the deposited $BaTiO_3$ films was controlled by the deposition time. The films' thickness was examined by a surface profiler (KLA-Tencor P-10) across the step created during deposition.

5.1.1.2 Structural characterization

Structural characterization of these films have been made by X-ray diffraction (XRD), scanning electron microscopy (SEM), atomic force microscopy (AFM), Raman spectroscopy.

XRD operated in four-circle geometry using the Cu K_α radiation was used to studies these films. The θ–2θ XRD patterns of these films are shown in Figure 5.1.1.1. In general, the intensity of the spectra increases with film thickness. Only peaks originated from families of $BaTiO_3$ (001) and LAO (001) are detected in all the samples. No other diffraction peaks corresponding to impurity phases or randomly oriented grains were observed indicating that the $BaTiO_3$ films are single phase and oriented in a preferred direction.

The qualities of the orientation of the films, also recognized as the texture of the

films, were determined by the ω-scan of the (002) peaks of the $BaTiO_3$. Figure 5.1.1.2 plots the full-width at half-maximum (FWHM) of the ω rocking curves as a function of thickness. The figure, in general, indicates an improvement of the films' texture with increasing film thickness for thickness below 200 nm. The orientation gets better for films with thickness increased toward 200 nm. This better orientation may be attributed to the relaxation of the stress induced by lattice mismatch between the $BaTiO_3$ and the LAO substrate. (The out-of-plane lattice constant calculated from the XRD profile is about 4.001Å) For thickness above 200 nm, the films' texture deteriorates with increasing thickness and reaches a maximum FWHM of ~1.8° at about 600 nm. Afterwards, the texture of the deposited BTO films gradually improved again as the film thickness further increased.

Though the θ–2θ and ω scans measure the crystallinity and orientation of the $BaTiO_3$ films, only information of grains whose atomic planes parallel to the samples' surface is obtained. The in-plane orientations and the epitaxial properties of the films, however, cannot be acquired by the above method. So ϕ-scans was employed in order to have a complete picture of the texture of the films. Since LAO has a pseudo-cubic structure and $BaTiO_3$ has a c/a ratio slightly deviated from unity (~1.01) in the tetragonal phase, XRD operating at 45° tilted χ-angle ϕ-scan of {101} planes for $BaTiO_3$ and LAO were performed. Figure 5.1.1.3 shows the ϕ-scans of (101) peaks of $BaTiO_3$ and LAO substrates for the samples with thickness of 30 and 2500 nm. The XRD patterns show that the peaks of the films are 90° apart and coincide the same angles as that of LAO substrates, all other films with different thicknesses show a similar feature. From the ϕ-scans, $BaTiO_3$ films have a four-fold symmetry and are cube-on-cube grown on top of the LAO substrate. This feature reveals the epitaxial growth of the $BaTiO_3$ films on LAO substrates.

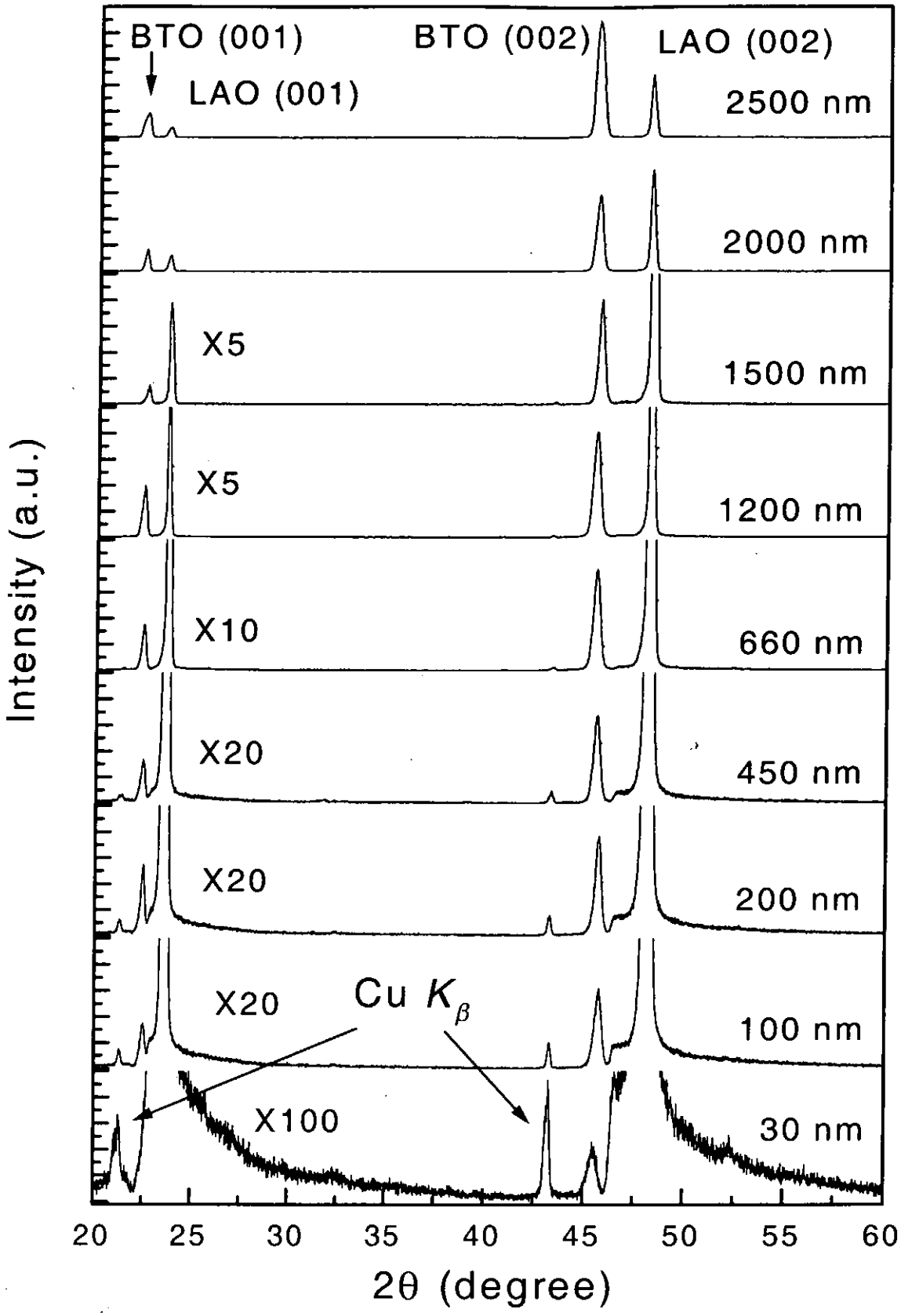

Figure 5.1.1.1 XRD θ–2θ patterns of $BaTiO_3$ films on LAO substrates with different thickness. The signals of thinner films are multiplied with a factor indicated in the graph for better comparison.

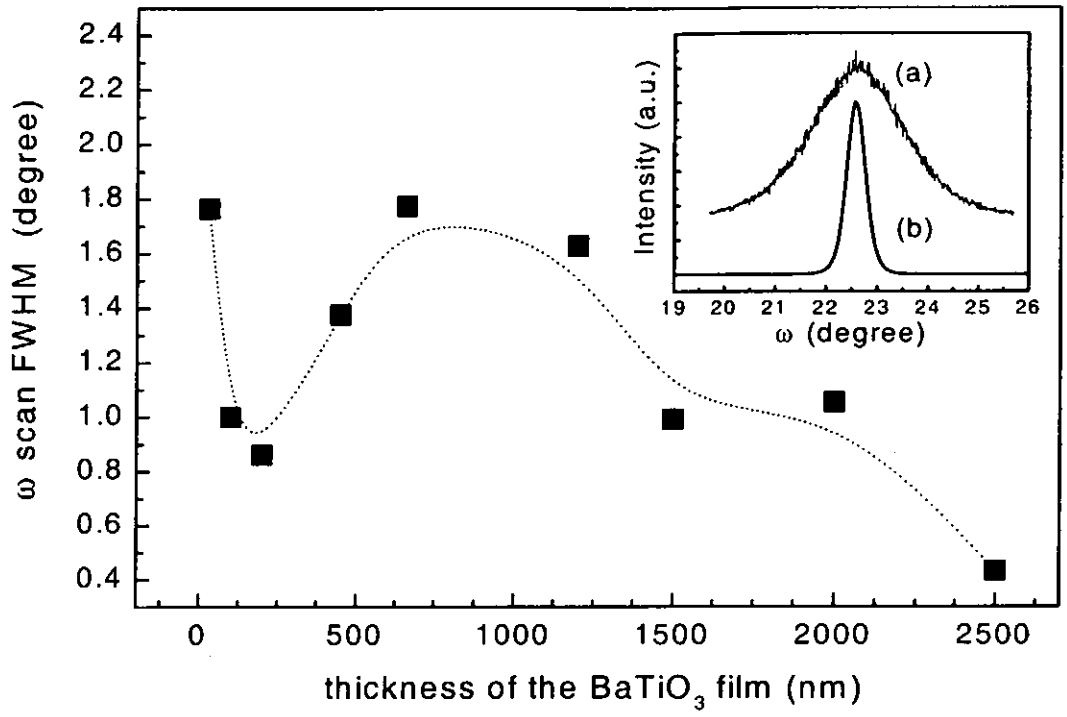

Figure 5.1.1.2 FWHM of ω rocking curve of $BaTiO_3$ (002) peaks with different film's thickness. Inset is the ω rocking curve profiles of (a) 30 nm and (b) 2500 nm with FWHM of 1.76° and 0.43° respectively.

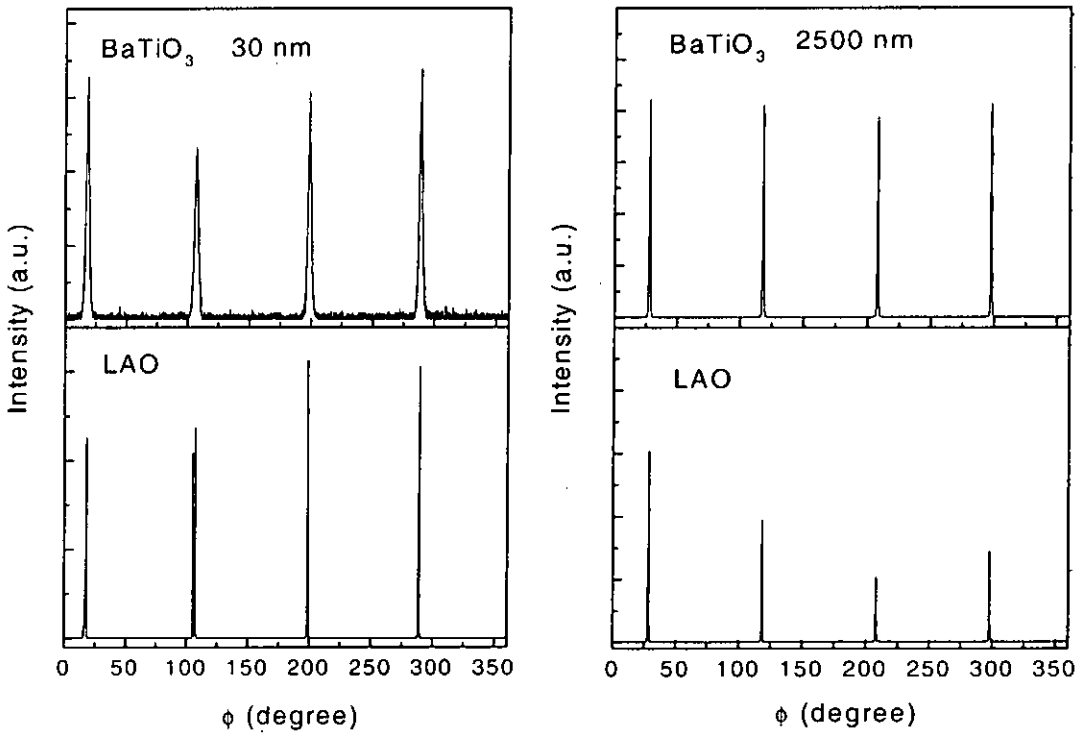

Figure 5.1.1.3 The ϕ scan of the (101) peaks of $BaTiO_3$ and LAO for the films of 30 nm and 2500 nm thick.

The thickness dependent surface morphology, roughness and grain size of the films were characterized by atomic force microscopy (AFM). A smooth continuous layer is observed, as shown in figure 5.1.1.4 (a), in the film of 30 nm thick. The film surface consists of grains with a fairly uniform crystallite size of approximately 60 nm. The root-mean square surface roughness R_q of this layer is only 1.6 nm. As film thickness increased, further grain growth continues with crystallites of slightly larger size nucleating on top of one another. At about 200 nm thick, the film comprises uniform rounded crystallites of size approximately 100 nm, shown in figure 5.1.1.4 (c). At the same time, the surface roughness increases to 3.2 nm. Further increase of film thickness is accompanied by grain coarsening laterally. At this stage, the shape of the crystallites remains rounded, but the distribution of grain sizes becomes more spread and resulting in a rougher surface. As film thickness reaches 1500 nm as shown in figure 5.1.1.4 (g), the anisotropy increases as a consequence of the shadowing effect, which is commonly observed in PLD method. In this case, substantial grain elongation can be seen clearly. The lateral length and the roughness of the grains can reach as much as 300 nm and 10 nm, respectively. General speaking, surface roughness of all the films is less than 1% of the deposited thickness and is therefore quite low. Figure 5.1.1.5 shows the relationship of surface roughness and grain size with the film thickness.

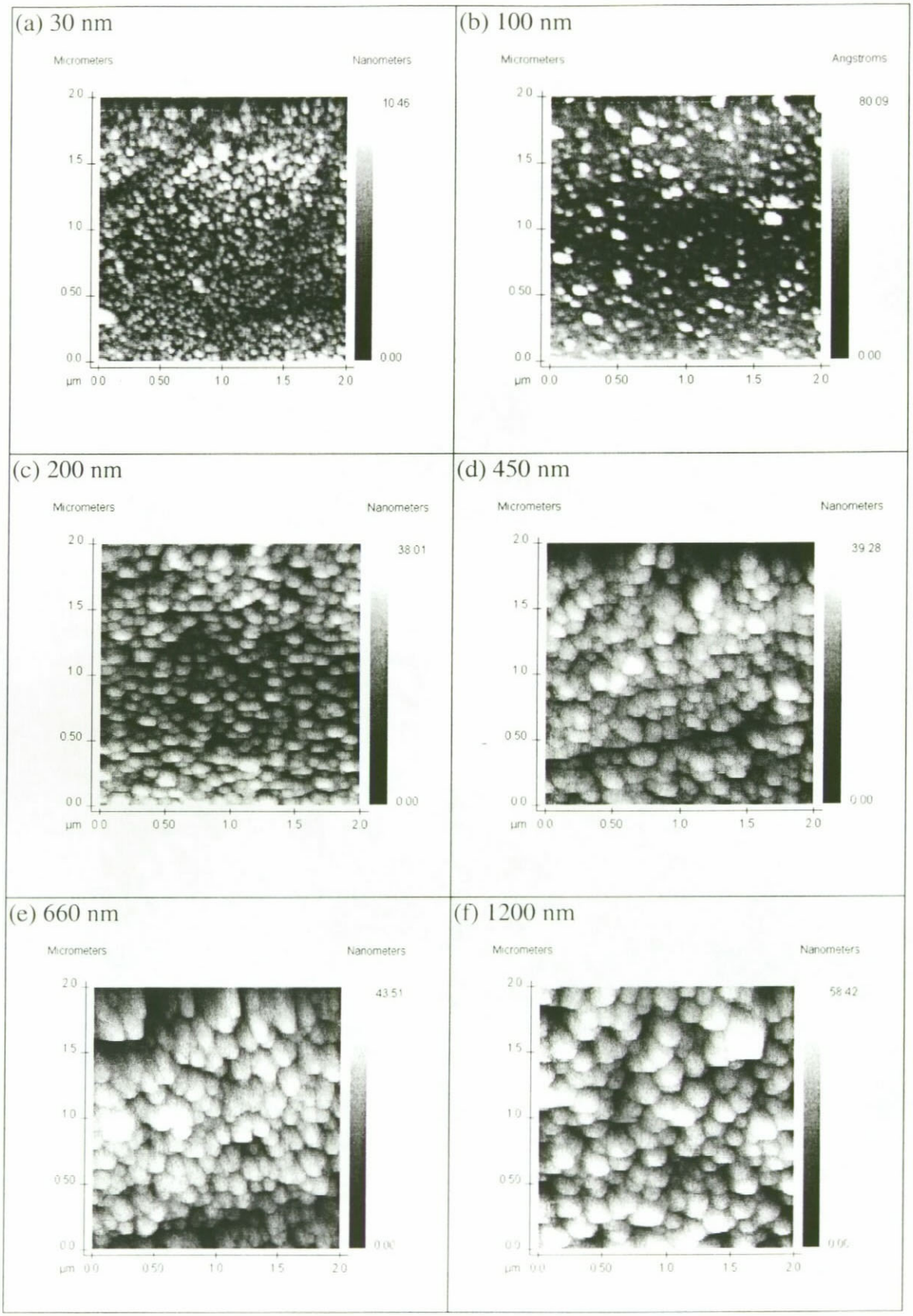

Figure 5.1.1.4 (Continue) AFM images of the $BaTiO_3$ films on LAO with different thickness.

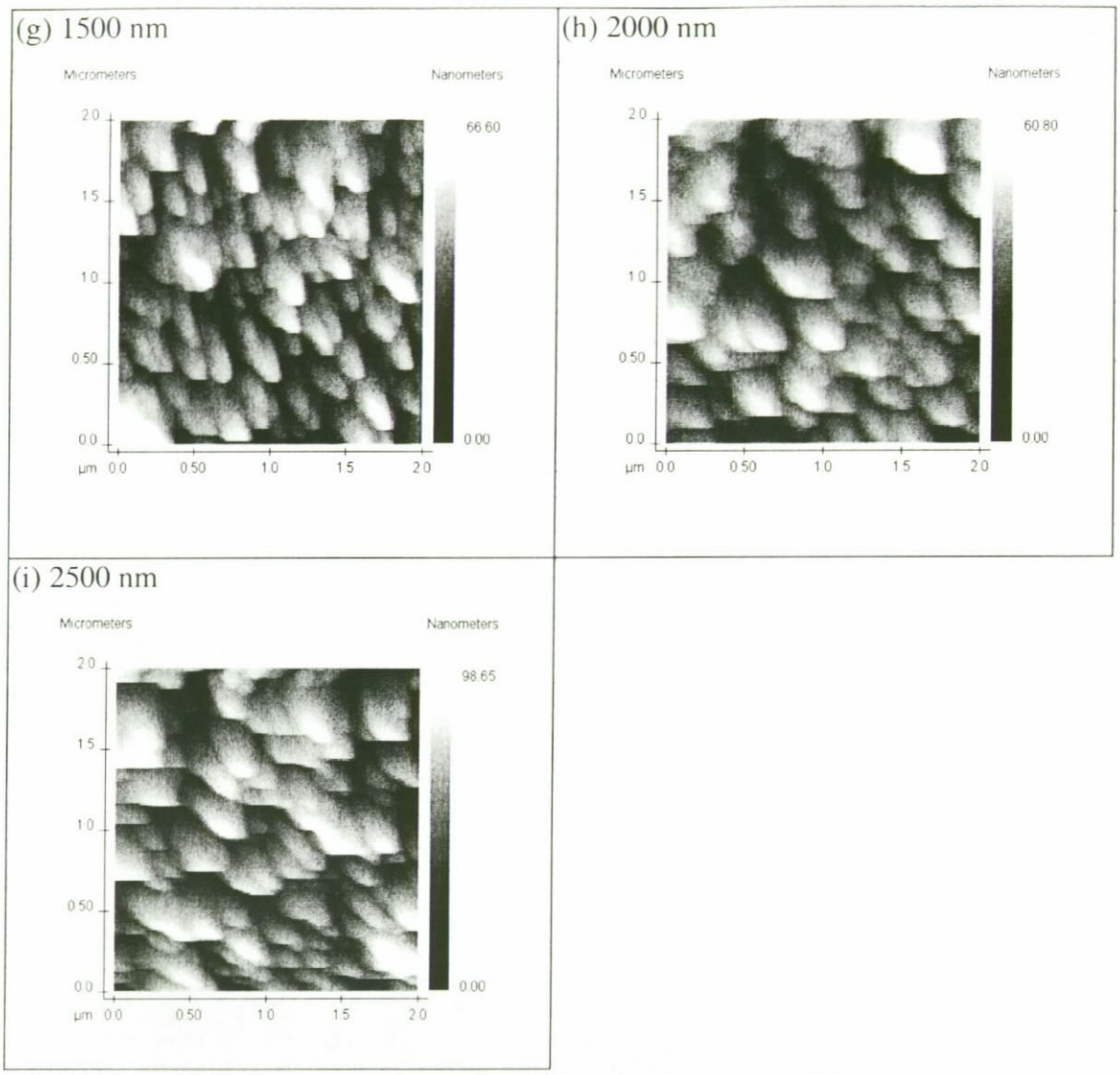

Figure 5.1.1.4 (Continue) AFM images of the $BaTiO_3$ films on LAO with different thickness.

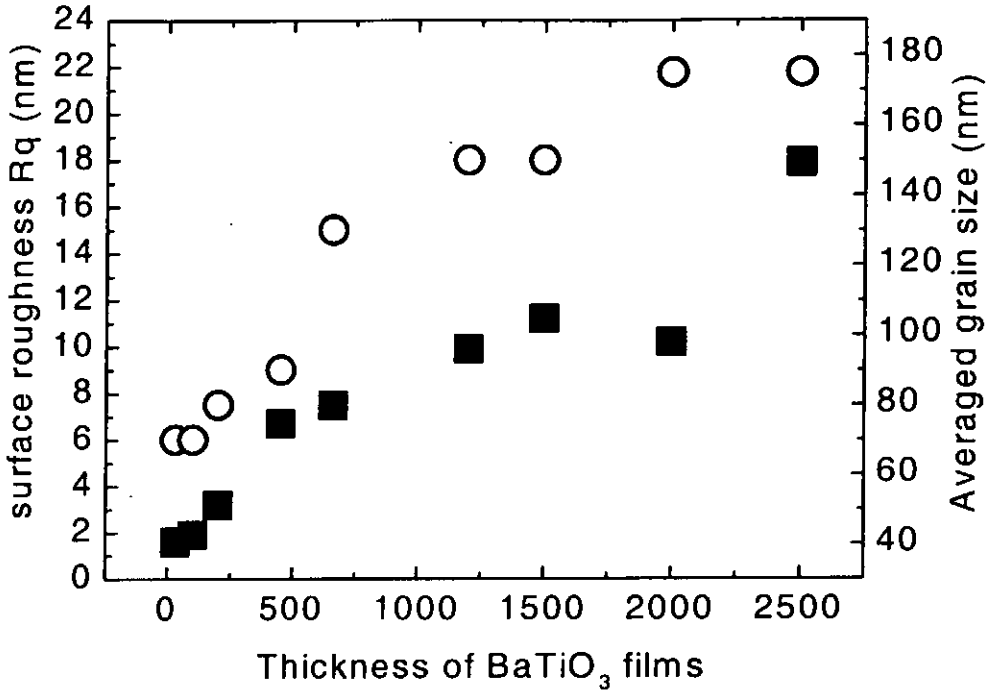

Figure 5.1.1.5 Plots of surface roughness and average grain size as a function of film thickness. (■: surface roughness, ○: average grain size)

The structural properties of $BaTiO_3$ films were also investigated by micro-Raman spectroscopy, which has several advantages over XRD methods [Robins et al., 1994]. For $BaTiO_3$, the small deviation from unity of the c/a ratio (≈1.01) in the tetragonal phase makes identification of this phase by XRD difficult. Furthermore, strain and disorder in thin films generally broaden the XRD peaks and this adds to the difficulty of using XRD to distinguish between tetragonal and cubic phases. However, the 305 cm^{-1} and 720 cm^{-1} Raman peaks are unambiguous confirmation of the presence of the tetragonal phase of $BaTiO_3$ [Robins et al., 1994].

Single crystal $BaTiO_3$ has a cubic perovskite-type structure above its Curie temperature (T_C =132°C) and is distorted to a tetragonal lattice below T_C. There are 12 Raman active modes: $3A_1+4E+B_1$ [Cui et al., 1996]. Here, A_1 is a nondegenerate mode, E is the double degenerate mode, and B_1 is the silent mode. Due to the long-range electrostatic forces, each of these modes splits into a transverse and longitudinal optical (TO and LO) mode. Raman spectra of the $BaTiO_3$ films are shown in figure 5.1.1.6. As expected, the intensity of the Raman spectra increases naturally with film thickness. The strong phonon mode at 486 cm^{-1} attributed from the LAO substrates is observed. The intensity of this mode, as expected, becomes weaker as the film thickness increased. Four phonon modes arisen from $BaTiO_3$ films are identified in our measurement. A weak peak is located at 285 cm^{-1} corresponding to a A_1(TO) phonon mode. The narrow peak at 305 cm^{-1} is assigned as the E(TO) mode. Another broad band at 520 cm^{-1} attributed to a A_1(TO) phonon mode of the tetragonal or cubic phase of $BaTiO_3$ is also observed. Finally, the highest frequency peak at 720 cm^{-1} is observed, in which both A_1(TO) and E(LO) character seem to be present. As discussed by L.H. Robin *et al*, the narrow peaks at 305 cm^{-1} and 720 cm^{-1} are usually used to indicate the tetragonal phase present in the $BaTiO_3$ films. Therefore, our Raman results indicate the presence of the tetragonal phase in all $BaTiO_3$ films of different thickness which cannot be confirmed in our X-ray measurement. Thus, the higher sensitivity to tetragonal phase of $BaTiO_3$ makes Raman spectroscopy better for qualifying our films than using XRD alone. Furthermore, no observation of phonon

mode at ~ 850-900 cm^{-1}, 1059 cm^{-1} and 1085 cm^{-1}, which are attributed to an amorphous Ba-Ti-O phase, orthorhombic Ba_2TiO_4 impurity phase and Ti-rich crystalline phase, respectively, indicates that the samples contain neither amorphous material nor Ti-rich impurity [Robins et al., 1994]. Since Raman scattering is very sensitive to impurity phase presence in the films, the purely $BaTiO_3$ phase obtained from these PLD method indicates our films are good in stoichiometry and free of impurity.

It is well known that the width of the Raman peaks associated with a given crystalline phase tends to decrease with increasing crystalline quality (i.e. lower defect density and less residual stress). Since the phonon modes at 305 cm^{-1} and 720 cm^{-1} are good indicators in the Raman spectrum of good-crystalline-quality tetragonal $BaTiO_3$, we analyzed the line width of both the 305 cm^{-1} and 720 cm^{-1} as well as the 520 cm^{-1} Raman peaks. Figure 5.1.1.7 shows the variation of the full-width at half-maximum (FWHM) of these peaks as a function of films thickness. A nonlinear least square fitting routine was used to fit the spectra with the Lorentzian type phonon modes plus a linear background. From each fitting, three parameters (band wave number, band intensity and FWHM) for each peak were obtained such that the FWHM versus film thickness was acquired. In the fitting routine, the three parameters were taken simultaneously as unconstrained variables. However, as the Raman spectra from the films of thickness less than 400 nm were very weak, the fitted FWHM values of these films are not shown in figure 5.1.1.8. Similar to the XRD ω rocking curve (figure 5.1.1.2), a maximum in FWHM is observed at films thickness of about 1 μm. For films with thickness larger than 1 μm, the FWHM of the phonon peaks are decreased. These results further prove that our films crystallinity is improving as the films thickness increased.

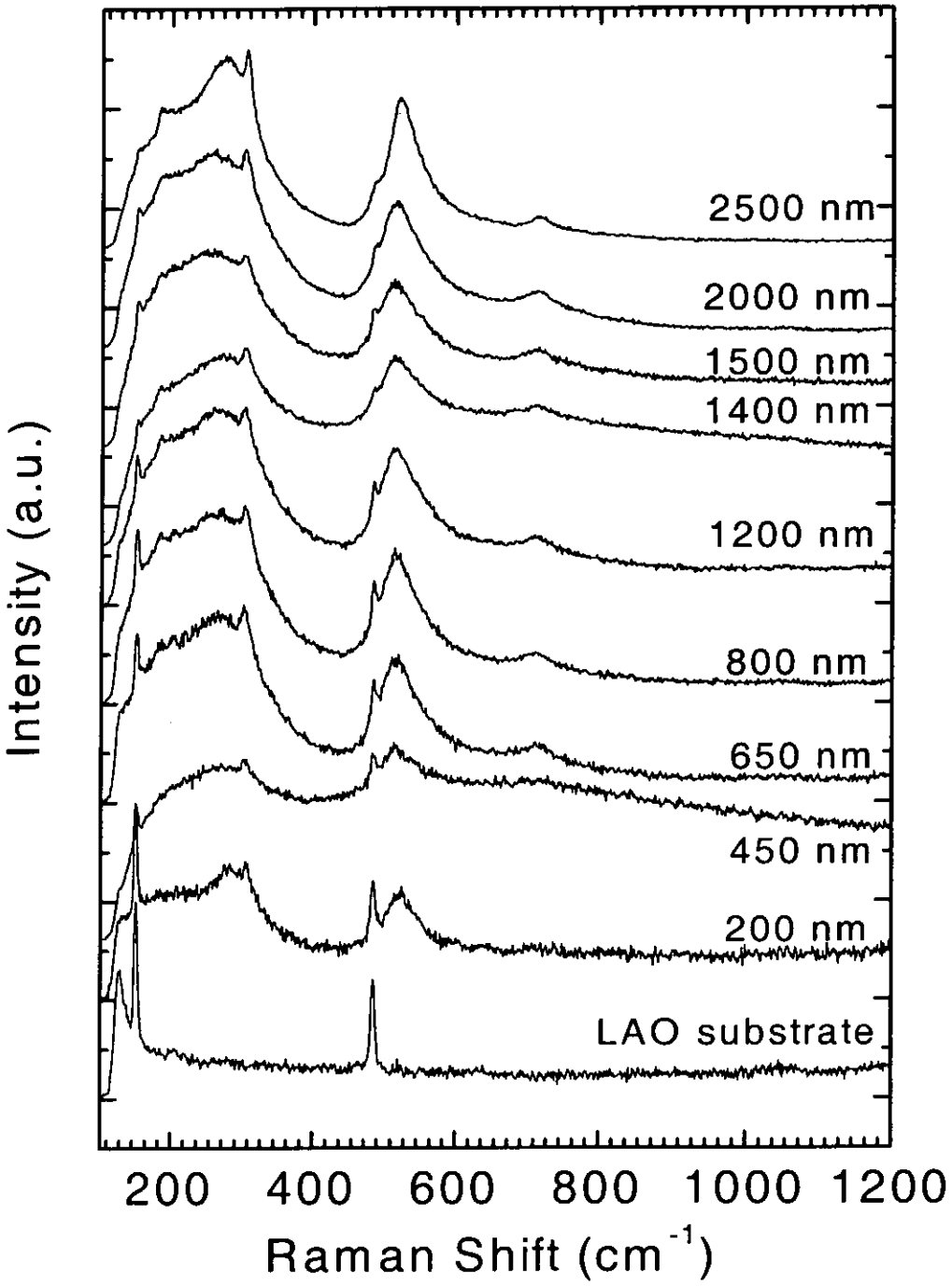

Figure 5.1.1.6 Raman spectra of $BaTiO_3$ films on LAO substrate with different thickness. The Raman spectrum of LAO substrate is shown for comparison.

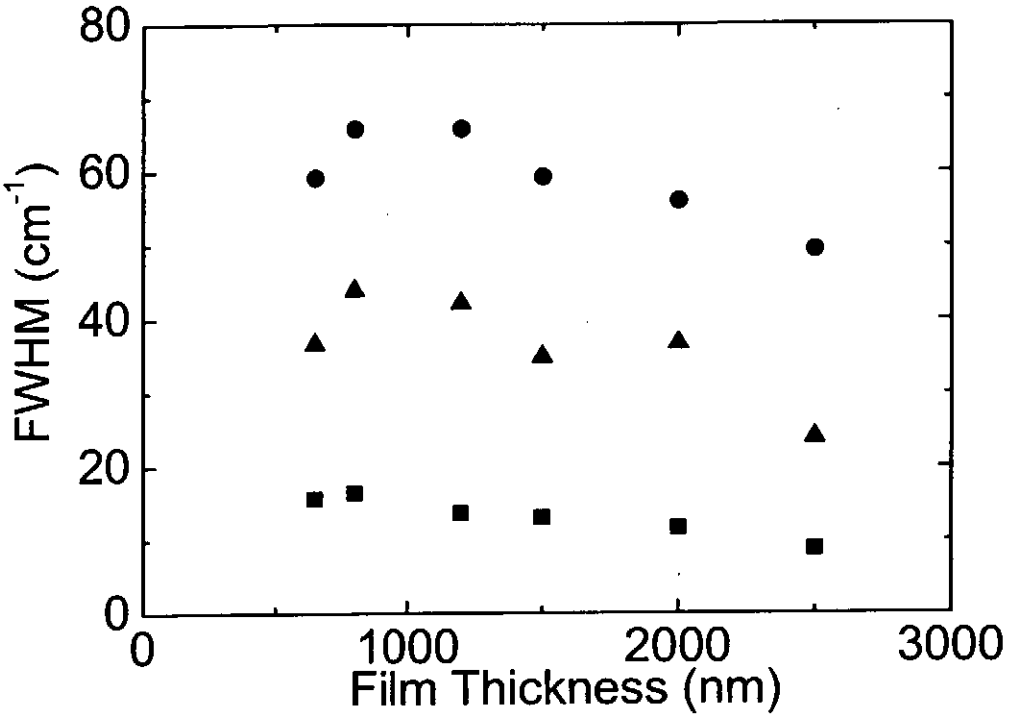

Figure 5.1.1.7 Full-width half-maximum of Raman peaks (●: 520 cm^{-1}, ▲: 720 cm^{-1}, ■: 305 cm^{-1}) as a function of film thickness.

5.1.1.3 Summary

In general, $BaTiO_3$ films were epitaxially grown on LAO substrates. Systematic variation of films' texture and crystallinity is observed with the evolution of films' thickness. Surface roughness and grain size are found to be increased with film thickness. The structural characterization studies are useful in understanding the growth mechanism of $BaTiO_3$ on LAO substrates, and hence is a useful information for growing the insulating layer for the proposed tri-layer structure.

5.1.2 $BaTiO_3/La_{0.35}Nd_{0.35}Sr_{0.3}MnO_3$ (LNSMO)/LAO

In order to characterize the electrical properties of the $BaTiO_3$ layers, suitable bottom electrodes were fabricated underneath the $BaTiO_3$ films. In our experience, conducting oxide electrode is a suitable choice for this purpose and many conducting oxide materials have been grown epitaxially on LAO substrates by PLD. By maintaining a high structural quality and good crystallinity, conducting oxide electrodes with good conductivity can be easily obtained. Among different conducting oxide electrodes, $La_{0.35}Nd_{0.35}Sr_{0.3}MnO_3$ (LNSMO) has been well studied in our group [Wu et al., 2000a]. Due to small lattice mismatch (the lattice constant of LAO is 3.79 Å, while the lattice constant of LNSMO is 3.88 Å), LNSMO has been successfully grown on LAO substrates with cube-on-cube epitaxial feature. Low room temperature resistivity of ~ 10^{-5} Ωm has been obtained in LNSMO, using appropriate deposition conditions [Wu et al., 2000a; 2001]. Besides, the electrical properties of LNSMO are only depended on the deposition parameters and are not affected by post-deposition treatment, such as, post-deposition annealing in various ambient oxygen pressure [Wu et al., 2000a; 2000b; 2001]. These superior characteristics of LNSMO make it a suitable platform for growing $BaTiO_3$ films.

5.1.2.1 Fabrication

$BaTiO_3$/LNSMO heterostructures were grown on LAO (001) substrates by in situ pulsed laser deposition using a KrF 248 nm eximer laser with a repetition rate of 10 Hz. The laser energy densities irradiated on the rotating LNSMO and $BaTiO_3$ targets were 6 and 3 J/cm^2, respectively. The target-substrate distance was 45 mm. The chamber was evacuated to a base pressure of 5 X 10^{-7} Torr by a cryopump. The heterostructures were first grown with a LNSMO layer using a deposition temperature of 650°C. The oxygen pressure during deposition was kept at 200 mTorr. The

$BaTiO_3$ films were then deposited on top of LNSMO layer at 650 °C in an oxygen ambient of 200 mTorr. The as-grown heterostructure was cooled under 1 atm. of oxygen. The thicknesses of LNSMO and $BaTiO_3$ films were measured to be about 370 and 500 nm, respectively.

5.1.2.2 Structure characterization

The crystal structure of the prepared $BaTiO_3$/LNSMO/LAO heterostructures was characterized using a four-circle X-ray diffractometer with Cu K_α radiation running in both Bragg-Brentano and four-circle geometries. The XRD θ–2θ scan pattern is shown in figure 6.1.2.1. The profile reveals both $BaTiO_3$ and LNSMO are grown single-phase oriented with good crystallinity on the LAO substrate, as only the strong {001} family peaks of the lattice planes corresponded to the deposited films are observed. The narrow ω-scan rocking curves (figure 5.1.2.2) of (002) planes of $BaTiO_3$ and LNSMO give further evidence of the quality of the films. The full width at half maximum (FWHM) of the (002) peaks for $BaTiO_3$ and LNSMO are 0.9913° and 1.0649°, respectively. These values are narrow, comparing with the FWHM of LAO substrate (~ 0.27°). This implies that the $BaTiO_3$ and LNSMO have a highly (001) preferred orientation. However, as it has been discussed in chapter 3, the θ–2θ scan and ω-scan cannot give enough information on the structural behavior especially the in-plane quality. The X-ray 360° ϕ-scans of the {101} planes of the films and substrate are required to examine the films' qualities such as the cube-on-cube growth epitaxy feature. So by assuming pseudo-cube structure of films and substrate, a 45° tilted χ-angle with 360° ϕ-scan of {202} planes were performed. Figure 5.1.2.3 shows the X-ray 360° ϕ-scans of $BaTiO_3$(202), LNSMO(202) and LAO(202) reflections. The peaks are 90° apart and appear at the same angles for both the films and substrate, which reveal the four-fold symmetry of the deposited films. The results indicate that these films are cube-on-cube epitaxially grown on top of LAO substrate.

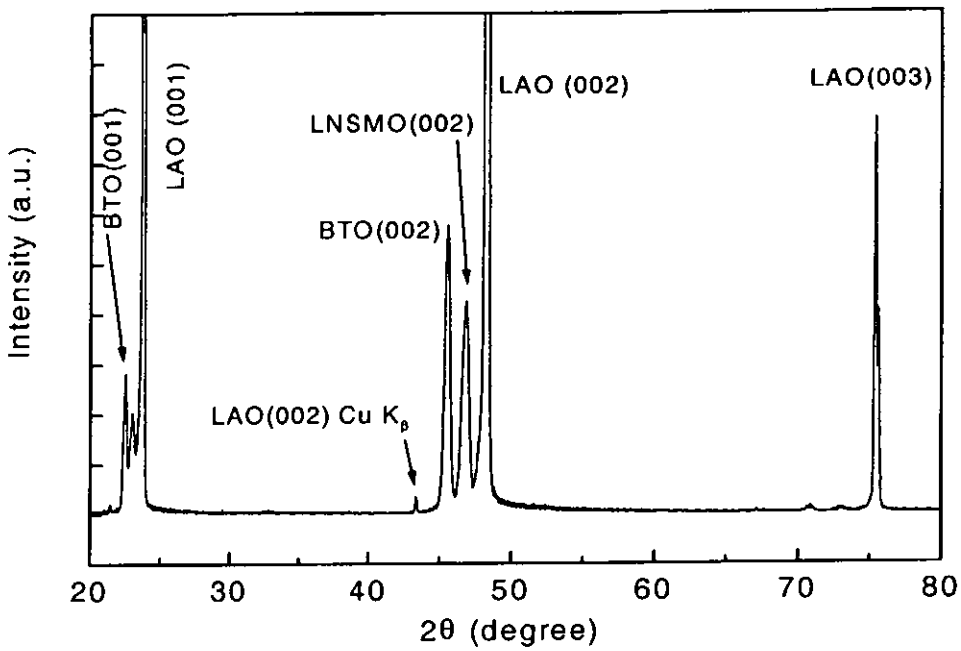

Figure 5.1.2.1 XRD θ–2θ pattern of BTO/LNSMO heterostructures growth on LAO(001) substrate

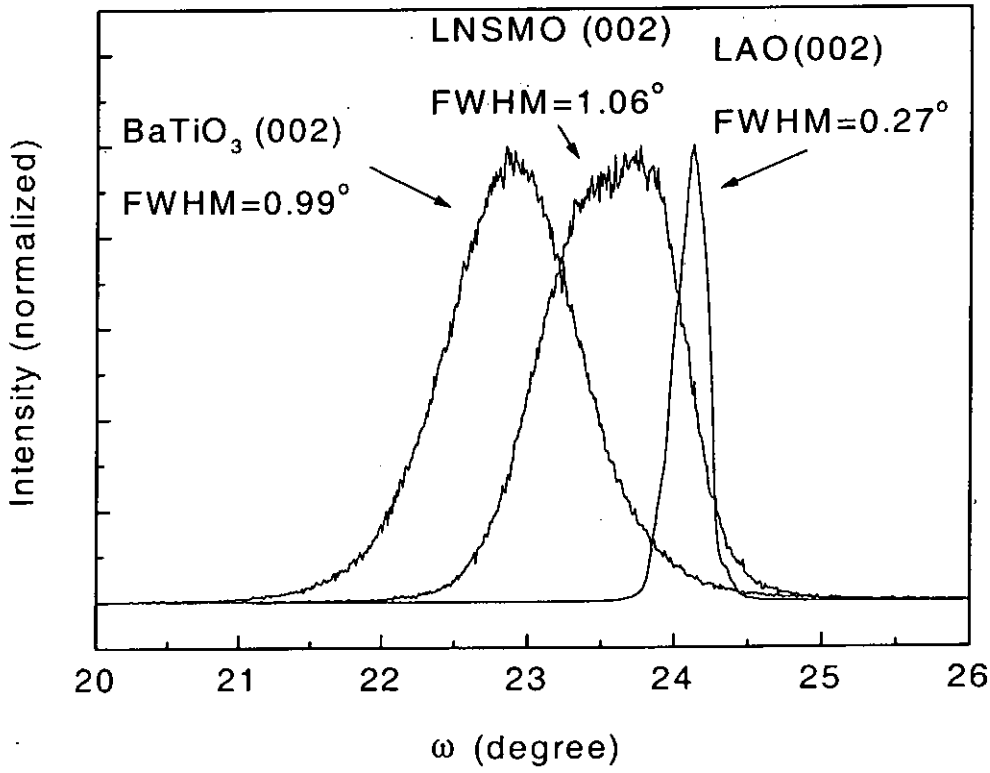

Figure 5.1.2.2 XRD ω-scan rocking curves of $BaTiO_3$, LNSMO and LAO substrate.

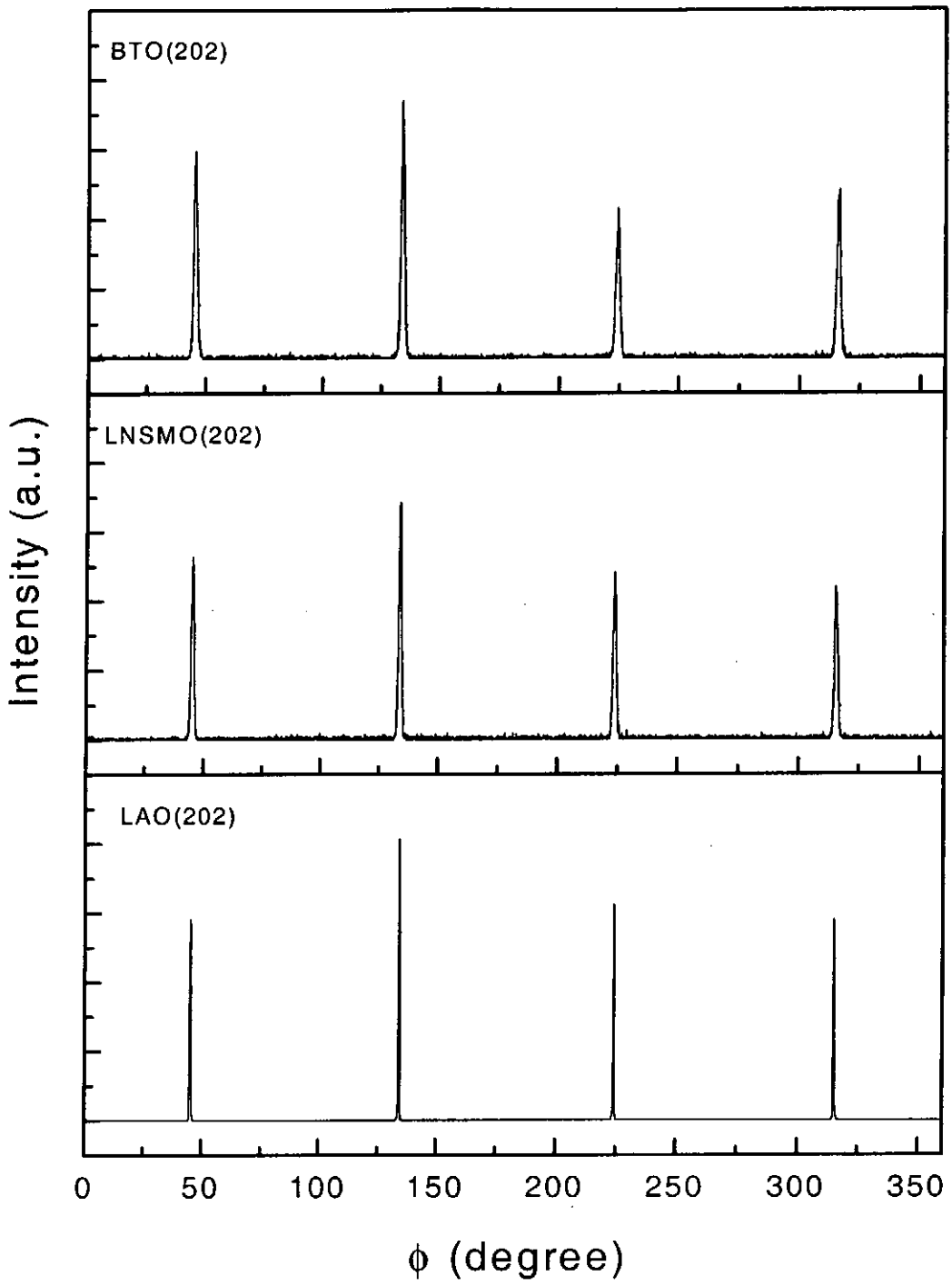

Figure 5.1.2.3 The ϕ-scans of the BTO(202), LNSMO(202) and LAO(202) of BTO/LNSMO/LAO heterostructure.

Scanning electron microscopy (SEM) was used to observe the surface morphology and the cross section of the $BaTiO_3$/LNSMO/LAO heterostructures. From figure 5.1.2.4 (a), smooth $BaTiO_3$ film with grain size ranging around 20 to 50 nm is observed. The cross-section image (figure 5.1.2.4 (b)) shows that the thicknesses of $BaTiO_3$ and LNSMO are 500 nm and 370 nm respectively. From the SEM images, it is observed that the grain size of the $BaTiO_3$ layer is smaller than those grown on LAO substrate with comparable thickness described in the section 5.1.1. Since the growth conditions were quite different, the effect of buffering LNSMO conducting layer cannot be justified. However, it is generally believed that lower deposition temperature and lack of long time post-deposition annealing result in a smaller grain size. Cross-section image indicates that the LNSMO layer has a wider lateral grain with columnar structure that provides a smooth and good crystalline platform for the growth of $BaTiO_3$ film. On top of this LNSMO layer, $BaTiO_3$ film grows with small granular crystallites near the interface and then gradually develops an oriented columnar feature that extended to the surface.

Both XRD results and SEM images suggest that the $BaTiO_3$ films are successfully fabricated on LNSMO/LAO heterostructures. The $BaTiO_3$ films are epitaxially grown in <001> orientation normal to the surface. Also the lateral grain size is small and uniform distributed at the film's surface.

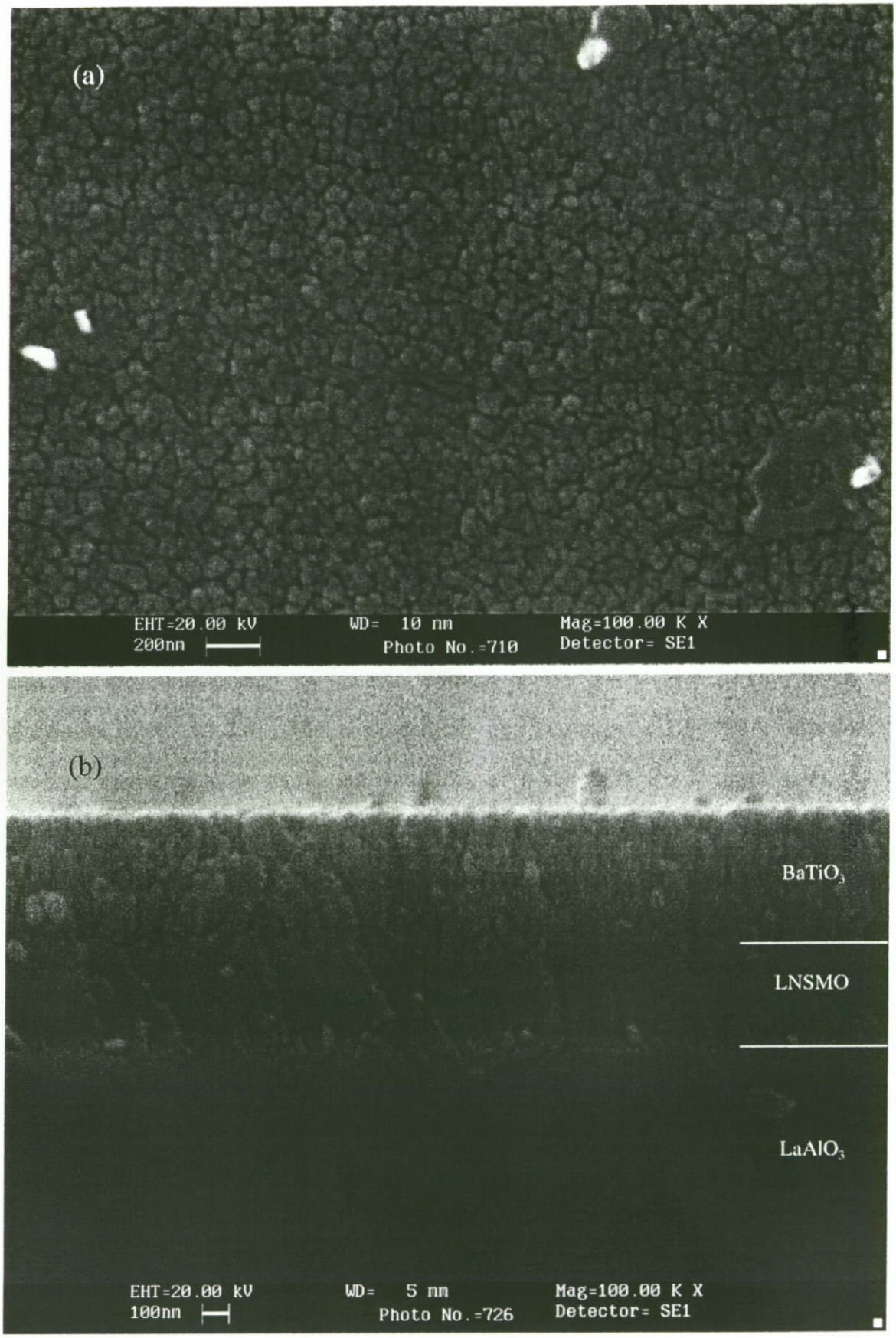

Figure 5.1.2.4 SEM's surface morphology (a) and cross section (b) images of $BaTiO_3$/LNSMO/LAO heterostructures.

5.1.2.3 Electrical measurement

Polarization-voltage (*P-E*) measurement was measured for the $BaTiO_3$/LNSMO/LAO heterostructures at room temperature using a driving frequency of 1 kHz. Pt dots of 200 μm in diameter were coated on top of the $BaTiO_3$ layer. Figure 5.1.2.5 is the results of the *P-E* loop measurement. From the graph, the $BaTiO_3$ layer possesses a very slim hysteresis loop corresponding to a nonlinear profile of polarization with the applied voltage. The coercive field and the remnant polarization are very small with applied voltages up to 5 V. The result further suggests that the $BaTiO_3$ film is tetragonal, since only the tetragonal phase $BaTiO_3$ possesses ferroelectric properties.

Further examination of the ferroelectric behavior of $BaTiO_3$ films was done by studying the ε-dependency of the bias voltage applied across the $BaTiO_3$ layer, as shown in figure 5.1.2.6. The measurement was taken by a HP4194A impedance analyzer operating at an oscillating frequency of 1 kHz with 0.5 V amplitude. The nonlinear dielectric permittivity as a function of the bias voltage was obtained. The bell-shaped behavior of *C-V* characteristics is understandable qualitatively in terms of the underlying domain switching process [Sharma et al., 1998]. Damjanovic attributed this phenomenon to the contribution of the domain wall movement [Damjanovic, 1998]. The initial rise in the permittivity with DC field is probably due to the increasing movement of domain walls that become 'free' from defects. At zero-DC field, these domain walls are locked by defects. Due to partial switching of some domains whose coercive field happens to be small enough, the permittivity can be switched by the combined DC + AC field. The maximum in the ε-*E* curve appears in the vicinity of the coercive field for the *P-E* hysteresis when most of the domains switch and the material appears to be dielectrically 'soft'. At high DC fields, the decrease in permittivity reflects two processes: (i) decrease in the number of domains as they become aligned with the field (ideally the sample becomes a single domain and

only lattice contribution is present) and (ii) inhibition of the movement of residual domain walls by the DC field. However, small oscillations or bending of residual domain walls under the AC field can still occur even at very large DC field that contributes to a smaller dielectric permittivity. Also, the $\varepsilon(V)$ obtained is relatively asymmetric at V = 0 and depends upon the direction of the change in the applied field. Such hysteresis has been suggested as an indication of ferroelectricity in $BaTiO_3$ by Boilkov [Boilkov et al., 2001]. However, the change of capacitance hysteresis loop with direction of bias voltage is explained by: (i) domain switching in the ferroelectric film [Damjanovic, 1998], and (ii) the filling of space charge at the interface between film and electrodes [Li et al., 1998; Meng et al., 2001]. From figure 5.1.2.6, the width between the two maximum points of the curves is 10 kV/cm and this value is approximately twice of the coercive field value obtained from figure 5.1.2.5. Since the coercive field value obtained is very small, it is difficult to determine the contribution of the hysteresis either from ferroelectricity or interfacial space charge. As it is reported by Sharma [Sharma et al., 1998] that amorphous $BaTiO_3$ films, which do not possess ferroelectricity, show DC bias independent *C-V* characteristic, we believe that the $BaTiO_3$ films grown on LNSMO/LAO substrates are tetragonal in structure and possess ferroelectricity. From figure 5.1.2.6, it is found that the maximum relative dielectric permittivity reachs 1250 at around 5 kV/cm and the relative dielectric permittivity is suppressed to around 400 at 100 kV/cm. Thus, the reduction of the relative dielectric permittivity is about 68%.

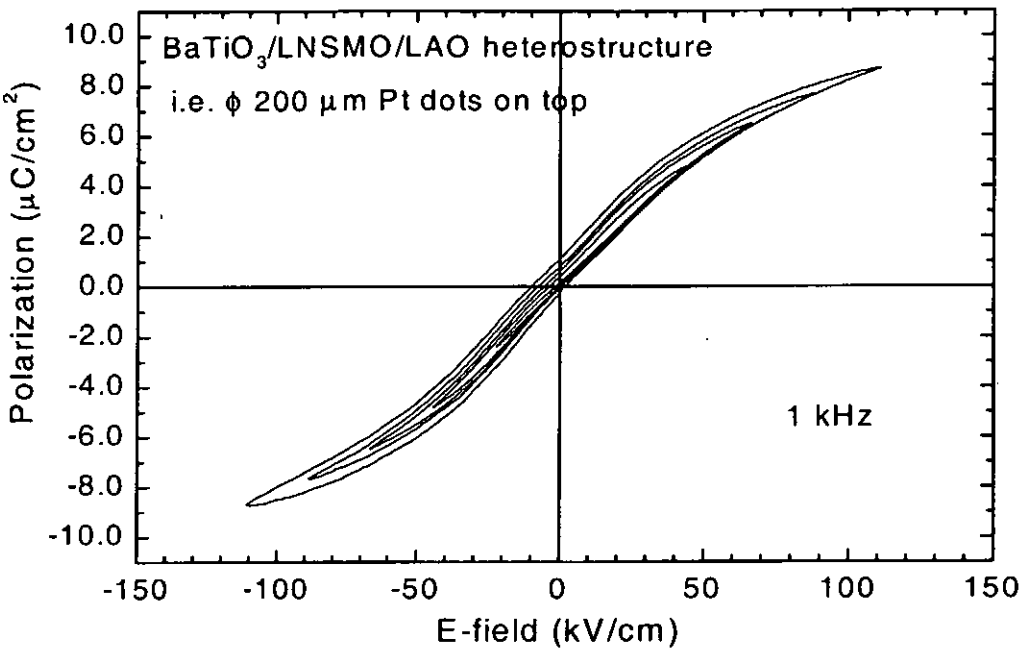

Figure 5.1.2.5 *P-E* measurement of $BaTiO_3$/LNSMO/LAO heterostructures with applied voltages of 1, 2, 3, 4 and 5 V

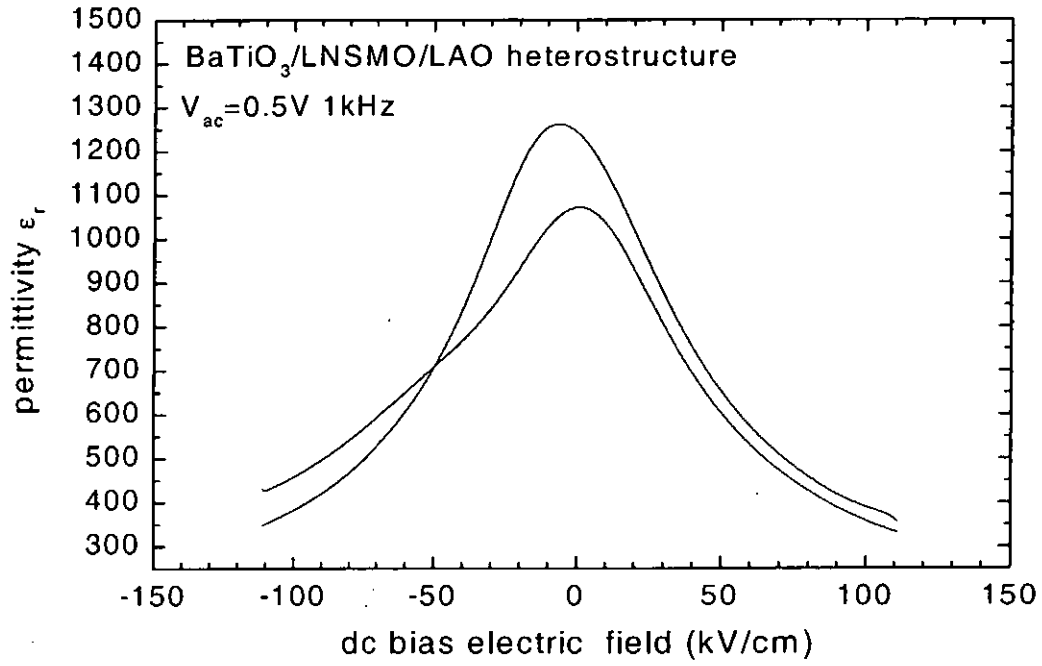

Figure 5.1.2.6 Relative dielectric permittivity of $BaTiO_3$ films on LNSMO/LAO as a function of DC electric field bias.

Figure 5.1.2.7 plots the derivative of *P-E* hysteresis loop ($\varepsilon = \partial P/\partial E$) as a function of AC field. Physically, the curve is not identical to the permittivity-DC field curve shown in figure 5.1.2.6. The *P-E* hysteresis loop is obtained by apply a strong AC field with frequency of ~ 1 kHz and its derivative, the differential permittivity, is plotted as a function of the instantaneous value of AC field with amplitude larger than the coercive field. From this curve, it is clearly noticed that the distinguishable peaks for hysteresis loop are not significant. However, reduce in the differential permittivity value when further increase in ac electric field suggests that the material undergoing the domain reorientation process. A typical frequency dependent of dielectric constant and loss tangent of the $BaTiO_3$ film are shown in figure 5.1.2.8. The dielectric constant and loss tangent of the $BaTiO_3$ film are about 1210 and 0.037 respectively at 1 kHz.

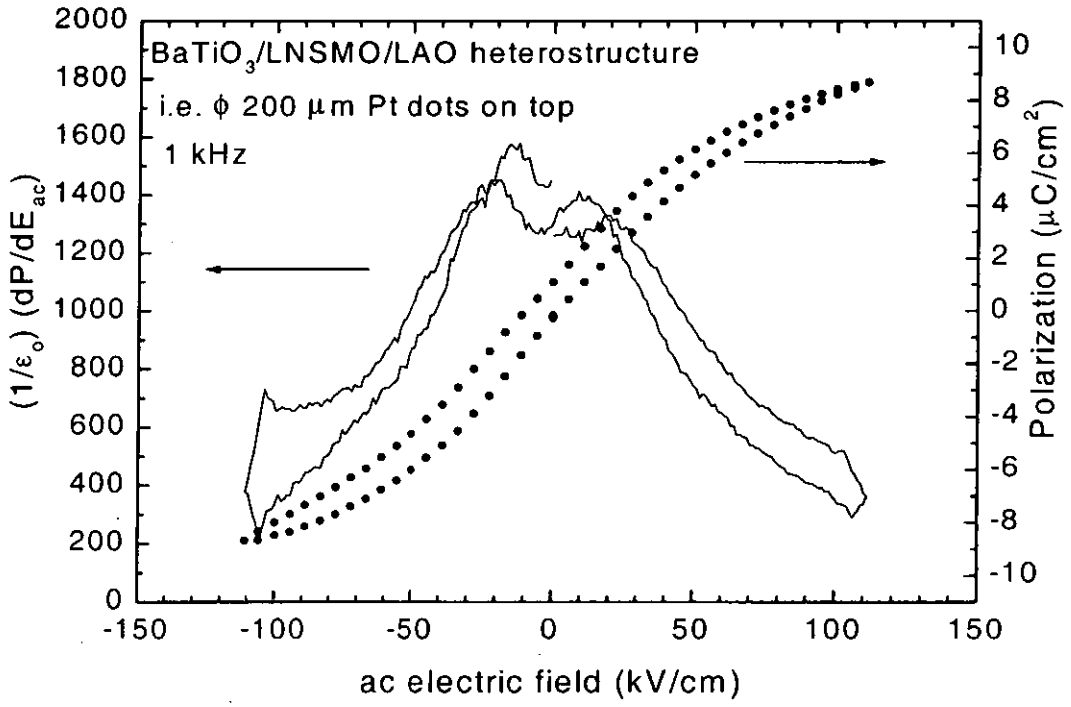

Figure 5.1.2.7 deviative d*P*/d*E* as a function of an AC electric field of the $BaTiO_3$ film on LNSMO/LAO and the correspinding *P-E* hysteresis loop.

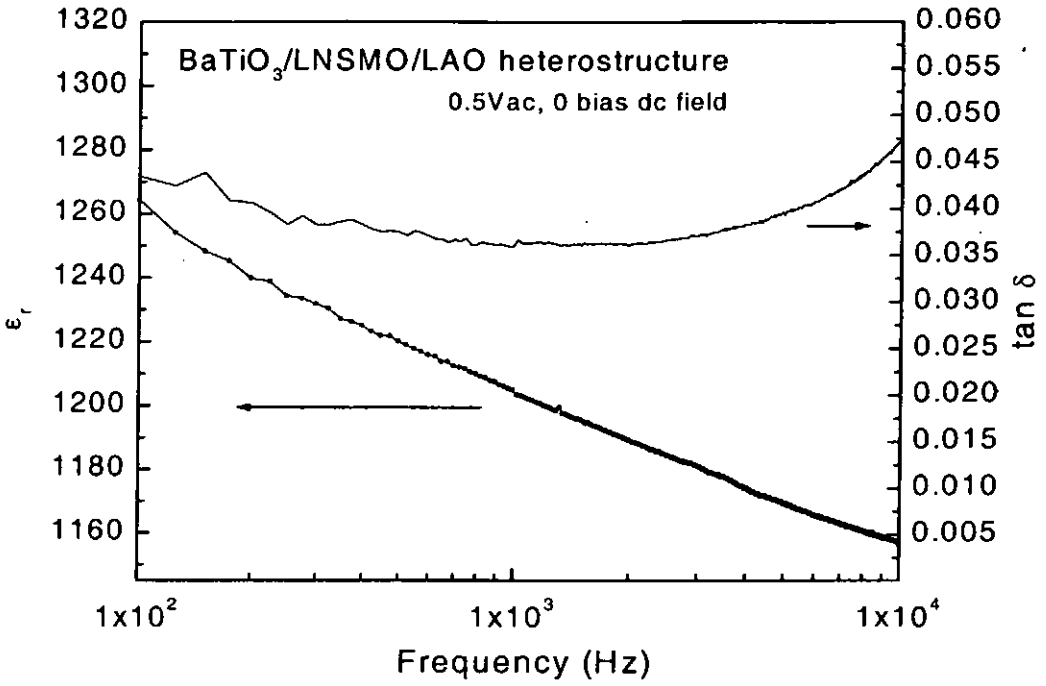

Figure 5.1.2.8 Frequency dependence of dielectric constant and loss tangent of $BaTiO_3$ films on top of LNSMO.

5.1.3 PZT/LNSMO/LAO

As a comparison for $BaTiO_3$ insulating system, $Pb(Zr_{0.52}Ti_{0.48})O_3$ (PZT) is used as the insulating layer. PZT possesses large dielectric constant and ferroelectric properties. It is interesting to study the difference in the tri-layer structure based on these two different insulators. Especially, we are interested to see whether the ferroelectric property will have any influence on the behavior of the tri-layer structure. To compare with the $BaTiO_3$/LNSMO/LAO heterostructures, optimized PZT on LNSMO/LAO was fabricated based on the experience of previous studies. [Wu et al., 2000c]

5.1.3.1 Fabrication

LNSMO films on LAO substrates were fabricated using same processing parameters as in the fabrication of the $BaTiO_3$/LNSMO/LAO heterostructures. The PZT films were then deposited in-situ on top of these LNSMO layers. The PZT films were deposited with laser fluence of 3 J/cm^3 operating at 10 Hz, the deposition temperature was kept at 650 °C under 200 mTorr ambient O_2. The as-grown heterstructures were cooled down at 1 atm of oxygen. Thickness of the PZT films was kept at about 500 nm.

5.1.3.2 Structure characterization

The crystal structure of the prepared PZT/LNSMO/LAO heterostructures was characterized by XRD. The XRD θ–2θ scans only show peaks corresponding to the planes of {001} families of PZT and LNSMO layers on LAO(001) substrates (figure 5.1.3.1). This indicates that these films are single phase and highly oriented. The FWHM of the PZT(002) and LNSMO(002) rocking curves are about 1.0181° and 1.0102° respectively, while the FWHM of the LAO substrate at (002) plane is 0.2346°

(figure 5.1.3.2). The narrow ω-scan rocking curves of (002) planes of PZT and LNSMO together with the X-ray 360° ϕ-scans of (202) planes of PZT, LNSMO and LAO (figure 5.1.3.3) provide evidences for the high crystallinity and cube-on-cube epitaxial growth of the PZT and LNSMO films on LAO substrates.

SEM images of surface morphology and cross-section of the PZT/LNSMO/LAO heterostructures are shown in figure 5.1.3.4. From the surface image, shown in figure 5.1.3.4 (a), the PZT film with lateral grain size about 100 nm is observed. The grains are approximately square in shape and closely packed together. From the cross-sectional view (figure 5.1.3.4 (b)), columnar structure of PZT is observed and it seems to be extended from the interface of PZT/LNSMO to the surface.

In general, our XRD and SEM results shows that PZT fabricated on LNSMO/ LAO shows good crystallinity and is epitaxially grown in <001> orientation normal to the surface. The film obtained has smooth surface and is densely packed.

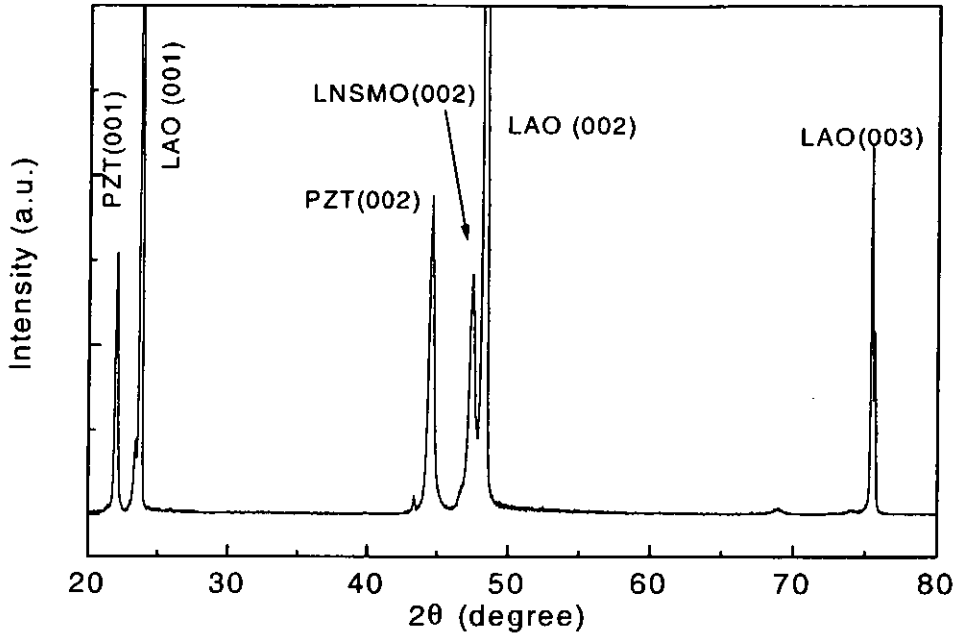

Figure 5.1.3.1 XRD θ–2θ pattern of PZT/LNSMO heterostructures growth on LAO(001) substrate.

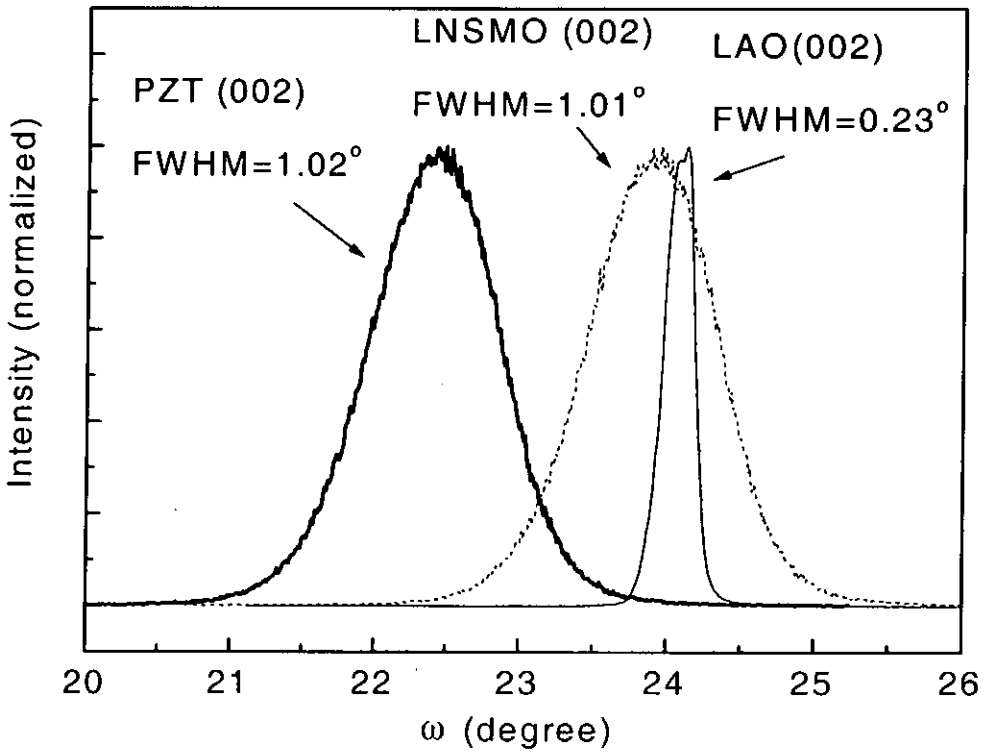

Figure 5.1.3.2 XRD ω-scan rocking curves of PZT, LNSMO and LAO substrate.

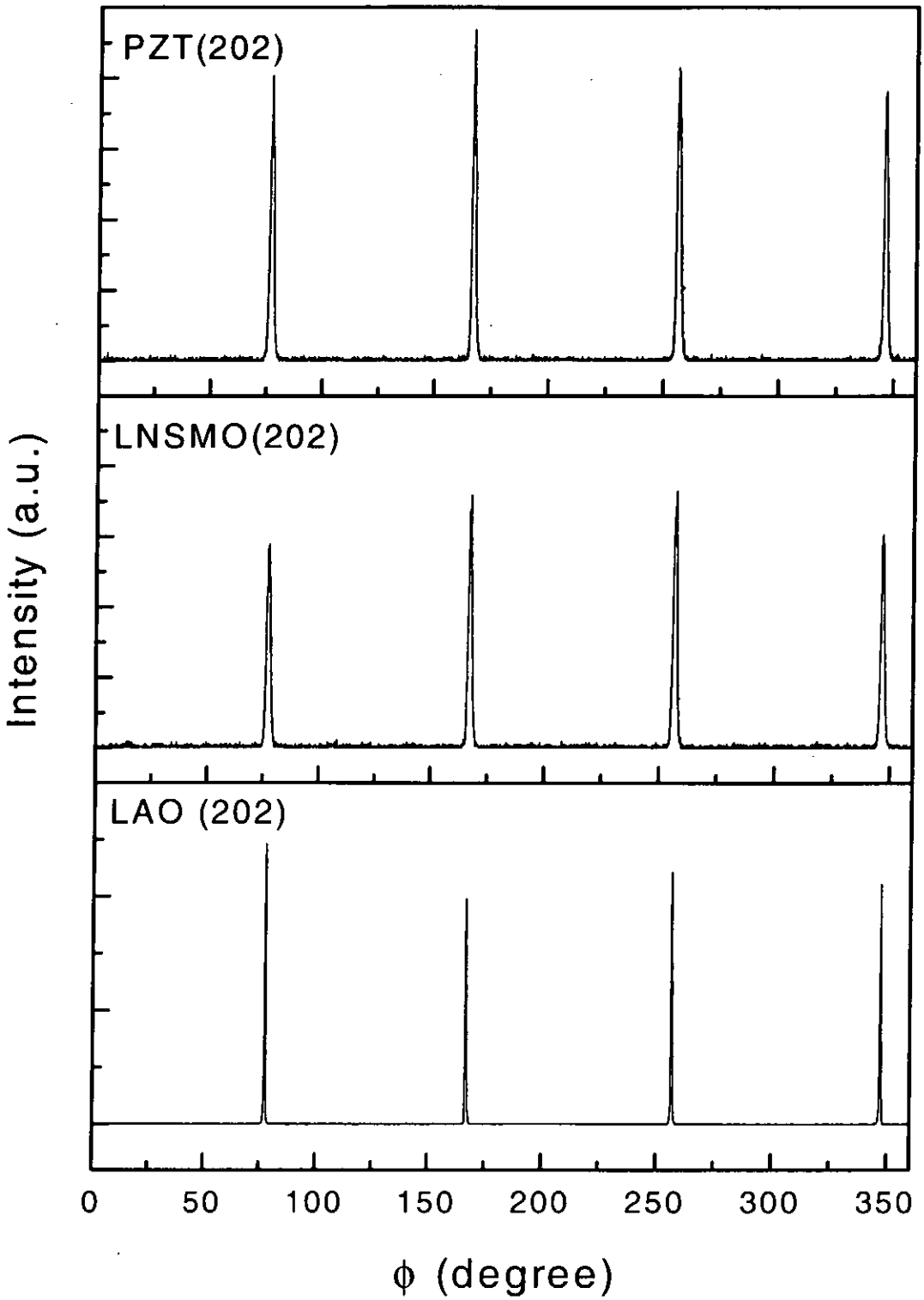

Figure 5.1.3.3 The The ϕ-scans of the PZT(202), LNSMO(202) and LAO(202) of PZT/LNSMO/LAO heterostructures.

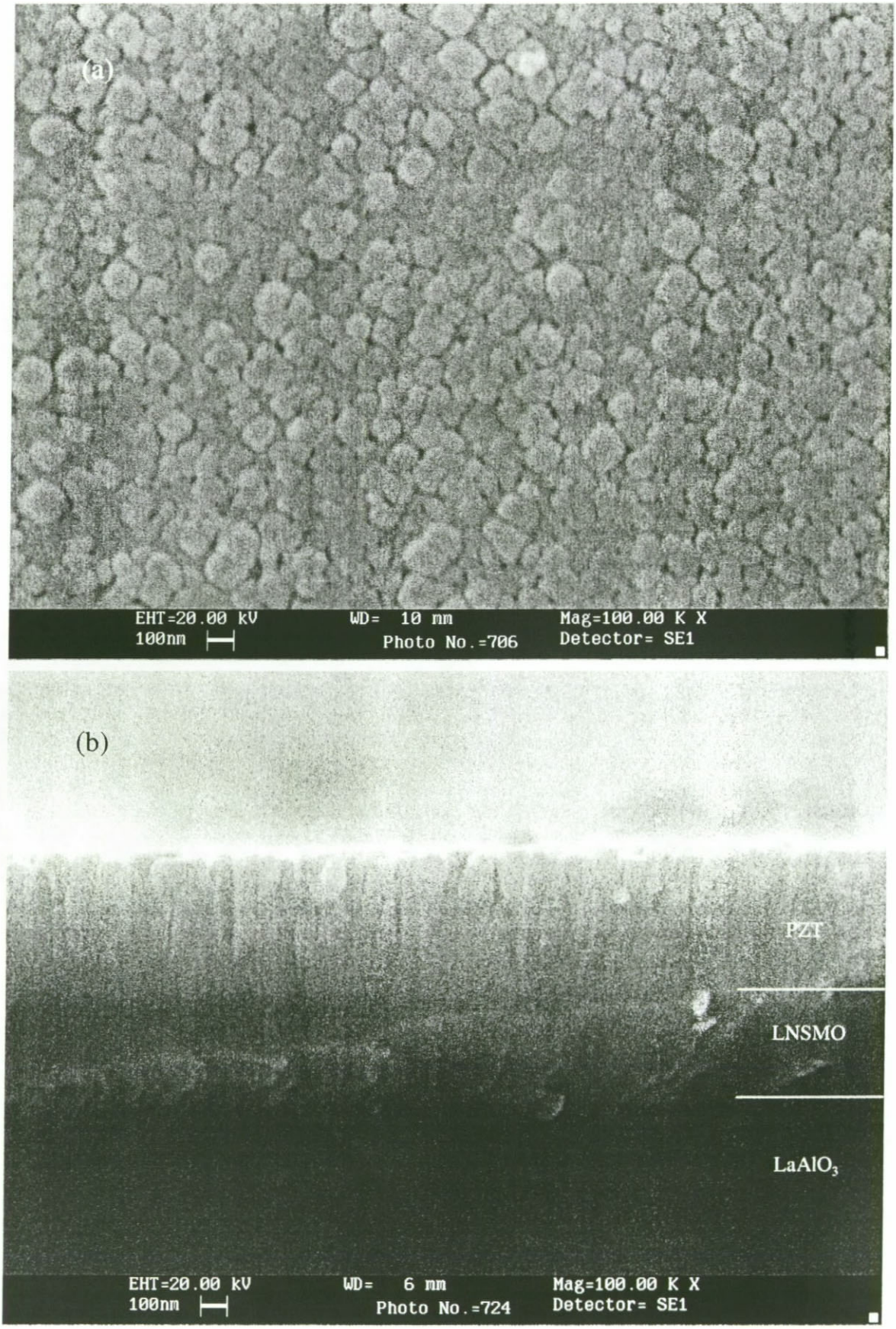

Figure 5.1.3.4 SEM's surface morphology (a) and cross section (b) images of PZT/LNSMO/LAO heterostructures.

5.1.3.3 Electrical measurement

As a comparison with the $BaTiO_3$/LNSMO/LAO heterostructures, similar electrical measurements on PZT/LNSMO/LAO heterostructures were performed. Polarization-voltage (*P-E*) relationship of the PZT layer was done at room temperature at 1 kHz. *P-E* hysteresis loops shown in figure 5.1.3.5 clearly indicate the ferroelectric characteristic of the PZT layer. With 10 V driving voltages, the remnant polarization (P_r), saturation polarization (P_s) and coercive field (E_c) of the PZT layer are 24 $\mu C/cm^2$, 33 $\mu C/cm^2$ and 50 kV/cm respectively. A remarkable difference from the $BaTiO_3$ film is observed in the permittivity curve of PZT layer under a DC biased voltage, as shown in figure 5.1.3.6. The maximum points of the curve shift away from zero bias voltage and are depended on the direction of the applied DC field. This results in a "butterfly" hysteresis curve which separates the maximum peaks on either side around the zero bias point. The maximal width between the two maximum points in the "butterfly" curve is about twice of the coercive field value and the peak positions appear in the vicinity of the coercive field for the *P-E* hysteresis loop. The appearance of the curve is another evident of the ferroelectricity of the PZT layer and it is understandable in terms of the underlying domain switching process as it has been described for $BaTiO_3$ layer in the last section. At field close to the coercive field of *P-E* hysteresis loop, the dielectric behavior of the PZT appears "soft" and reachs maximum relative dielectric permittivity which is suggested as a result of the switching process by most of the domains during the applied DC field. The maximum relative dielectric permittivity reachs 1200 at around 35 kV/cm and is suppressed to around 450 at 100 kV/cm. The reduction of the relative dielectric permittivity is about 62.5%. Figure 5.1.3.5 and figure 5.1.3.6 indicate that the deposited PZT film possesses ferroelectricity.

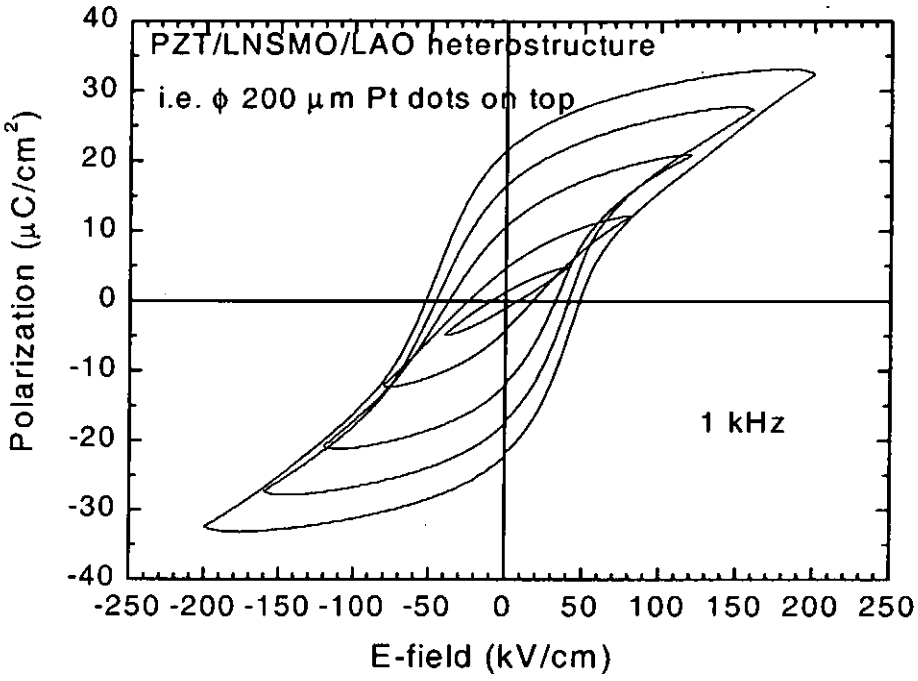

Figure 5.1.3.5 *P-E* measurement of PZT/LNSMO/LAO heterostructures with applied voltages of 2, 4, 6, 8 and 10 V

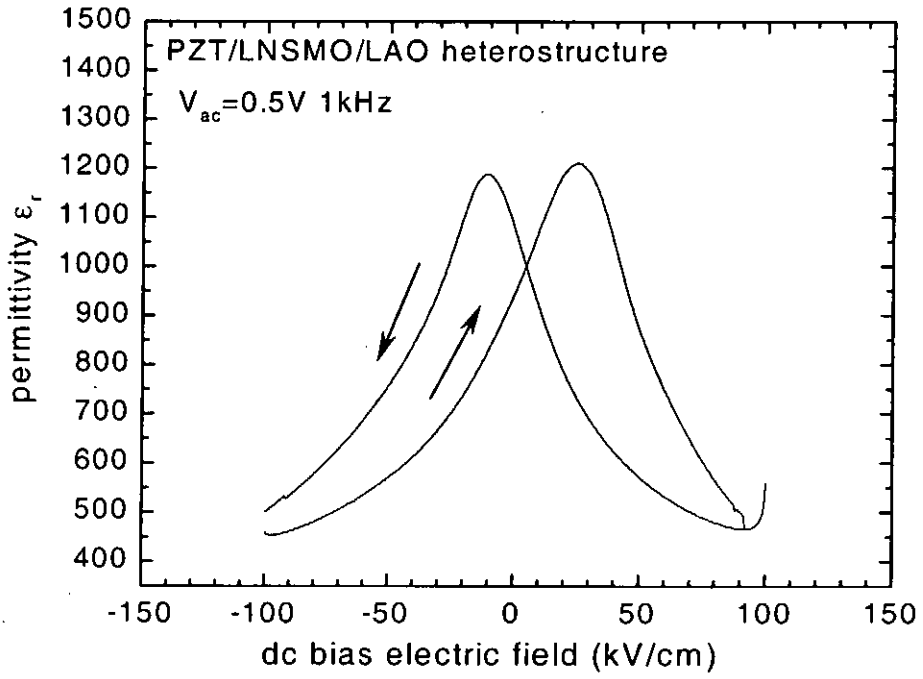

Figure 5.1.3.6 Relative dielectric permittivity of PZT films on LNSMO/LAO as a function of DC electric field bias.

Figure 5.1.3.7 plots the derivative of *P-E* hysteresis loop ($\varepsilon = \partial P/\partial E$) measured as a function of AC field. Physically, this *P-E* hysteresis loop is obtained by apply a strong AC field of 1 kHz and its derivative, differential permittivity, is plotted as a function of the instantaneous value of the AC field with amplitude larger than the coercive field. Hence, this curve is describing the instantaneous dynamic motion of the domain switching process under the applied field. It is noticed that the domain reorientation process is very active at the coercive field around 45 kV/cm. This gives rise to a steep slope observed in the *P-E* loop as well as a high derivative value. Above 50 kV/cm, the movable domains are reduced. This results in a steady change in *P-E* loop and a relatively constant of $\partial P/\partial E$ value. When the field strength decreased, some domains will back-switch, but the polarization is still nonzero at zero field. An opposite field brings the polarization to zero again. This opposite field is caused by other oppositely re-orientated domains that happen to be other peak of $\partial P/\partial E$ value. Further decrease of field in the negative direction causes a new alignment of dipoles in the domain but the number of switchable domain is reduced as the field continuous to increase in opposite direction. As a result, the $\partial P/\partial E$ value reduces again while the field strength is increase.

Figure 5.1.3.8 shows the frequency dependent of dielectric constant and loss tangent of the PZT films under the applied sub-switching field. The dielectric constant and loss tangent of the PZT films are about 680 and 0.105 respectively at 1 kHz.

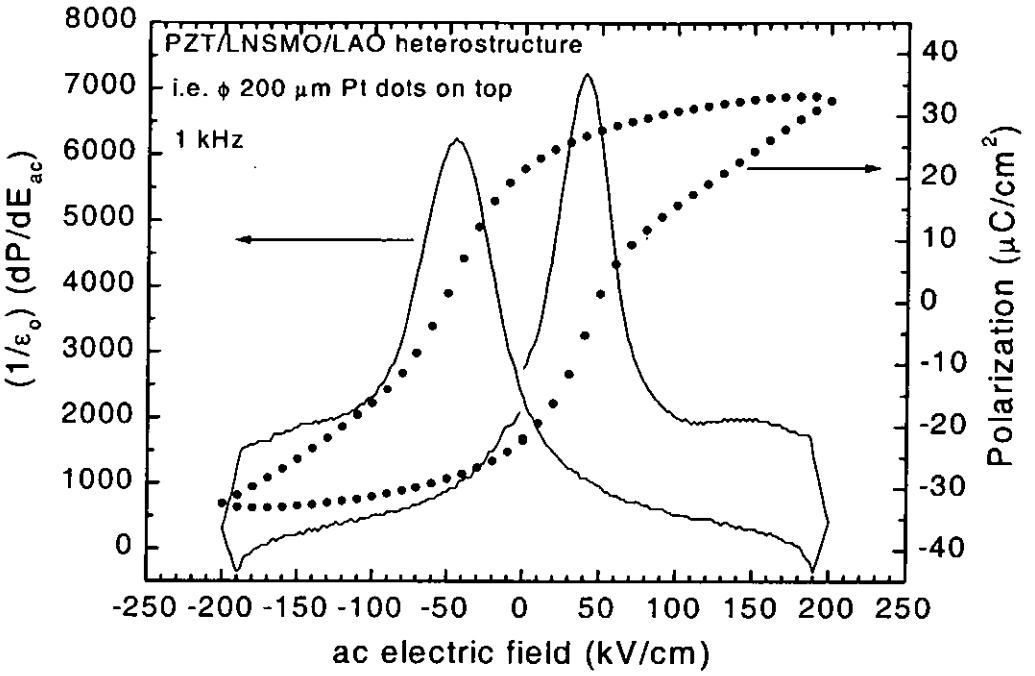

Figure 5.1.3.7 derivative d*P*/d*E* as a function of an AC electric field of PZT films on LNSMO/LAO and the corresponding *P-E* hysteresis loop.

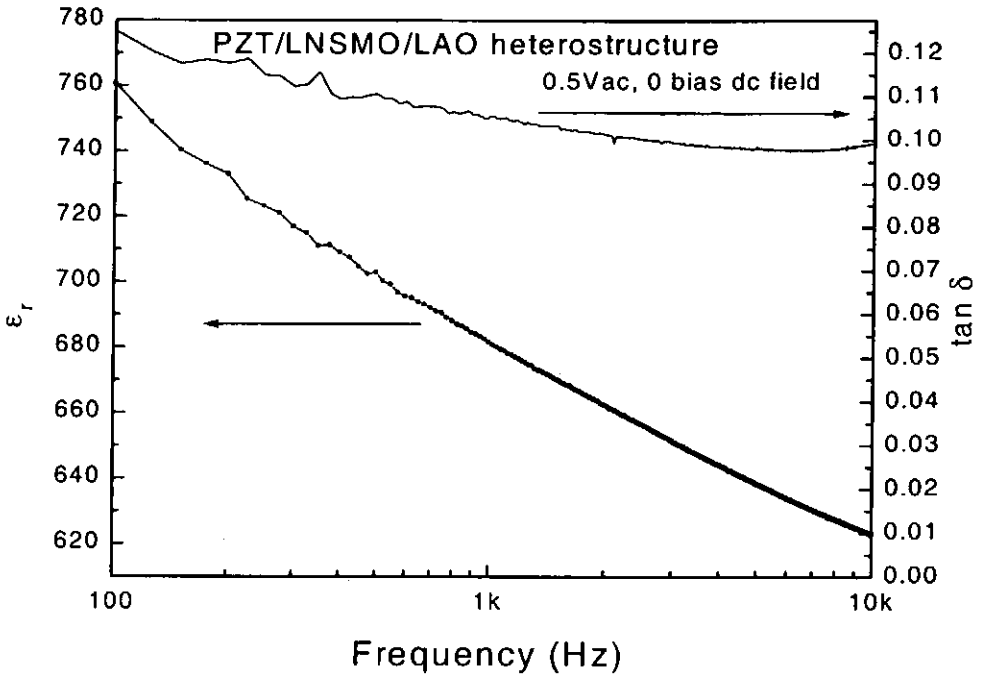

Figure 5.1.3.8 Frequency dependence of dielectric constant and loss tangent of PZT films on top of LNSMO.

5.2 Phosphor layer

Since ZnS:Mn has very high luminous efficiency, it was chosen for the phosphor layer. Before fabricating the tri-layer structure, the technique and processing conditions for depositing single layer ZnS:Mn films using PLD method were studied in order to investigate the relation between the processing parameters and the structural as well as optical properties. ZnS:Mn films were deposited under different temperatures and ambient environments. Two different substrates have been used, namely, (001) silicon wafers and ITO-coated glasses. The ZnS targets used in this work were doped with Mn of 1% by weight and obtained from Target Materials, Inc. The laser ablation of the ZnS target was carried out with an ArF excimer laser (Lambda Physik, 193nm, 20 ns) focused on the rotating target at an incident angle of 45°. The laser fluence was ~2 J/cm^2. Deposition experiments were performed in a vacuum chamber which was evacuated to a base pressure of 1.5×10^{-4} Torr and then back filled with various Ar pressures ranging from 0.3 Torr to 1.5 Torr. Substrate temperature during deposition was varied between 150 °C and 500 °C.

5.2.1 ZnS:Mn on (001) Si

Preliminary studies on fabricating ZnS:Mn films on Si (001) substrates were done in a vacuum of 5×10^{-5} Torr evaculated by a diffusion pump. Different substrate temperatures ranging from 200 °C to 600 °C were used. However, none of these films showed characteristic peaks of ZnS under XRD θ–2θ inspections. Furthermore, no film showed observable luminescence under the irradiation of UV mercury lamp. Indeed, under this high vacuum condition, the deposition rate was very low. For those depositions above 550 °C, severe re-sputtering feature was observed. In general, films of unknown structure and stoichiometry were grown under relatively high vacuum.

Breakthrough began with the introduction of Ar gas into the chamber with

pressure up to 300 mTorr while the substrate temperature maintained at 450 °C during deposition. Under these deposition conditions, the ZnS:Mn films showed very weak luminescence when irradiated by an UV lamp. Afterwards, studies varying Ar pressure and substrate temperature with the range mentioned above were conducted.

5.2.1.1 Fabrication

The 5x10 mm^2 cut Si (001) substrates were first immersed into a 10% mole of HF solution for 10 minutes to etch away the surface oxide. After rinsing with deionized water, the substrate was pasted onto the sample heater and mounted into the chamber. For the films grown at different deposition temperatures, the chamber was first evacuated to 10^{-5} Torr and then heated up to the decided temperature (ranging from 150 °C to 500 °C). Before deposition, the chamber was flushed with Ar gas of 99.99% purity for at least 3 times and then filled up to 500 mTorr. After that the ZnS:Mn target was laser ablated in order to grow film on Si (001) substrate. Without post-deposition annealing, the films were immediately cool down inside the chamber with the same Ar pressure. For those films grown with varying ambient pressure, the deposition temperature was kept at 450 °C while the background Ar pressure during deposition changed from 300 mTorr up to 1.5 Torr. After deposition, the films were again cool down at the same ambient Ar pressure. Film thickness, controlled by the time duration of the laser ablation, was maintained within 600 nm to 800 nm in our studies. The thickness of the films was checked with a surface profiler.

5.2.1.2 Structure Characterization

XRD was used to characterize the structure of the deposited ZnS:Mn films. Figure 6.2.1.1 shows the XRD θ–2θ patterns of ZnS:Mn films grown on Si (001) substrates with different substrate temperatures. At low substrate temperature (150 °C), only diffraction peaks arisen from zinc-blende (cubic) structure with a preferred

(111) orientation of ZnS were observed. As substrate temperature increases, peaks corresponded to wurtzite (hexagonal) structure were appeared. As a result, the films contained a mixed phase of both zinc-blende and wurtzite structure, and became polycrystalline. As the temperature further increased above 450 °C, the wurtzite phase without preferred orientation became dominant. This demonstrated that low substrate temperature facilitated the formation of zinc-blende structure with a preferred (111) orientation while wurtzite phase became dominant at high substrate temperature.

In addition to the crystallinity orientation, grain size and surface morphology of these ZnS:Mn films were also examined. The SEM images in figure 5.2.1.2 reveal that the deposited films are, in general, smooth and crack-free with grain size of ~100 nm. However, there is a change in the shape of the grain as substrate temperature increased. For films grown at lower substrate temperature (150°C) as shown in Figure 5.2.1.2a, the grains were circular in shape with a narrow size distribution. As the deposition temperature increased, the grains were elongated and showed an irregular grain growth with some degree of grain agglomeration. This results in a much wider size distribution.

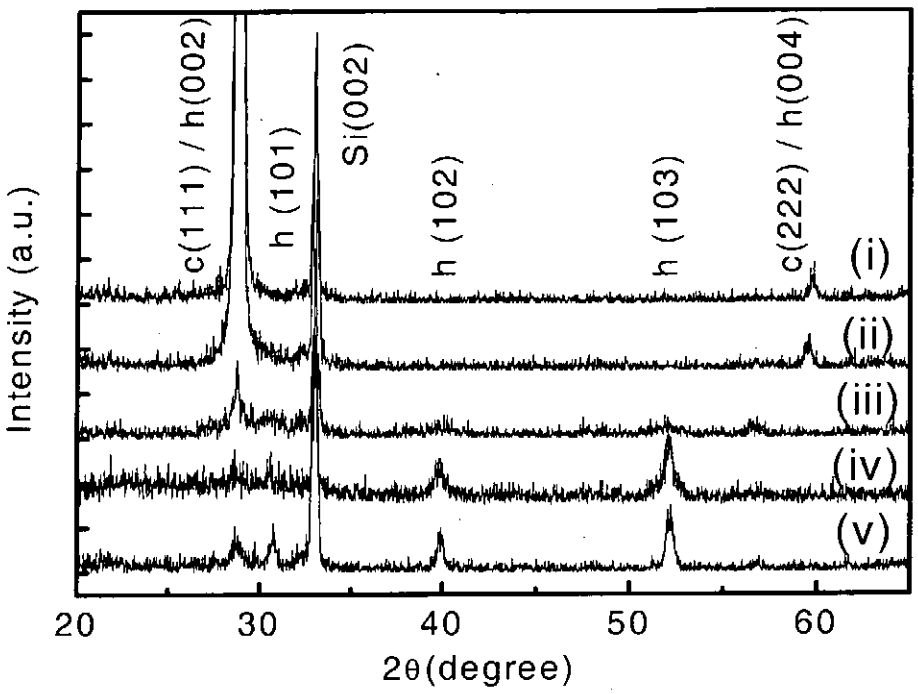

Figure 5.2.1.1 XRD patterns of ZnS:Mn films grown on Si (001) with substrate temperatures of (i) 150 °C, (ii) 250 °C, (iii) 350 °C, (iv) 450 °C and (v) 500 °C.

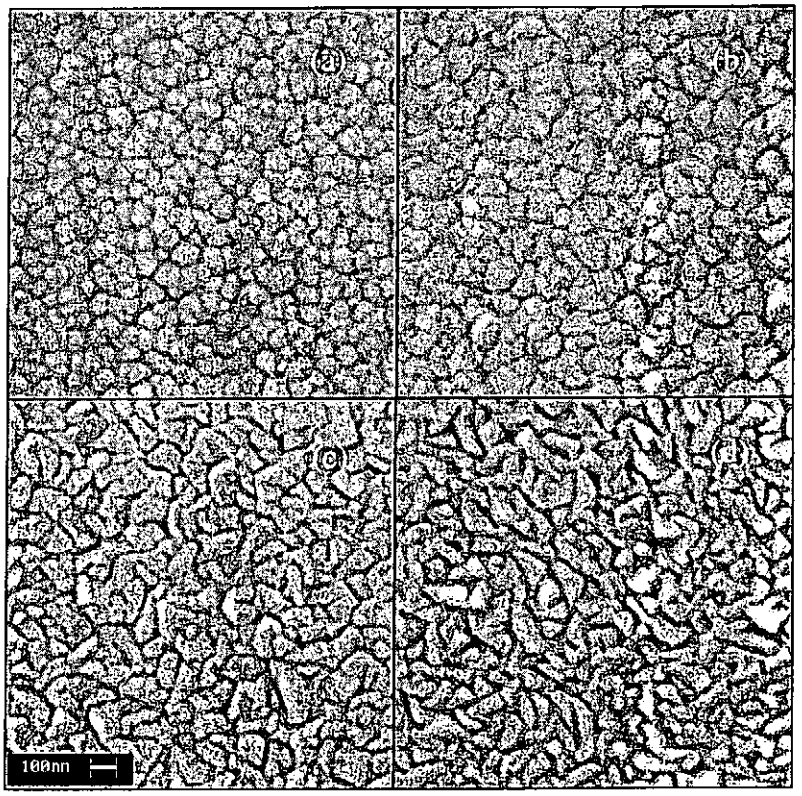

Figure 5.2.1.2 SEM images of ZnS:Mn grown on Si (001) with 500 mTorr back-filled Ar pressure and at substrate temperatures of (a) 150 °C, (b) 250 °C, (c) 350 °C, and (d) 450 °C.

On the other hand, ZnS:Mn films grown on Si (001) substrates with various ambient backfilled Ar pressure from 300 mTorr to 1.5 Torr were also conducted. The deposition temperature was fixed at 450 °C. Figure 5.2.1.3 shows the XRD θ–2θ patterns of these ZnS:Mn films. It in noticed that there is no significant difference in the XRD patterns. All patterns show the existence of both zinc-blende and wurtzite characteristic peaks and appear as the typical ZnS:Mn films grown at a higher substrate temperature with wurtzite phase dominated structure. The results demonstrate that ambient Ar pressure during deposition has no significant change on the structural properties.

Grain size and surface morphology of these ZnS:Mn films were examined by the SEM. The SEM images in figure 5.2.1.4 reveal that the deposited films are smooth and crack-free with grain size of ~ 100 nm. At deposition temperature of 450 °C, these films do not show any difference between various ambient Ar pressure. These films, in general, have elongated grains and show irregular grain growth with grain agglomeration feature. Hence, this results in a wider size distribution.

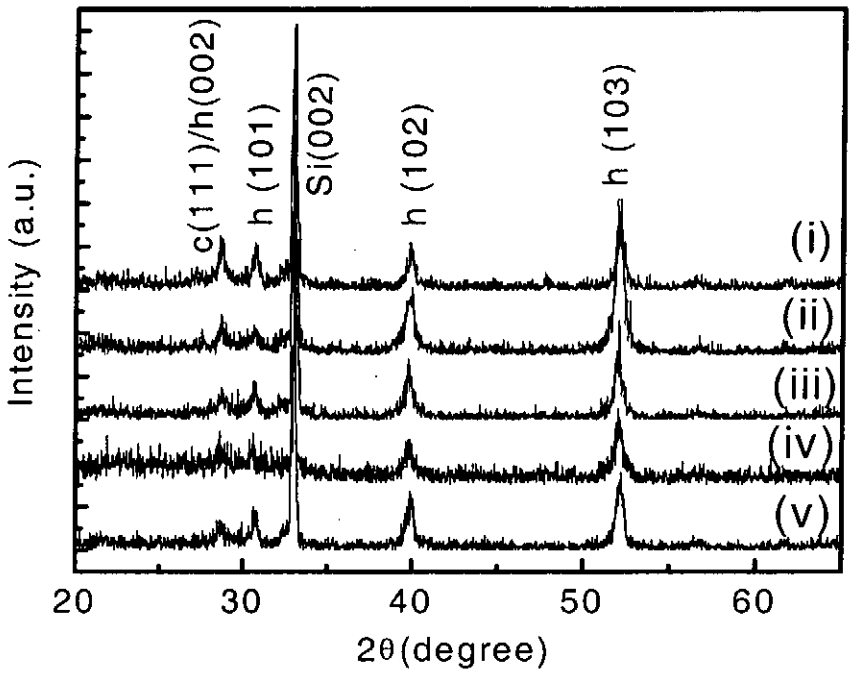

Figure 5.2.1.3 XRD patterns of ZnS:Mn films grown on Si (001) with ambient Ar pressures of (i)1.5 Torr, (ii)1 Torr, (iii)700 mTorr, (iv)500 mTorr and (v)300 mTorr.

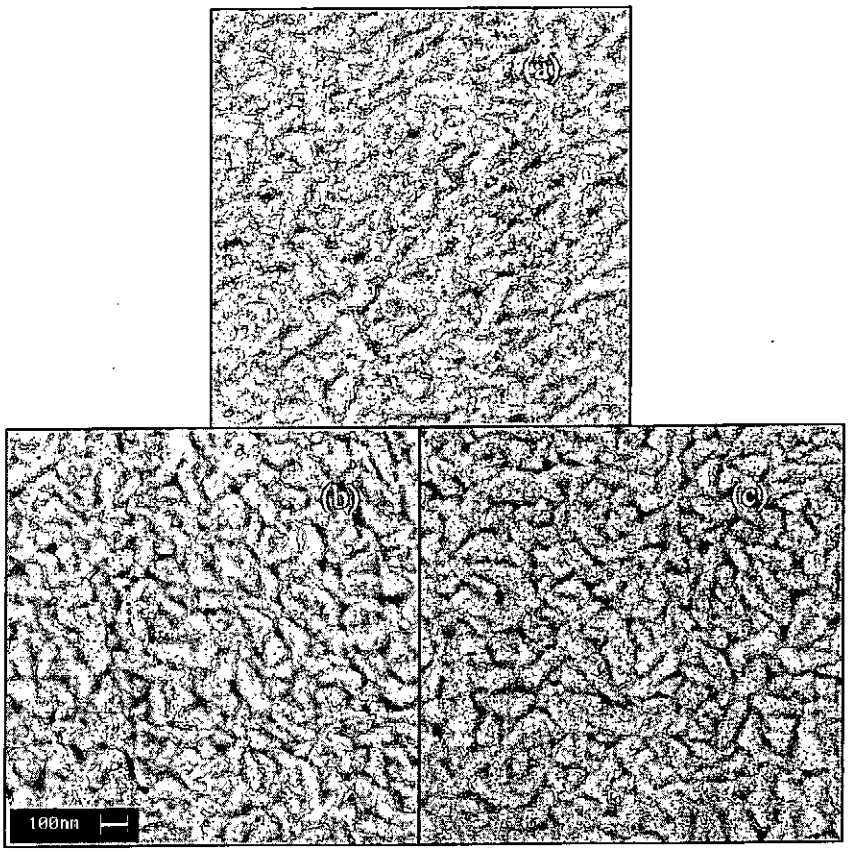

Figure 5.2.1.4 SEM images of ZnS:Mn grown on Si (001) with 450 °C substrate temperatures and with ambient Ar pressure of (a) 300 mTorr, (b) 500 mTorr and, (c) 1 Torr.

5.2.1.3 Optical Properties

Besides structural properties, the optical properties of ZnS:Mn are also very important in determining the performance of the tri-layer structures. In this part of studies, the optical properties of the ZnS:Mn films were investigated. Optical measurements of the ZnS:Mn films deposited at different temperature were characterized by photoluminescence (PL), ellipsometric and transmittance measurements. In the PL measurement, the films were excited by a 488 nm laser beam from an argon ion laser (Coherent Innova 70) with power of 100 mW. PL spectra were recorded by a double grating monochromator (Spex 1403) equipped with the standard photon counting equipment. Figure 5.2.1.5 shows the PL spectra of the films deposited on Si (001) at 150 °C and 450 °C. The PL spectra show an orange-

yellow emission band at ~ 590 nm which is due to the ${}^4T_1(G) - {}^6A_1(S)$ transition of the Mn^{2+} [McLaughlin et al., 1993]. As substrate temperature increased, the PL band becomes narrower and shifts to lower wavelength. Inset shows the peak position of this PL band as a function of substrate temperature. In host matrices of different crystal symmetry, the crystal-field splitting of the $3d^5$ electron configuration of Mn^{2+} is difference. Hence the energy in the transition of ${}^4T_1(G) - {}^6A_1(S)$ of Mn^{2+} ions could be different in zinc-blende ZnS and wurtzite ZnS. Similar shift have been reported for the EL emission band observed in ZnS:Mn films [Yamamoto, 1998; Ono, 1995]. Therefore, we suggest that the shift in the PL peak position as well as the broadening of the PL band could be due to the superimpose of the emissions of Mn^{2+} ions under different ratios of zinc-blende to wurtzite phase presence in our ZnS films.

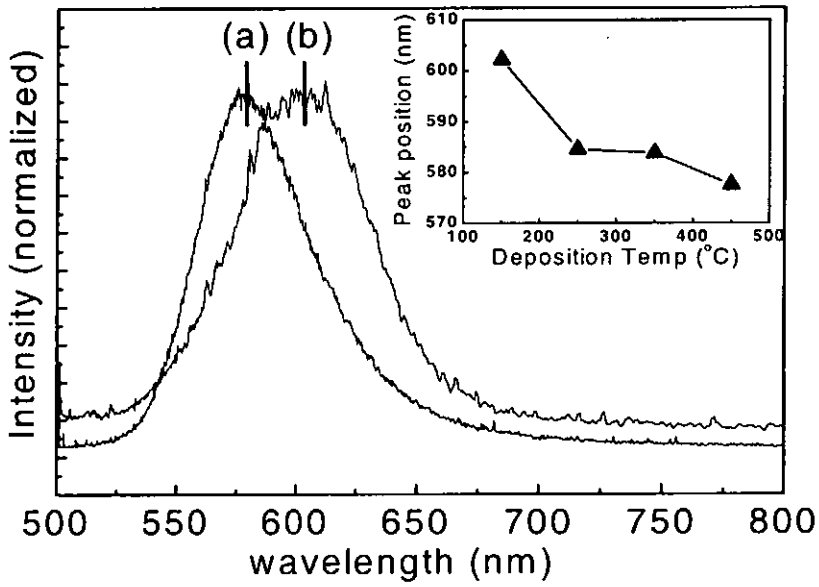

Figure 5.2.1.5 PL spectra of ZnS:Mn films on Si (001) deposited at (a) 450 °C and (b) 150 °C. Inset is the peak position of PL band as a function of substrate temperature.

Since the refractive index dispersion of the zinc-blende and wurtzite structure of ZnS are different, we used their the change in refractive index as an indicator to determine the different structural components of the ZnS films. To measure the refractive index of the films, we used spectroscopic ellipsometry (SE) technique. SE is a nondestructive technique using light reflection. In conjunction with computer modeling of the experiment data, SE is capable to determine the refraction index dispersion as well as depth profiling of thin film samples with depth resolution in the angstrom range.

Ellipsometric measurements were carried out by a spectroscopic phase modulated ellipsometer (Jobin Yvon UVISEL) in the wavelength range of 350 – 850 nm at 5 nm intervals. All measurements were performed at a 70° angle of incidence with the analyzer and modulator set at 45° and 0°, respectively. The obtained spectra were best fitted using the double layer Sellmeier (DLS) model. The parameters, including the thickness of the films, obtained from each of the fittings were used to simulated n by the following dispersion relations: [Ward, 1994]

$$n^2 = A + B \times \frac{\lambda^2}{\lambda^2 - C^2} \qquad \textbf{(5.2.1.1)}$$

where n is the refractive index, and A, B and C are positive constants. Here, λ represents the wavelength ranging from 350 to 850 nm. Film thickness of our deposited films was also measured by a surface profile (KLA-Tencor P-10) in order to compare with our fitted results.

Dispersion curves of the two ellipsometric parameters, Ψ and Δ, for ZnS:Mn film with substrate temperature equals to 350 °C is shown in figure 5.2.1.6. In general, all the films show a similar feature with oscillations due to film thickness. Our initial analysis was based on a single layer Sellmeier model. Poor agreement, however, was obtained with the experimental data. In subsequent analysis, we modified the single layer Sellmeier model into a double layer Sellmeier (DLS) model. In this model, we assume that the films consist of two layers: a bottom bulk ZnS:Mn layer and a surface layer that composed of bulk ZnS:Mn as well as void. These voids in the surface layer

are mainly caused by surface roughness and porosity. Figure 2.5.1.7 shows the DLS model for our ZnS:Mn films. Based on this modified DLS model, better-fit results were obtained. The solid lines in figure 5.2.1.6 denote these fitted results. The volume fraction of void *f*, effective thickness of surface layer d_s and bottom layer d_b, and the other three parameters (A, B and C) obtained by DLS model are shown in Table 5.2.1.1.

After securing the fitting parameters, the refractive index dispersion spectra for the bottom layers, n_b, evaluated using Equation (5.2.1.1), are plotted in Fig. 5.2.1.8 (a) as a function of substrate temperature. The Bruggeman effective medium approximation (EMA) [Landauer, 1978; Bruggeman, 1935] was used to describe the refractive index dispersion spectra for the top ZnS:Mn layers, which is expressed by

$$(1-f)\frac{n_b^2-n_s^2}{n_b^2+2n_s^2}+f\frac{1-n_s^2}{1+2n_s^2}=0 \qquad \textbf{(5.2.1.2)}$$

where n_b is the refractive index of the bottom layer (i.e. the bulk ZnS:Mn) and n_s is the effective refractive index of the surface layers. According to Bruggeman effective medium approximation, a large void fraction leads to a lower refractive index for the upper layer. Figure 5.2.1.8 (b) shows the n_s dispersion spectra as a function of substrate temperature for the upper ZnS:Mn layers.

In general, the refractive indices n_s and n_b of the ZnS:Mn films increase with shorter wavelength. As the substrate temperature increases, the spectra shift upwards indicating that the refractive index increases with substrate temperature. For instant, when the substrate temperature is 150 °C, the refractive index n_b of the bottom ZnS:Mn layer is about 2.44 at 500 nm, while the corresponding value for 450 °C film is about 2.50. The rise of refractive index seems to be more pronounced as the substrate temperature increased from 150 °C to 250 °C and becomes less distinct between 250 °C and 450 °C. Similar temperature dependence is also observed in the n_s spectra. The escalation of n_b with substrate temperature may be a result of either change in the structure (wurtzite and zinc-blende) or increasing density. It is known

that the refractive index of the wurtzite ZnS structure is larger than that of zinc-blende ZnS structure. Also, the refractive index is increased with the density of the film. But it is interesting to compare the temperature change of refractive index with the temperature change of PL peak positions obtained from the PL measurement. A pronouncing change between 150 °C and 250 °C and a mild change between 250°C to 450°C are observed from both measurements. This suggests that changes in both PL and ellipsometric measurements may be resulted from the same origin, and that is, the increasing wurtzite to zinc-blende ratio with substrate temperature. Based on the fitting parameters in Table 5.2.1.1, we see that both the void percentage and the surface layer thickness are about the same at different substrate temperatures. These results demonstrate that the substrate temperature has no significant effect on the surface roughness of the films. The measured film thicknesses using the surface profile are also shown in Table 5.2.1.1 for comparison. As we observe in the table, the two sets of film thickness data are comparable to each other. However, the discrepancy seems to propagate as the substrate temperature is increased. This can be attributed to the effects of decreasing uniformity in films deposited at higher substrate temperature.

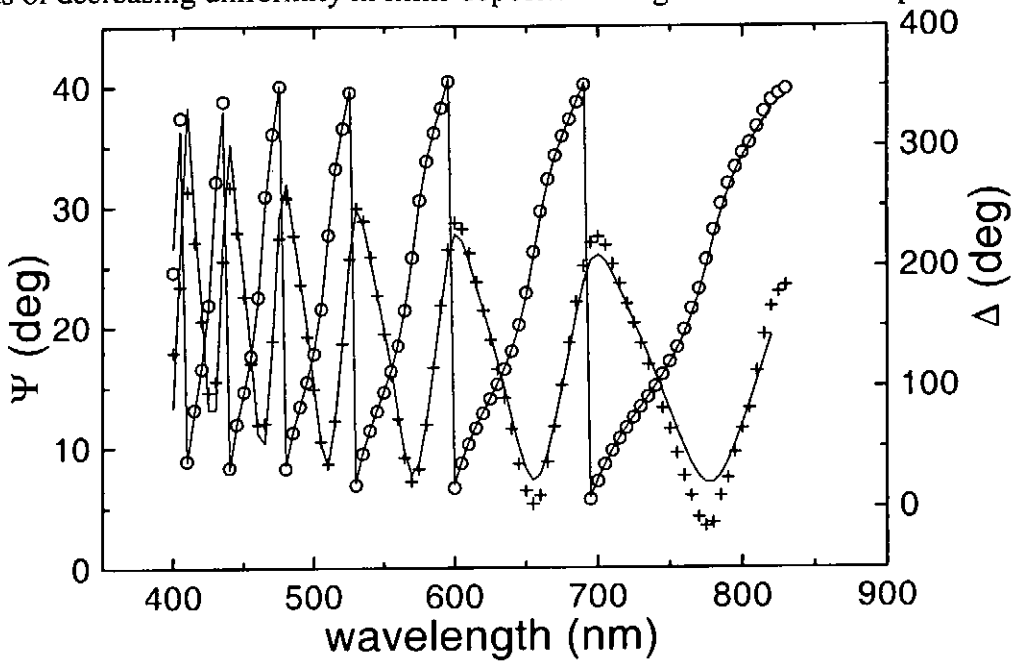

Figure 5.2.1.6 Spectra of the ellipsometric parameters Ψ and Δ as a function of wavelength, obtained from SE experiments for ZnS:Mn film deposited at 350°C. The + and o are the measured Ψ and Δ values respectively, while the solid lineas are obtained from the fitting.

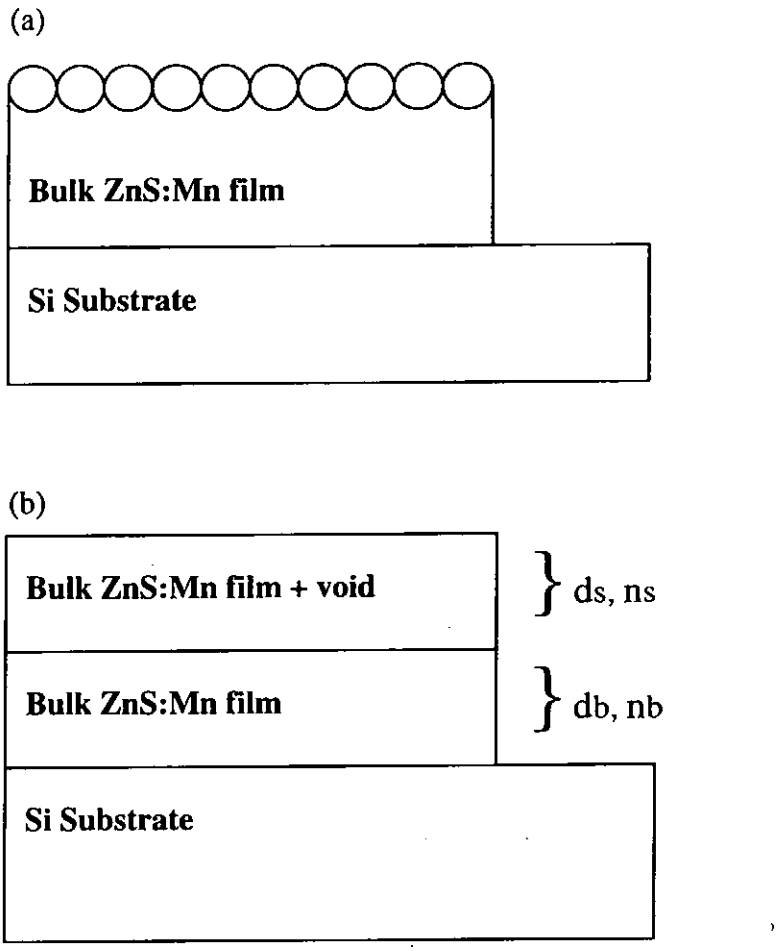

Figure 5.2.1.7 Schematic picture of the DLS model.

Table 5.2.1.1. The fitting parameters of the ZnS:Mn films with different substrate temperatures.

T (°C)	A	B	C	d_b (nm)	d_s (nm)	f (%)	Thickness measured by surface profile d (nm)	$(d_b+d_b)/d$
150	3.46	1.73	278.9	699.5	22.9	37.2	720	1.00
250	3.40	1.98	272.8	854.9	24.3	37.0	838	1.05
350	3.31	2.05	267.7	556.3	27.6	34.2	504	1.16

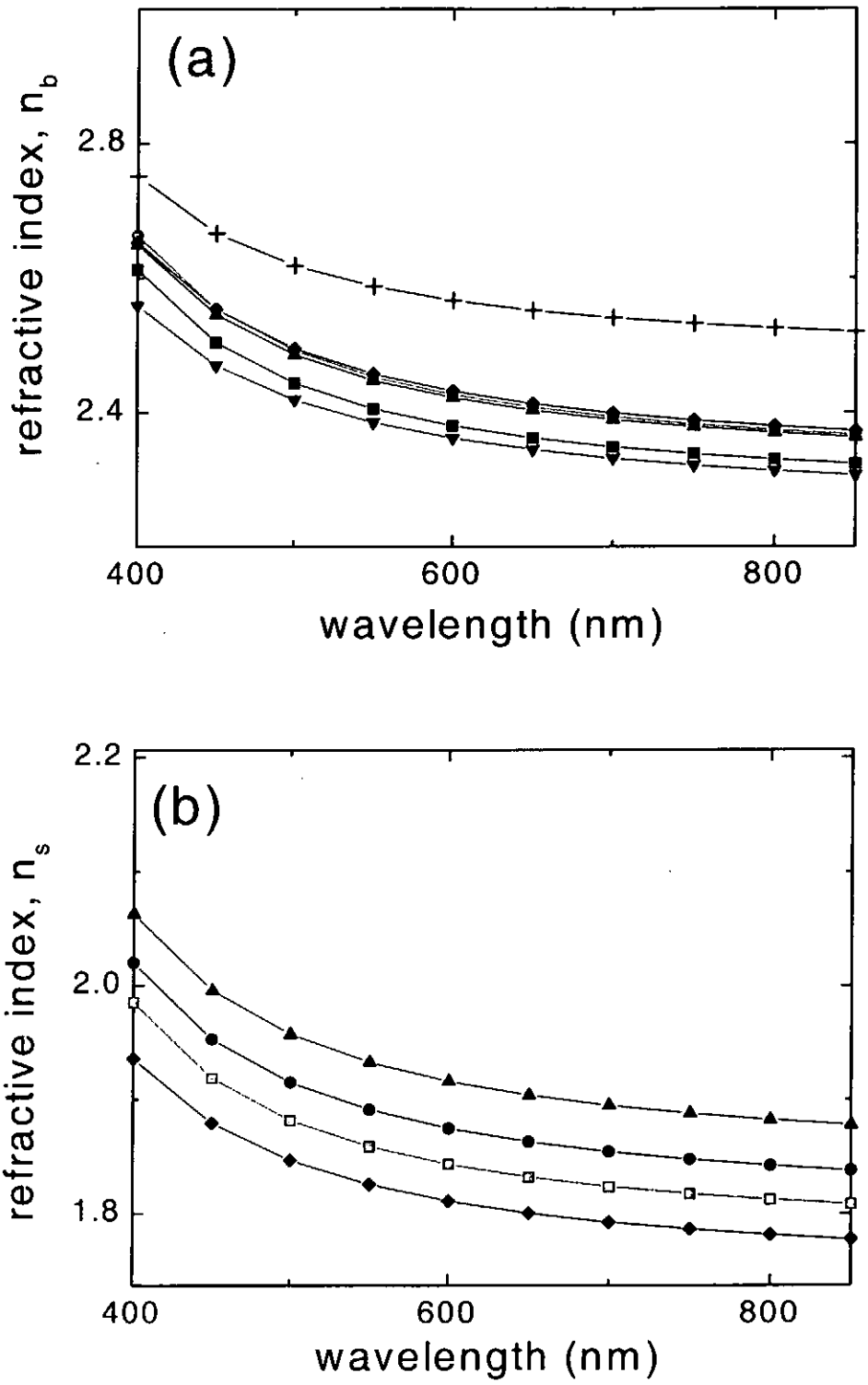

figure 5.2.1.8 (a) The refractive index n_b of the bottom ZnS:Mn layers of 150°C (solid line + ■), 250°C (solid line + ●), 350°C (solid line + ▲) and 450°C (solid line + ◆) obtained by Eq. (1). The dispersion curves for pure ZnS of wurtzite structure (solid line + +) and zinc-blende structure (solid line + ▼) are also shown for reference. (b) The effective refractive index n_s of the upper ZnS:Mn layers of 150°C (solid line + ■), 250°C (solid line + ●), 350°C (solid line + ▲) and 450°C (solid line + ◆) obtained by EMA.

5.2.2 ZnS:Mn on ITO coated glass

Besides Si (001) wafer, ZnS:Mn films were also grown on ITO-coated glass substrates because ITO-coated glass is commonly used as substrate in display devices.

5.2.2.1 Fabrication

Similar to the growing procedure of ZnS:Mn films grown on Si (001) substrate, the ITO-coated glass was used as the substrate instead. With the experience in growing ZnS:Mn films on Si, this study was only concentrated on the substrate temperature effect. Following the same processing condition for ZnS:Mn films on Si, the ZnS:Mn films on ITO-coated glass were prepared.

5.2.2.2 Structure characterization

Again XRD was used for the non-destructive structure investigation. From XRD θ–2θ patterns of the ZnS:Mn films grown on ITO-coated glass at different substrate temperatures shown in figure 6.2.2.1, it is noticed that these films show similar evolution as those grown on Si (001) substrate. At low substrate temperature (150 °C), peak at 28.5° corresponding to the strongest zinc-blende (cubic) (111) line dominates the XRD pattern. When the substrate temperature increases, the zinc-blende (111) structure becomes suppressed while other peaks identifying as the wurtzite structure appear and become clearer with higher substrate temperature. The result suggests that low substrate temperature facilitates the zinc-blende structure formation and high substrate temperature promotes wurtzite structure formation for ZnS:Mn films.

SEM was used to characterize the surface morphology and the grain size of the ZnS:Mn films deposited on ITO-coated glass substrates. It is observed that the shape evolution of the grains are just the same as those grown on the Si (001) substrate, even

the substrates are changed to ITO-coated glasses. Only the size of the grains are a bit smaller when the ZnS:Mn films are grown on ITO-coated glass. In general, smooth and crack-free ZnS:Mn films are successfully grown on the ITO-coated glass by PLD method.

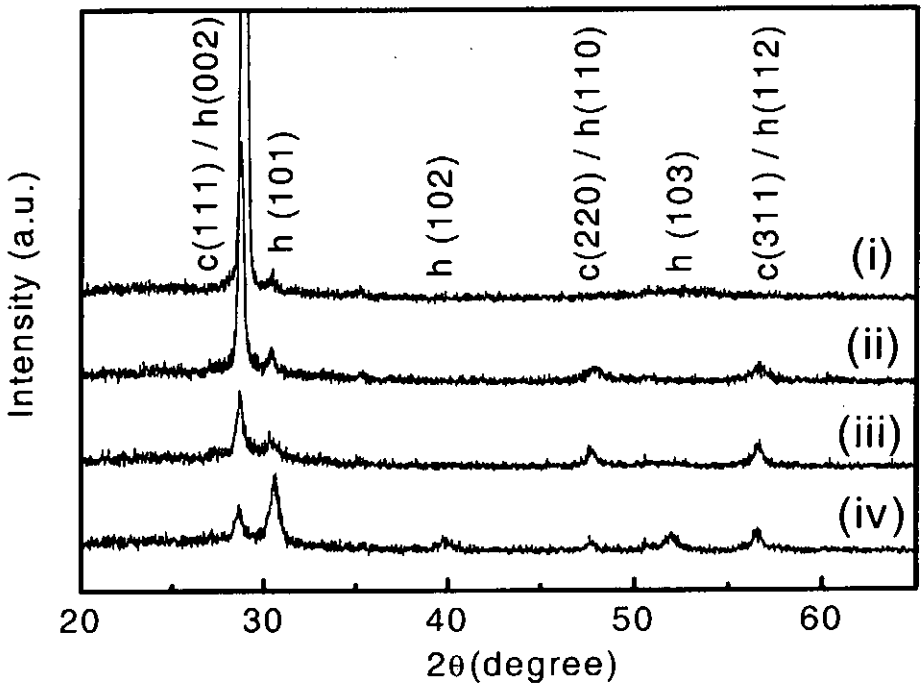

Figure 5.2.2.1 XRD patterns of ZnS:Mn films grown on ITO-coated glass with substrate temperatures of (i) 150 °C, (ii) 250 °C, (iii) 350 °C and (iv) 450 °C.

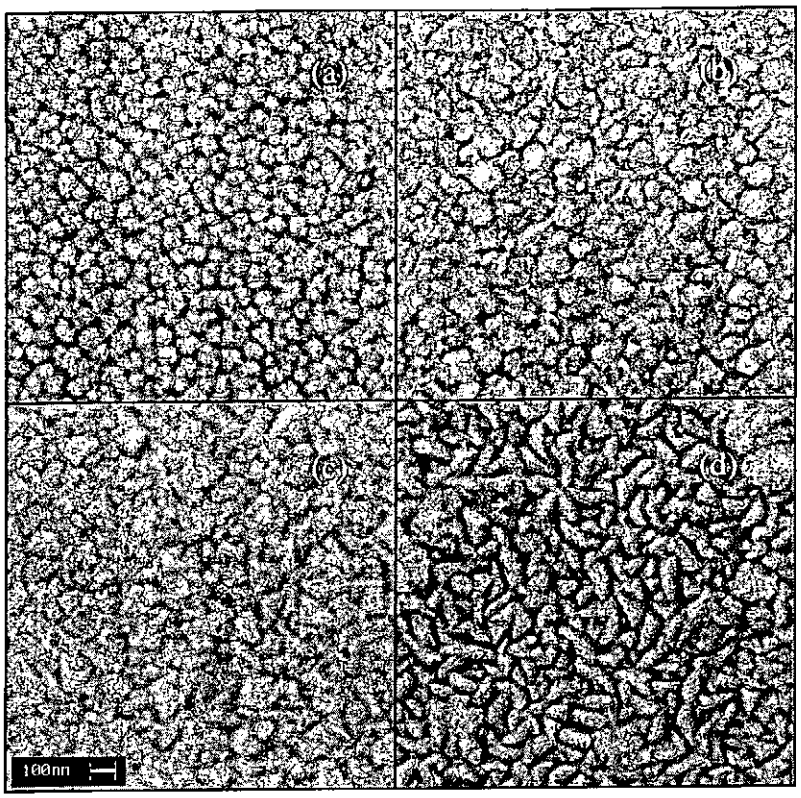

Figure 5.2.2.2 SEM images of ZnS:Mn grown on ITO-coated glass with 500 mTorr back-filled Ar pressure and at substrate temperatures of (a) 150 °C, (b) 250 °C, (c) 350 °C, and (d) 450 °C.

5.2.2.3 Optical properties

The ZnS:Mn films on ITO-coated glass prepared by different substrate temperatures were also investigated by measuring their PL spectra. However due to the strong emission spectra of the ITO-coated glass, it is difficult to obtain a good PL spectrum from the ZnS:Mn films grown on ITO-coated glasses. However, with the advantages of transparency of ITO-coated glass, the optical properties of these films were examined by measuring the optical transmittance. The transmittance measurement was performed by an UV-VIS scanning spectrophotometer (Shimadzu UV – 2101 PC).

Figure 5.2.2.3 shows the substrate temperature dependence of the transmittance of ZnS:Mn films grown on ITO coated glasses. All the films show a good optical transmittance of ~80% in the visible region. The transmittance, however, is slightly deteriorated as the substrate temperature got to ~ 450 °C. The absorption edge for the film deposited at 150 °C is located at ~ 370 nm. As substrate temperature increased, this absorption edge shifts to shorter wavelength. Based on these absorption profiles, the band gap energies of the ZnS:Mn films were determined. For direct transition, the relation between the absorption coefficient α and the energy of the incident light $h\nu$ is given by:[Elidrissi et al., 2001; He et al., 1996; Kam et al., 1999]

$$(\alpha h\nu)^2 = B(h\nu - E_g) \qquad \textbf{(5.2.1.3)}$$

where B is a constant and E_g is the band gap energy. Figure 5.2.2.4 shows the plot of $(\alpha h\nu)^2$ vs $h\nu$. By extrapolating the linear portion of the curve to zero, films with band gap energies of 3.50, 3.47, 3.44 and 3.28 eV are obtained at deposition temperatures of 450, 350, 250, 150 °C, respectively. For ZnS, zinc-blende structure has a smaller energy gap than that of the wurtzite structure. Therefore at higher deposition temperature, the films possess a higher wurtzite to zinc-blende ratio resulting in a larger band gap. Similar, it is noticed that the change in band gap energy also have a common feature of a significant change between 150 °C to 250 °C and a milder change between 250 °C to 450 °C. Therefore, as suggested by our XRD data, the shifts of both absorption edge and band gap energy are related to the change of wurtzite to zinc-blende ratio in ZnS:Mn films with different deposition temperatures.

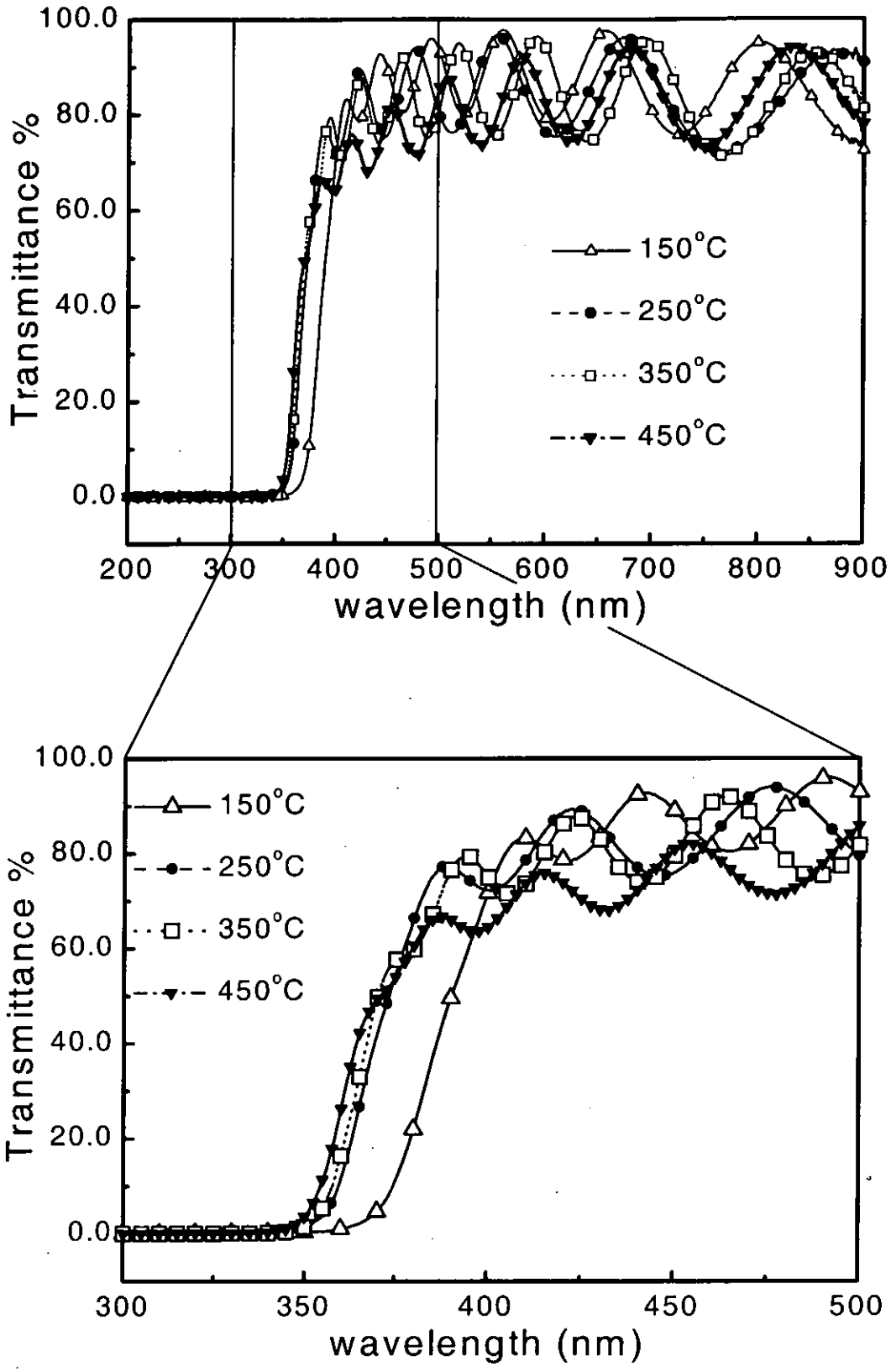

Figure 5.2.2.3 Transmittance of ZnS:Mn films on ITO-coated glasses deposited with various substrate temperatures.

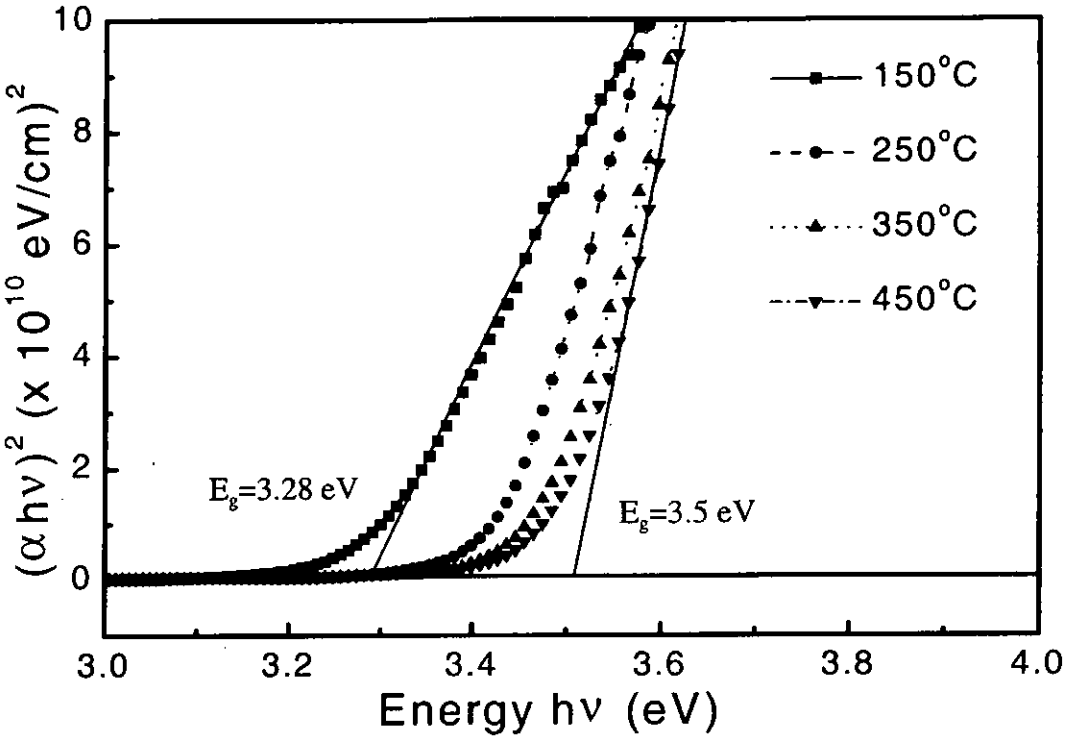

Figure 5.2.2.4 The dependencies of $(\alpha hv)^2$ on hv of ZnS:Mn films

5.2.3 Summary

ZnS:Mn films were successfully grown on Si (001) and ITO-coated glass substrates by PLD method. The deposited ZnS:Mn films are smooth and crack-free. As the substrate temperature increased, the crystallite changes from a circular to an elongated shape with a wider size distribution as observed by SEM. Meanwhile, the XRD results show that the structure changes from a zinc-blende dominated structure to a mixture of zinc-blende and wurtzite structure. ZnS:Mn films with preferred wurtzite structure are obtained at substrate temperatures ≥ 150°C and the structure changes are not affected by the substrate used. Both SEM and XRD results indicate that the back-filled Ar pressure had no significant effect on the structural properties of ZnS:Mn films. Apart from structural changes, systematic changes of optical properties of the ZnS:Mn films are also observed with increasing substrate temperature. As the substrate temperature increased, the peak of the orange-yellow PL band shifts to

a shorter wavelength, the refractive index increases and the absorption edge shifts to shorter wavelength indicating that the increment of the band gap energy. All the above optical properties observed have a common feature that they have a significant change between 150 °C to 250 °C and a milder change between 250 °C to 450 °C. This feature suggests that the changes of these optical properties of the ZnS:Mn films may have a same origin i.e. from the increasing of wurtzite to zinc-blende ratio with the increment of substrate temperature. Since the XRD results illustrate the same trend of the structure variation of the ZnS:Mn films with substrate temperature, all the changes in the optical properties of ZnS:Mn films are correlated with the changes in the structure of the films.

5.3 Multilayers for electroluminescence

With the studies on the basic characteristics of the insulating and phosphor layers, the interest was promoted to the electroluminescent behavior of the phosphor layers with different combination of insulating materials stacked with the phosphor layer. In this part of the study, the insulating materials used were $BaTiO_3$ and PZT. From previous studies in section 5.1.2 and 5.1.3, $BaTiO_3$ films were found to have extraordinary high dielectric constant (ε_r~1200, 1kHz) at zero dc biased field with a weaker degree of ferroelectric behavior. Meanwhile PZT films showed clearly ferroelectric properties with lower dielectric constant (ε_r~680, 1kHz) at zero dc biased field but a higher dielectric constant in the vicinity of the corresponding coercive field for the *P-E* hysteresis. The difference in dielectric behavior is expected to influence the charge accumulation at the insulator and phosphor interface and hence the charge injected into the phosphor layer driving by an ac field for electroluminescent operation. In this section, a brief study on the electroluminescent properties for the heterostructures with different insulating layers was performed.

5.3.1 The layers structure

Based on the insulating layers of $BaTiO_3$ and PZT fabricated in section 5.1, heterostructures for electroluminescent measurement were fabricated as shown in figure 5.3.1. The phosphor ZnS:Mn layer was coated on the $BaTiO_3$/LNSMO/LAO and PZT/LNSMO/LAO heterostructures and with ITO transparent electrode on the top most for electroluminescent measurement.

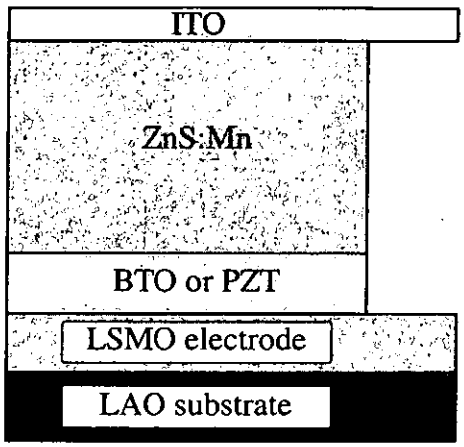

Figure 5.3.1 ac EL device structure

5.3.2 Electroluminescent (EL) measurement

EL measurement was performed with an EL driver and a Spex 1403 double grating monochromator equipped with photomultipler tube. The commercially EL driver provides 1kHz output waveform and was used to drive the multilayer as a function of applying voltage for EL measurement. Figure 5.3.2 shows the EL spectra for ITO/ZnS:Mn/$BaTiO_3$/LNSMO/LAO heterostructures obtained under different applied voltage. Similar EL spectra for PZT as the insulating layer have been obtained as shown in figure 5.3.3. The spectra indicate that the emissions for both $BaTiO_3$ and PZT stacked with ZnS:Mn are peaked at 585 nm which is the emission of the Mn^{2+} ions presented in the ZnS host. The areas under the EL spectra for different applied voltage are integrated and plotted against the applied voltage as shown in figure 5.3.4. From figure 5.3.4, both heterostructures show similar trends of increasing brightness with applied voltage. Even though the heterostructure based on $BaTiO_3$ insulating layer seems to have an observable brightness at a lower applied voltage, it cannot be concluded that the threshold voltage for EL is lower than the heterostructure using PZT. Also it cannot make a judgment on the efficiency of EL between these two insulating materials. The reasons are because a) the thickness of the ZnS:Mn are not determined in this experiment and the alignment of the EL experimental setup can influence the recorded intensity.

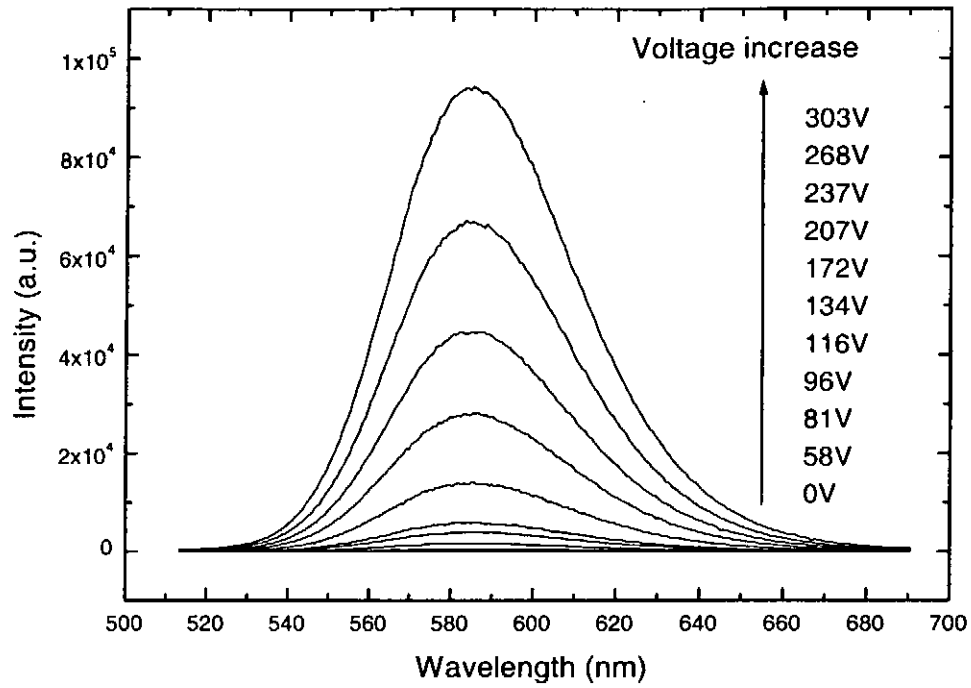

Figure 5.3.2 EL spectra of ITO/ZnS:Mn/$BaTiO_3$/LNSMO/LAO heterostructures.

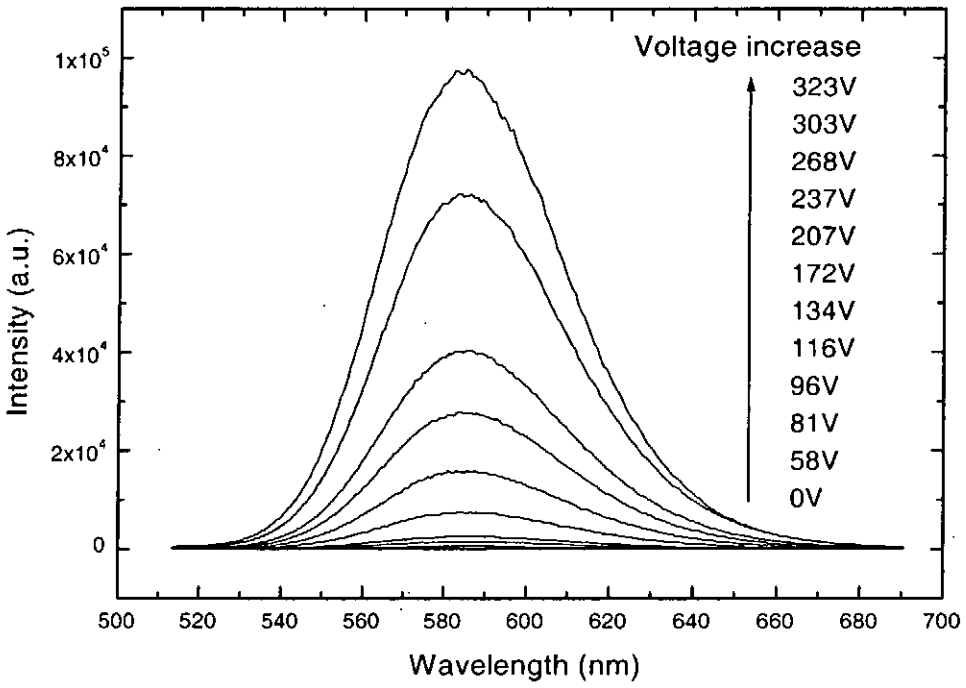

Figure 5.3.3 EL spectra of ITO/ZnS:Mn/PZT/LNSMO/LAO heterostructures.

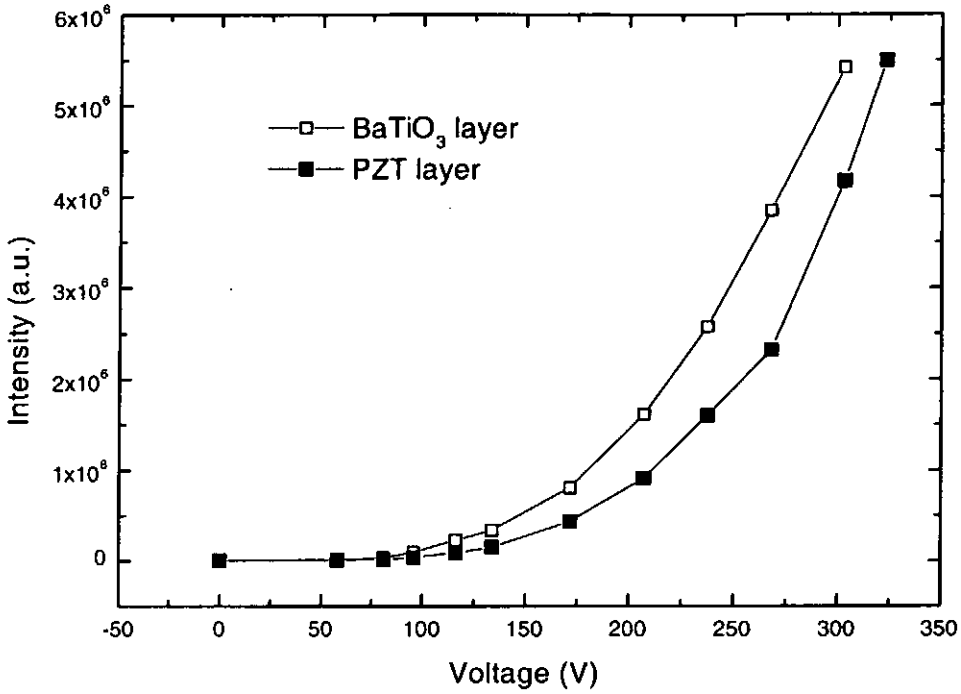

Figure 5.3.4 EL intensity as a function of applied voltage (0-peak)

CHAPTER 6

CONCLUSIONS AND RECOMMENDATIONS FOR FUTURE WORK

In our studies, fabrication of individual layers including insulating layer and phosphor layer have been performed as fundamental researches for further investigation on insulating-film/phosphor-film/insulating-film heterostructures which is a potential structure for future ac thin film electroluminescent device.

Firstly, $BaTiO_3$ films, a commonly used insulating material, have been successfully fabricated on LAO substrates. Effects of film thickness on $BaTiO_3$ structural properties were investigated. Thickness of the films, ranging from 30 nm to 2500 nm, was controlled by laser ablation time. All these films, in general, showed good crystallinity with epitaxial grown (001) out-of-plane oriented on top of LAO (001) substrates as they were studied by XRD θ-2θ scan. ω-rocking curve showed that the film's thickness systematically affected the degree of texture. The ω rocking curve showed that the crystallinity, in general, increased with film thickness. A full width at half maximum of 1.76° of the $BaTiO_3$ (002) rocking curve for the 30 nm $BaTiO_3$ film was decreased to only 0.43° for the 2500 nm $BaTiO_3$ film. For film thickness less than 1 μm, however, the crystalline quality was maximized at about 200 nm. This indicated that the texture was improved as films grew to 200 nm and then deteriorated as the film thickness further increased to 700 nm. Then the texture became better again as it further grew toward 2500 nm. In general all the films showed good texture, the film with the worst texture only showed 1.76° of FWHM of the (002) peaks and it still consider being good in orientation. AFM studies showed that the grain size increased with film thickness and so did the surface roughness. For all the films, surface roughness was less than 1% of the deposited thickness and was therefore quite low. Raman spectra studies showed that all the $BaTiO_3$ films with thickness above 450 nm were in tetragonal phase and contained no other impurity

phase. Our results indicated that films with progressively improved crystallinity and good surface qualities were produced by increasing film thickness. Hence the effects of film thickness of $BaTiO_3$ on the structural properties were revealed. Furthermore, $BaTiO_3$ and PZT films were also epitaxially grown on LNSMO buffered LAO (001) substrates. Both films with good crystallinity and texture were obtained. Actually, the crystallinity of $BaTiO_3$ films grown on LNSMO was comparable to those grown on LAO substrates. Both $BaTiO_3$ and PZT films showed ferroelectricity as observed in the *P-E* loop measurements.

Secondly, ZnS:Mn films, a common used phosphor layer material, were successfully grown on Si(001) and ITO-coated glass substrate. The optical dispersion functions of the ZnS:Mn films derived at different substrate temperature were obtained by spectroscopic ellipsometry. In order to yield a more accurate optical constant of the ZnS:Mn films, we used a modified Sellmeier model, in which an effective surface layer representing the surface roughness in the bulk was visualized. The refractive indices of the ZnS:Mn films increase with substrate temperature. Shifts in the absorption edge as well as the energy gap due to the substrate temperature were also observed in the transmittance spectra. In addition, the peak of the orange-yellow PL band shifted to a shorter wavelength with increasing substrate temperature. All these changes in optical properties of the ZnS:Mn films were correlated with the structural change which was confirmed by our XRD measurement. At low substrate temperature, ZnS films of zinc-blende structure were preferred resulting in a smaller refracrive index and band gap energy while mixed wurtzite and zinc-blende phase became dominant at higher substrate temperature. This mixed phase had a larger refractive index and band gap energy.

At last, electroluminescence of the insulating-film/phosphor-film heterostructures with two different insulating layer combinations: i.e. $BaTiO_3$ and PZT, have been observed. The obtained electroluminescent spectra showed no significant difference by using two different insulating layers. All spectra had the maximum at 585 nm and increased in intensity with the applied voltage of 1 kHz.

Although the effects of processing parameters on the structural as well as optical properties for each individual layer were obtained in our present studies, some aspects still need further experimental investigation. Firstly, the influence of the electrical properties and ferroelectric properties of insulating layers on the electroluminescent mechanism should be determined. The knowledge of these properties is essential for device applications. Secondly, effects of the two types of insulating layer on electroluminescence of the heterostructures should be worked out in more detail. This study could provide information on choosing the right insulating layer for electroluminescent device.

REFERENCES

Chapter 1

Krasnov, A.N., "Selection of dielectrics for alternating-current thin-film electroluminescent device", *Thin Solid Films*, Vol. 347, pp. 1-13 (1999).

Lee, Yun-Hi, Ju, Byeong-Kwon, Kim, Dong-Ho and Oh, Myung-Hwan, "Comprehensive Understandings on the High Dielectric Constant Insulating Layers for Alternating-Current Thin-Film Electroluminescent device", *IEEE Transactions on electron devices*, Vol. 48, pp.653-660 (2001).

Nakanishi, Y., Mori, S., Nakamura, T., Tatsuoka, H., Kuwabara, H. and Hatanaka, Y., "Effect of insulating layer structural properties for thin-film electroluminescent devices", *Materials Chemistry and Physics*, Vol. 43, pp. 292-295 (1996).

Rack, P.D. and Holloway, R.H., "The structure, device physics, and material properties of thin film electroluminescent displays", *Material Science and Engineering* R21, pp. 171-219 (1998).

Theis, D., "Selected analytical tools yield a better insight into electroluminescent thin films", *Physica Status Solidi A*, Vol. 81, pp. 647-655 (1984).

Tiku, S.K. and Rustomji, S.H., "Dielectrics for Bright EL Displays", *IEEE Transactions on electron devices*, Vol.36, pp.1947-1952 (1989).

Wu, W.B., Wong, K.H., Mak, C.L., Choy, C.L. and Zhang, Y.H., "Epitaxial $Pb(Zr_{0.52}Ti_{0.48})O_3/La_{0.35}Nd_{0.35}Sr_{0.3}MnO_3$ heterostructures for fabrication of ferroelectric field-effect transistor", *Journal of Applied Physics*, Vol. 88, pp.2068-2071 (2000).

Wu, W.B., Wong, K.H. and Choy, C.L., "A comparative study of in situ annealing effects on the electrical transport behavior of epitaxial $La_{0.5}Sr_{0.5}CoO_3$ and $La_{0.3}Sr_{0.3}MnO_3$ thin films", *Thin Solid Films*, Vol. 385, pp.298-301 (2001).

Chapter 2

Bhaskaran, S., Singh, V.P. and Morton, D.C., "Electron ejection processes at insulator-semiconductor interfaces in ACTFEL display devices", *IEEE Transactions on electron Devices*, Vol. 42, pp. 1756-1762 (1995).

Corlatan, D., Neyts, K., Vischere, P.D., Bossche, J.V. den and Maximus, B., "Properties of charge carriers in ZnS and their effect on the excitation of Mn", *Journal of the Society for Information Display*, Vol. 5, pp.131-136 (1997).

Destriau, G., "Recherches sure les scintillations des sulfures de zinc aux rayons," *J. Chim. Physuque*, vol. 33, pp. 587-625 (1936).

Howard, W.E., "The importance of insulator properties in a thin-film electroluminescent device", *IEEE Transactions on electron devices*, Vol. 24, pp. 903-908 (1977).

Inoguchi, T., Takeda, M., Kakihara, Y., Nakata, Y. and Yoshida, M., S.I.D. Intern. Symp. Digest, 84 (1974).

Keir, P.D., Le, H., Thuemler, R.L., Hitt, J., and Wager, J.F., "Relaxation charge anomalies in the charge-voltage characteristics of alternating-current thin-film electroluminescent devices", *Applied Physics Letter*, pp. 2421-2442 (1996).

Kina, H., Tamura, Y., Yamada, Y., and Maruta, Y., "The characteristics of SrS:Ce thin film electroluminescent device", *Japanese Journal of Applied Physics*, Vol. 36, pp.150-154 (1997).

Mellor, C.E., Plumb, J.L., Hope, L.L. and Abdalla, M.I., "Fabrication of electrode structures on very large electroluminescent displays", *Proceedings of the SPIE – The International Society for Optical Engineering*, Vol. 457, Los Angeles, USA, 24-25 Jan, 1984, pp. 66-73 (1984).

Ono, Y.A., *Electroluminescent displays.* Singapore: World scientific, 1995.

Russ, M.J. and Kennedy, D.I., "The Effects of Double Insulating Layers on the Electroluminescence of Evaporated ZnS:Mn Films," J. Electrochem. Soc., Vol. 114, pp. 1066 (1967).

Shih, S., Keir, P.D., Wager, J.F. and Viljanen, J., "Space charge generation in ZnS:Mn alternating-current thin-film electroluminescent devices", *Journal of Applied Physics*, Vol. 78, pp. 5775-5781 (1995).

Tong, W., Xin, Y.B., Park, W., and Summers, C.J., "In situ annealing studies of molecular-beam epitaxial growth of SrS:Cu", *Applied Physics Letters*, Vol. 74, pp.1379-1381 (1999).

Wager, J.F. and Keir, P.D., "Electrical characterization of thin-film electroluminescent devices", *Annual Review of Materials Science*, Vol. 27, pp. 223-248 (1997).

Chapter 3

Askar'yan, G.A., Pokhorov, AlM., Chantutiya, G.F. and Shipulo, G.Pl, *Sov. Phys. JETP*, Vol. 7, pp. 6 (1963).

Brech, F. and Cross, L., "Optical micromission stimulated by a ruby maser", *Applied Spectroscopy*, Vol. 16, pp. 59 (1962).

Chrisey, D.B. and Huber, G.K., *Pulsed Laser Deposition of Thin Films*, John Wiley & Sons, Inc, New York, (1994).

Dijkkamp, D., Venkatesan, T., Wu, X.D., Shaheen, S.A., Jisrawi, N., Min-Lee, Y.H., McLean, W.L. and Croft, M., "Preparation of Y-Ba-Cu oxide superconductor thin films using pulsed laser evaporation from high T_c bulk material", *Applied Physics Letter*, Vol. 51, pp. 619-621 (1987).

Gaponov, S.V., Klyuenkov, E.B., Nesterov, B.A., Salashchenko, N.N. and Kheifets, M.I., "Low-temperature epitaxy of dielectrics in laser sputtering in a low-density, chemically active gas", *Soviet Technical Physics Letters*, pp.193-194 (1979.

Metev, S. and Meteva, K., "Nucleation and growth of laser-plasma deposited thin films" *Applied Surface Science.*, Vol. 43, pp. 402-408 (1989).

Metev, S.M. and Veiko, V.P., *Laser-assisted Micro-technology*, 2nd Edition, Springer Berlin Heidelberg (1998).

Meyerand, R.G. and Haught, A.F., "Gas breakdown at optical frequencies", *Physical Review Letter*, Vol. 11, pp. 401-403 (1963).

Namiki, A., Kawai, T. and Ichige, K., "Angle-resolved time-of-flight spectra of neutral particles desorbed from laser irradiated CdS", *Surface Science*, Vol. 166, pp. 129-140 (1986).

Ready, J.F., "Development of plume of material vaporized by giant-pulse laser", *Applied Physics Letters*, Vol. 3, pp. 11-13 (1963).

Saenger, K.L., Pulsed laser deposition: Part II A review of process mechanisms,

Processing of Advanced Materials, v3, pp 63-82 (1993).

Singh, R.K., Holland, O.W. and Narayan, J., "Theoretical model for deposition of superconducting thin films using pulsed laser evaporation technique", *Journal of Applied Physics*, Vol. 68. pp. 233-247 (1990).

Smith, H.M. and Turner, A.F., "Vacuum deposited thin films using a ruby laser", *Appl. Opt.*, Vol. 4, pp. 147-148 (1965).

Wu, Wenbin, Wong, K.H., Mak, C.L., Choy, C.L. and Zhang, Y.H., "Effect of oxygen stoichiometry on the ferroelectric property of epitaxial all-oxide $La_{0.7}Sr_{0.3}MnO_3/Pb(Zr_{0.52}Ti_{0.48})O_3/ La_{0.7}Sr_{0.3}MnO_3$ thin-film capacitors", *Journal of Vacuum Science & Technology A*, Vol. 18, pp. 2412-2416 (2000).

Chapter 4

Albrecht, T.R. and Quate, C.F., "Atomic resolution with the atomic force microscope on conductors and nonconductors", *Journal of Vacuum Science & Technology A*, Vol. 6, pp. 271-274 (1988).

Binnig, G., Rohrer, H., Gerber, Ch., and Weibel, E., "7 x 7 Reconstruction on Si(111) Resolved in Real Space", *Physical Review Letters*, Vol. 50, pp.120-123 (1983).

Binnig, G., Quate, C. F., and Gerber, Ch., "Atomic force microscope" *Physical Review Letters*, Vol. 56, pp.930-933 (1986).

Binnig, G., Gerber, C., Stoll, E., Albrecht, T.R. and Quate, C.F. "Atomic resolution with the atomic force microscope" *Europhysics Letters*, Vol. 3, pp.1281-1286 (1987).

Martin, Y., Williams, C.C., Wickramasinghe, H.K., "Atomic force microscope mapping and profiling on a sub 100Å scale", *Journal of Applied Physics*, Vol. 61, pp. 4723-4729 (1987).

Chapter 5

Boilkov, Yu. A. and Claeson, T., "Microstructure and dielectric parameters of epitaxial $SrRuO_3/BaTiO_3/SrRuO_3$ heterostructures", *Journal of Applied Physics*, Vol. 89, pp. 5053-5059 (2001).

Bruggeman, D.A.G., "Berechnung verschiedener Konstanten von heterogenen Substanzen: 1. Dielektrizitätskonsstanten und Leitfähigkeiten der Mischkörper aus isotropen Substanzen",*Annalen der Physik (Leipzip)*, Vol. 24, pp. 636-679 (1935).

Cui, Dafu, Li, Chunling, Ma, Kun, Zhou, Yueliang, Liu, Yanwei, Chen, Zhenghao, Ma, Jianwei, and Li, Lin, "Raman spectroscopy of laser ablated $BaTiO_3/YBa_2Cu_3O_{7-x}$ thin film bilayer structure", *Applied Physics letter*, Vol. 68, pp. 750-752 (1996).

Damjanovic, D., "Ferroelectric, dielectric and piezoelectric properties of ferroelectric thin films and ceramics", *Rep. Prog. Phys.*, Vol. 61, pp. 1267-1324 (1998).

Elidrissi, B., Addou, M., Regragui, M., Bougrine, A., Kachouane, A. and Bernède, J.C., "Structure, composition and optical properties of ZnS thin films prepared by spray pyrolysis", *Materials Chemistry and Physics*, Vol. 68, pp. 175-179 (2001).

He, T., Ehrhart, P. and Meuffels, P., "Optical band gap and Urbach tail in Y-doped $BaCeO_3$", *Journal of Applied Physics*, Vol. 79, pp. 3219-3223 (1996).

Kam, C.H., Cheng, S.D., Zhou, Y., Pita, K., Han, X.Q., Que, W.X., Zhang, H.X., Lam, Y.L., Chan, Y.C., Sun, Z., and Shi, X., "Structural, electrical, and optical properties of sol-gel-processed thin films of $BaTiO_3$ on ITO glass", *Proceedings of the SPIE – The International Society for Optical Engineering*, Vol. 3896, pp. 466-471 (1999).

Krasnov, A.N., "Selection of dielectrics for alternationg-current thin-film electroluminescent device", *Thin Solid films*, Vol. 347, pp. 1-13 (1999).

Landauer, R., In "Electrical transport and optical properties of inhomogeneous media (Ohio State University, 1977).", *AIP Conference Proceedings No. 40*, pp. 2-45, American Institute of Physics, New York.

Li, Hong-Cheng, Si, Weidong, West, A.D. and Xi, X. X., " Near single crystal-level dielectric loss and nonlinearity in pulsed laser deposited $SrTiO_3$ thin films", *Applied Physics Letters*, Vol. 73, pp. 190-192 (1998).

McLaughlin, M., Sakeek, H.F., Maguire, P., Graham, W.G., Molloy, J., Laverty, S., Anderson, J., "Properties of ZnS thin films prepared by 248-nm pulsed laser deposition", *Applied Physics Letter*, Vol. 63, pp. 1865-1867 (1993).

Meng, X. J., Sun, J. L., Yu, J., Bo, L. X., Jiang, C. P., Sun, Q., Guo, S. L., and Chu, J. H., "Changes in interface capacitance for fatigued lead-zirconate-titanate capacitors", *Applied Physics Letters*, Vol. 78. pp. 2548-2550 (2001).

Ono, Y.A., *Electroluminescent displays*. Singapore: World scientific, 1995.

Robins, L.H., Kaiser, D.L., Rotter, L.D., Schenck, P.K., Stauf, G.T. and Rytz, D., "Investigation of the structure of barium titanate thin films by Raman spectroscopy", *Journal of Applied Physics*, Vol. 76, pp. 7487-7499 (1994).

Sharma, H.B. and Mansingh, A., "Phase transition in sol-gel-derived barium titanate thin films", *Journals of Physics D: Applied Physics*, Vol. 31, pp. 1527-1533 (1998).

Song, M.H., Lee, Y.H., Hahn, T.S., Oh, M.H. and K.H. Yoon, "Characteristics of ZnS:Mn thin film electroluminescent device using layered $BaTiO_3$ thin film structures", *Solid State Electronics*, Vol. 42, No. 9, pp. 1711-1717 (1998).

Ward, L., In "The optical constants of bulk materials and films, 2nd edition", pp. 138, Institute of Physics Publishing, Bristol and Philadelphia (1994).

Wu, Wenbin, Wong, K.H., Li, X.-G., Choy, C.L. and Zhang, Y.H., "Effect of annealing in reduced oxygen pressure on the electrical transport properties of epitaxial thin film and bulk $(La_{1-x}Nd_x)_{0.7}Sr_{0.3}MnO_3$", *Journal of Applied Physics*, Vol. 87, pp. 3006-3010 (2000a).

Wu, Wenbin, Wong, K.H., Mak, C.L., Pang, G., Choy, C.L. and Zhang, Y.H., "Influence of oxygen background pressure on the structure and properties of epitaxial $SrTiO_3/La_{0.35}Nd_{0.35}Sr_{0.3}MnO_3$ heterostructures grown by pulsed laser deposition", *Journal of Vaccuum Science and Technology A*, Vol. 18, pp.2378-2383 (2000b).

Wu, W.B., Wong, K.H., Mak, C.L., Choy, C.L. and Zhang, Y.H., "Epitaxial $Pb(Zr_{0.52}Ti_{0.48})O_3/La_{0.35}Nd_{0.35}Sr_{0.3}MnO_3$ heterostructures for fabrication of ferroelectric field-effect transistor", *Journal of Applied Physics*, Vol. 88, pp.2068-2071 (2000c).

Wu, W.B., Wong, K.H., Choy, C.L. and Zhang, Y.H., "In situ oxygen control and high thermal stability of epitaxial $(La_{1-x}Nd_x)_{0.7}Sr_{0.3}MnO_3$ films fabricated by pulsed laser deposition", *Thin Solid Film*, Vol. 389, pp.56-61 (2001).

Yamamoto, H. "Zinc Sulphide". In Vij, D.R. and Singh, N., *Luminescence and Related Properties of II-VI Semiconductors*, NOVA Science publishers, INC. USA, pp169-207 (1998).